ROOM TEMPERATURE GOLD-VACUUM-GOLD

TUNNELING EXPERIMENTS

DISSERTATION

Presented to the Graduate Council of the

North Texas State University in Partial

Fulfillment of the Requirements

For the Degree of

DOCTOR OF PHILOSOPHY

BY

E. Clayton Teague,   B.S.,M.S.

Denton, Texas

August, 1978

Teague, E. Clayton, <u>Room</u> Temperature <u>Gold-Vacuum-Gold</u> <u>Tunneling</u> <u>Experiments</u>. Doctor of Philosophy (Physics), August, 1978, 218 pp., 3 tables, 45 figures, bibliography, 84 titles.

An experiment has been completed which demonstrated quantum mechanical tunneling of electrons between two gold electrodes separated in vacuum. The tunneling current between the gold electrodes has been measured, for fixed voltages of 0.1 and 0.01 volts, as the electrode spacing was varied from a distance of approximately 2.0 nm down to a point where the electrodes touched. Current-voltage characteristics for fixed electrode spacing in the direct tunneling region have also been measured. Numerical calculations of the tunneling current based on the free-electron model of the electrodes and the barrier, an image-potential reduced barrier, and a WKB approximation for the tunneling probability have been performed and compared with Simmons' theory and with the experimental results.

Within experimental error the results indicate that an image potential reduced barrier with the modifications suggested by Lang and Kohn gives a close approximation to the true barrier for metal-vacuum-metal tunneling. For the first time, the work function of the electrodes in a tunneling experiment has been deduced from experimentatl parameters independent of the tunneling device.

Conventional devices for conducting these experiments

are fabricated by evaporating one electrode onto a glass substrate, forming an oxide layer with a fixed thickness of one to three nm on the electrode and then evaporating a second electrode over the oxide layer. These experiments have been widely used to measure the characteristics of Josephson junction devices, electrons and phonons in superconductors, semiconductor surfaces and junctions, the material used for the insulating barrier, and intentionally introduced impurities at the barrier-electrode interface.

While these experiments have made and continue to make valuable contributions to solid state physics, they have been seriously restricted by the small number of electrode materials which tend to form natural oxides suitable for a tunneling barrier. In addition, interpretation of the experimental results has been limited because of the difficulties in characterizing the atomic structure and composition of the insulator and the insulator-electrode interfaces. Major problems resulting from this lack of structure characterization are that the electron potential energy and the energy-momentum relationship of the electron while it is in the barrier cannot be modeled adequately.

By making a change from these conventional devices to one which uses a vacuum barrier, material restrictions are removed, electron properties in the barrier are well-known, structure of the electrode-barrier interface is more defined and, in addition, the electrode spacing may be continuously

changed. There are, however, some difficulties with vacuum barrier tunneling which must be weighed along with its advantages. The tunneling current between two electrodes is an exponential function of their spacing; a change in spacing of 0.1 nm produces a factor of 10 change in current for electrode work functions of approximately 5 electron volts. Thus great care must be exercised in electrode preparation and in the mechanical and thermal design of the vacuum tunneling device.

The device developed for this experiment demonstrates that these difficulties can be overcome so that vacuum tunneling experiments can reliably be performed. With this demonstration many new areas of reserarch may be explored. In addition to further exploration of the areas given for the conventional devices, the vacuum tunneling technique can be utilized in the field of metrology as a tool to locate the true position of a surface to a precision of 0.1 nm, 10 to 100 times greater than presently available techniques. Without the limitation to electrode materials with form oxides that are good barriers, vacuum tunneling experiments will be a very versatile tool for performing inelastic electron tunneling spectroscopy of a wide range of adsorbates. Because of its extreme sensitivity to changes in electrode spacing, a vacuum tunneling device could serve as a transducer for detecting part-per-million changes in any quantity which would change the electrode spacing, e.g. temperature, vibrations, and mechanical strain.

TABLE OF CONTENTS

The Work Function and The Image Potential
The Barrier Potential Energy Function
The Tunneling Process
Approximate Analytical Expression For
  Tunneling Current
Numerical Calculations of Tunneling Current

Mechanical and Thermal Requirements
Choosing an Electrode Material and
  Preparing The Electrodes
Temperature Control System
Vacuum System For The Tunneling Experiment
Electrode Holder and Micropositioning
  Assembly
Vibration and Acoustical Isolation
Tunneling Electronics

Data and Analysis
Effects of Mechanical Stress on Tunneling
  Characteristics
Conclusions

APPENDICES

LIST OF TABLES

LIST OF ILLUSTRATIONS

CHAPTER I

INTRODUCTION

According to quantum mechanics, a material particle can pass through a spatial region in which the particle's kinetic energy is less than its potential energy. The phenomenon is known as tunneling. A macroscopic example would be a ball which, when rolled toward a sharply peaked hill with insufficient speed to get over the top, does not roll back, but appears on the other side of the hill without affecting the ball or the hill and continues on its way. The probability of such an event occurring is astronomically small at the macroscopic level. However, for electrons and other fundamental particles and walls formed by nuclear and atomic forces, the probability while still small (one in 10^9 is not unusual) leads to major physical effects. This work pertains to the tunneling of electrons between two metal plates closely spaced in vacuum.

Tunneling is not a new idea; it is in fact almost as old as quantum mechanics. In less than two years after Schrodinger[1a] had published his now classic papers on "Quantization as a Problem of Proper Values," Oppenheimer[1b] had used the wave mechanical concept of tunneling to explain the autoionization of atomic hydrogen, Fowler and Nordheim[1c] had explained the main features of electron emission from

1

cold metals in high external fields and Gamow[1d] had described the alpha particle decay process in heavy nuclei. The efforts by Frenkel[1e] and by Holm[1f] to describe the anomalous temperature dependence of the resistance of electrical contacts were the earliest studies of electron tunneling between metals.

Since these early studies, electron tunneling in solids has remained a very active area of solid state physics. Discoveries over the last 15 years by Giaever[1g] that tunneling could be used to measure the properties of superconductors, by Esaki[1h] of interband tunneling in semi-conductors, by Josephson[1i] of the unique characteristics of tunneling between superconductors, and by Lambe and Jakelvic[1j] that tunneling could be used as a spectroscopic tool have had a major influence on the development of physics, and all have important technological consequences.

In the simplest form, an experiment to measure electron tunneling between two metals would be performed as shown in Fig. 1A. Two parallel plates are separated by an insulator and connected to a variable voltage source. An ammeter and voltmeter are also included to measure the current flow and the applied voltage. Normally, a direct current would not flow through the circuit. However, if the plates are spaced very close together (on the order of ten atomic diameters), a tunneling current will flow. If the plates could be made sufficiently flat and parallel over an area of one square
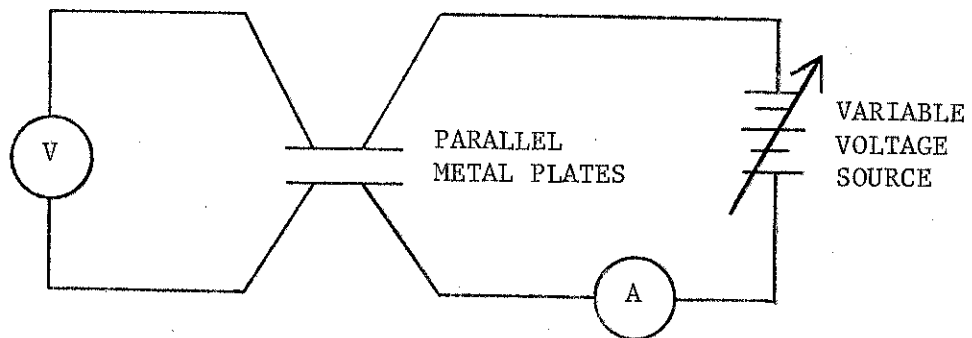
Fig. 1a. Simplified Circuit Diagram of Electronics to Conduct a Tunneling Experiment. Spacing of the metal plates must be less than approximately 2 nm to observe tunneling.
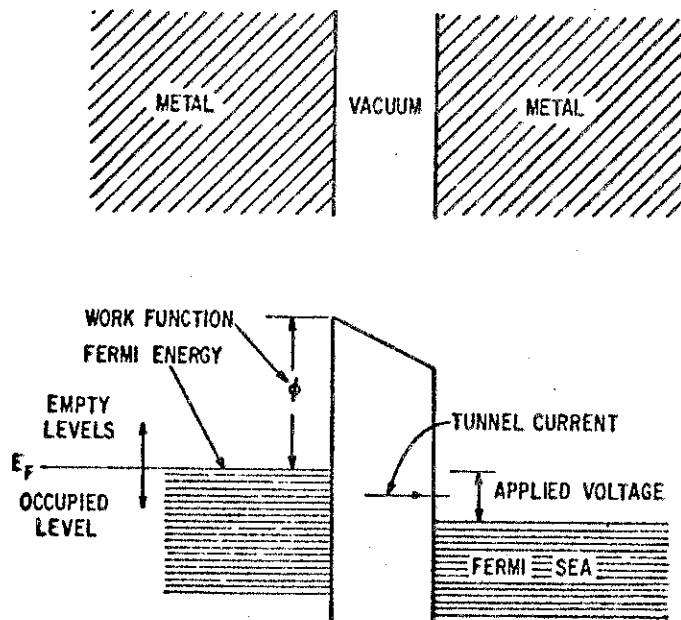
Fig. 1b. Above: Two Metals Separated in Vacuum. Below: Energy Diagram Associated with This Configuration.

Fig. 1. Schematic of a Tunneling Experiment. Fig. 1b is from Giaever in Reference 3.

millimeter, the current flow would be several amperes for
an applied voltage of one-tenth volt.

Conventional devices for conducting these experiments are
fabricated by evaporating one electrode onto a glass substrate,
forming an oxide layer with a fixed thickness of 1 to 3 nm on
the electrode and then evaporating a second electrode over
the oxide layer. These experiments have been widely used to
measure the characteristics of Josephson junction devices,
electrons and phonons in superconductors, semiconductor surf-
aces and junctions, the material used for the insulating
barrier, and intentionally introduced impurities at the barrier-
electrode interface. While these experiments have made and
continue to make valuable contributions to solid state physics
and technology, they have been seriously restricted by the
small number of electrode materials which tend to form natural
oxides suitable for a tunneling barrier. In addition, interpre-
tation of the experimental results has been limited because
of the difficulties in characterizing the atomic structure
and composition of the insulator and the insulator-electrode
interfaces. A major problem resulting from this lack of
structure characterization is that the energy-momentum rela-
tionship of the electron while it is in the barrier cannot
be modeled adequately.

By making a change from these conventional devices to one
which uses a vacuum barrier, material restrictions are removed,
electron properties in the barrier are well-known, structure of

the electrode-barrier interface is more defined and, in addition, the electrode spacing may be continuously changed. There are, however, some difficulties with vacuum barrier tunneling which must be weighed along with its advantages.

A schematic energy diagram for a metal-vacuum-metal tunneling structure is shown in Fig. 1B. The energy diagram is based on Sommerfield's electron theory of metals in which all the conduction electrons of a metal are considered as being placed in a potential energy box and distributed over the allowed energy values according to Fermi-Dirac statistics. At zero temperature, the electrons, therefore, fill the energy levels up to a maximum energy, the Fermi energy. The energy required to remove one of the electrons from this energy to a large distance from the metal is known as the metal's work function. As shown in the figure, when a voltage is applied to one of the metals, its Fermi energy is lowered relative to the other; the energy difference is equal to the product of the magnitude of the charge on an electron and the applied voltage.

It will be shown in Chapter II that an approximate expression for the tunneling current, I, under these conditions is given by:

$$I = C \exp(-a\, S\, B^{1/2})\, A\, V, \qquad (1\text{-}1)^*$$

_____

*Equations will be numbered in the form (Chapter No.-Eq. No.)

where* C $\doteq$ 3.16 x 10^{13} A/m^2/V, a = 10.25 (nm)$^{-1}$(eV)$^{-1/2}$, S is the electrode spacing, B is the average barrier height for an electron at the Fermi energy, A is the tunneling area, and V is the applied voltage. The important consequences of Eq. 1-1 for the vacuum tunneling experiment are that small changes in electrode spacing or mean barrier height have a very large effect on the tunneling current. An electrode spacing of 0.1 nm produces approximately a factor of 10 change in the tunneling current for a mean barrier height of 4 eV. Changes of about half this magnitude can be produced as a result of work function changes produced by the formation of oxide or other films on the electrode surface. Thus great care must be exercised in electrode preparation and in the mechanical and thermal design of the vacuum tunneling device.

Young et al[2a] and Thompson and Hanrahan[2b] have previously performed vacuum barrier tunneling experiments. Both of these experiments were primarily concerned with observing the transition from Fowler-Nordheim field emission tunneling to direct vacuum tunneling. Young et al[2a] did report a preliminary observation of a linear current-voltage characteristic for direct tunneling at a spacing of approximately 1.2 nm. Thompson and Hanrahan[2b] have not reported any current-voltage characteristics. Uncontrolled fluctuations in electrode spacing limited the exploration of direct vacuum tunneling properties in both experiments.

---

* $\doteq$ denotes "approximately equal to."

The objective of this work, which has evolved from that of Young et al, was to extend the previous vacuum barrier investigations to a detailed experimental study of the direct vacuum tunneling region. Such detailed experimental results would provide a means to test the present theoretical framework of electron tunneling between solids. Some of the unresolved questions in this area: (1) What is the relationship between the classical electrostatic image potential and the quantum mechanical exchange and correlation potential? (2) What is the transit time for a tunneling electron? and (3) How is the distance between the last atomic planes of the two electrodes related to the tunneling barrier thickness?

Explicit goals of this work, which were partially achieved, were first, to measure the current through a vacuum tunneling device for fixed voltages of less than one-tenth volt as the electrode spacing was varied from a distance of approximately 2.0 nm down to a point where the electrodes touched; second, to measure the current-voltage characteristics for fixed electrode spacing in the direct tunneling region; third, to compare the measured results with available theories of electron tunneling, and finally to establish a basis for using a vacuum tunneling device for use as a probe to measure the position of a surface to a precision of 0.1 nm; 10 to 100 times greater than presently available techniques. Contributions to all these goals were obtained and will be described in later chapters.

The qualification on completely achieving the goals was given because the quality of electrode surfaces and the precision of electrode spacing measurements were not adequate in the area of the first three goals to resolve completely the questions posed about the theoretical framework.

A discussion of some fundamental concepts related to electron tunneling in solids, with particular emphasis on the origin of the work function and the barrier potential energy function, is given in Chapter II. Chapter III describes the requirements of the experimental apparatus for a vacuum tunneling experiment and the particular solution adopted for this work. Experimental results and an analysis of the relationship between the results and the numerical calculations of Chapter II are given in Chapter IV.

CHAPTER II

SOME BASIC CONCEPTS OF METAL-VACUUM-METAL TUNNELING THEORY

The objective of this chapter is to calculate, with the use of simple models, the current versus voltage (I-V) characteristics and, for a fixed voltage, the current versus spacing (I_{cv}-S) characteristics of the gold-vacuum-gold tunneling device used in the experiments of this work. The primary results of these calculations are tables and graphs of the I-V and I_{cv}-S characteristics which can be used for comparison with the measured data to be presented in Chapter IV.

While quite thorough treatments of electron tunneling in conventional metal-insulator-metal junctions are available in the literature[3-12], no numerical results have previously been published which fully accounted for the image potential variation with electrode spacing and applied bias voltage; both of which are essential for comparison with the metal-vacuum-metal tunneling data. Additional motivations for performing the calculations were that (1) almost all of the available theoretical results have been seriously questioned in terms of numerical accuracy and overall validity of the analytical approximations which were employed[13], and (2) even if one were to accept the validity of results which

9

have been obtained, the effort to extrapolate and apply these approximate results to the gold-vacuum-gold tunneling device would be almost as great as carrying out the more accurate numerical calculations.

The content of the following discussion is therefore (1) a description of models of the electron properties of the tunneling device and of the tunneling process, (2) a development based on these models to obtain analytical expressions for the tunneling current which are, within the limitations of the models, "almost" exact, (3) a reduction of the exact expressions with commonly used approximations to obtain analytical solutions for I vs V and S in terms of experimental parameters, and (4) a description of the procedure employed to carry out numerical computations of I vs V and S along with a presentation of results from these computations. No attempt will be made to give either a review or a comprehensive survey of the literature that is related to the topics of this chapter. Tutorial coverages of the theoretical and experimental aspects of electron tunneling into semiconductors, metals, and superconductors are given in the book edited by E. Burstein and S. Lundquist[3]. A comprehensive review and digest of the tunneling literature up through 1969 has been given by C. B. Duke[4]. Recent development in the theories of tunneling are covered in two papers of debate between T. E. Feuchtwang and C. Caroli, et al[10] and references contained therein.

The Work Function and The Image Potential.

By its nature, the metal-vacuum-metal tunneling device can be completely represented by a model which accounts for the electron properties of two metal-vacuum interfaces and their interaction. Neglecting for the moment the interaction, the problem is then to obtain a model that adequately describes a uniform metal and its interface to vacuum. In this section properties of the metal-vacuum interface will be developed in terms of the general theory of metal surfaces formulated by Lang and Kohn; LKI[14], LKII[15], LKIII[16]. Their theory will be used as a basis to describe the origins of the metal work function and to obtain a potential energy function for the metal-vacuum interface.

Lang and Kohn's work is based on the density-functional theory of inhomogeneous electron gas systems formulated by Hohenberg, Kohn, and Sham (HKS)[17]. The HKS formalism is a self-consistent-field method and as such its fundamental idea is to replace the actual interactions; electrostatic, exchange, and correlation, between the electrons and the ion-cores by an interaction between one electron and an averaged self-consistent potential produced by the other electrons and the ion-cores. It therefore fully accounts for the effects of electron exchange and correlation and is in principle capable of providing exact results. Since the concepts of this formalism will be used so extensively in the following

discussion of the work function and the surface potential energy function, a brief summary of the HKS theory, based in part on a review by Hedin and Lundqvist[18], will now be given.

The theory rests on two theorems. One states that the ground state wavefunction of an interacting many-electron system, and thus all ground state properties, are functionals of the electron density $N(\underline{r})$. The other states that the ground state energy for a given external potential $U(\underline{r})$ can be written as

$$E_u[N(\underline{r})] = \int U(\underline{r})N(\underline{r})d\underline{r} + F[N(\underline{r})],* \qquad (2.1)$$

where F is a universal functional of N, independent of the external potential U, and that E_u is a minimum for the correct density function $N(\underline{r})$.

With these theorems as a basis, HKS[17] further show that the total electronic ground-state energy of a many-electron system in an external potential $U(\underline{r})$ can be written in the following form:

$$E_u[N] = e\int U(\underline{r})N(\underline{r})d\underline{r} + (e^2/2) \int N(\underline{r})N(\underline{r}')/(|\underline{r}-\underline{r}'|)d\underline{r}d\underline{r}'$$

$$+ T_s[N] + E_{xc}[N]. \qquad (2.2)$$

---

* An underlined symbol indicates that it represents a vector quantity.

$\int$ denotes integration.

The functional $T_s[N]$ is the kinetic energy of a <u>noninteract-</u><u>ing</u> electron system, and $E_{xc}[N]$ represents the exchange and correlation energy. The first two terms in Eq. 2.2 represent the electron gas' electrostatic potential energy in the field $U(\underline{r})$ and the Coulomb self-energy of the electrons. All the complexities of the many-body interactions are contained in the functional $E_{xc}[N]$.

An effective potential, U_{eff} is then defined as

$$U_{eff}[N;\underline{r}] = U(\underline{r}) + e \int N(\underline{r}')/(|\underline{r}-\underline{r}'|)d\underline{r}' + U_{xc}[N;\underline{r}], \quad (2.3)$$

where:

$$U_{xc}[N;\underline{r}] = \emptyset E_{xc}[N]/\emptyset N(\underline{r})^*. \quad (2.4)$$

$U_{eff}[N;\underline{r}]$ is then shown to play the role of an effective single particle potential so that $E_u = T_s[N] + U_{eff}[N;\underline{r}]$. This expression for the total ground-state energy combined with an assumed form of $E_{xc}[N]$ enables one to solve the following self-consistency problem to obtain an exact density distribution of the system of N interacting electrons:

$$[-(\hbar^2/2m)grad^2 + U_{eff}[N;\underline{r}]] \, \Psi_i = e_i\Psi_i \quad (2.5)$$

$$N(\underline{r}) = \int^{\#}(i)|\Psi_i(\underline{r})|^2 \, \theta(u-e_i), \quad (2.6)$$

M is the electron mass and $\hbar$ is Planck's constant divided by

---

*$\emptyset$ denotes "variation of" in the calculus of variations sense.

$\int(i)$ denotes summation over the index i.

2 pi. The sum is over the N lowest-lying orthonormal solutions, Ψ_i, of Eq. 2.5. $\Theta(x)$ is unity for $x < 0$, and zero for $x > 0$, μ is the chemical potential of the metal. The e_i are Lagrange multipliers introduced to fix the number of electrons as the states Ψ_i are varied. Their identification as single particle energies is discussed later in this section. At finite temperatures, U_{xc} is defined in terms of the system's free energy and the Θ function is generalized to the Fermi distribution function.

The many-body problem has, therefore, been reduced to a set of one-body problems coupled only through the effective one body potential $U_{eff}[N;\underline{r}]$. Solution of Eqs. 2.3 to 2.6 proceeds in the usual manner: one begins with an assumed $N(\underline{r})$ and $E_{xc}[N(\underline{r})]$, constructs $U_{eff}[N;\underline{r}]$ from 2.3 and then finally calculates a new $N(\underline{r})$ with the use of 2.5 and 2.6. The procedure is then repeated until the new and old $N(\underline{r})$ differ by acceptable tolerances.

Lang and Kohn (LKI) calculate the electronic structure at a metal-vacuum interface by applying this formalism to the jellium model of a metal. In this model the positive ion-cores of the metal-lattice are replaced by a uniform, spacially fixed background of charge with density

$$N_+(\underline{r}) = N_a, \qquad x \leq 0$$

$$= 0 \qquad x > 0 \qquad\qquad (2.7)$$

The conduction or valence electrons with density $N(\underline{r})$ are free to move and settle in an equilibrium configuration

with respect to this fixed background of positive charge.
$N(\underline{r})$ is subject to the charge neutrality condition.

$$\int [N_+(\underline{r}) - N(\underline{r})] \, d\underline{r} = 0 \qquad (2.8)$$

For the tunneling experiment this model is a reasonable
approximation since the ion-core lattice and its resultant
electron band structure are not expected to significantly
affect the characteristics of the tunneling current.

The electronic structure of an inhomogeneous electron
gas with the inhomogeneity being produced by the background
of Eq. 2.7 is calculated in LKI. They demonstrate by numerical
calculations that even though the electron density in the sur-
face region of a metal varies quite rapidly, good agreement
with experimental results is obtained if one uses the approxi-
mation

$$E_{xc}[N] = \int e_{xc}(N(\underline{r})) \, N(\underline{r}) d\underline{r}, \qquad (2.9)$$

e_{xc} is the exchange and correlation energy per particle of a
uniform electron gas. By making use of Wigner's form of
$e_{xc}(N)$

$$e_{xc} = -0.458/r_s(N) - 0.44/(r_s(N)+7.8), \qquad (2.10)$$

$$r_s(N) = [3/(4 \text{ pi } a_B^3 N)]^{1/3}, \qquad (2.11)$$

and a $U(\underline{r})$ determined by Eq.2.7, the functions $N(x)$, $U_{eff}(x)$,

and the electrostatic part of U_{eff}, $V(x)$ are calculated for
several values of the electron gas density. In Eqs. 2.10 and
2.11, e_{xc} is in units of Hartrees. (1 Hartree = 27.2eV),
a_B is the Bohr radius, and N is the uniform background density
in number/cm^3. Fig. 2 is a graph constructed from a table
given in LKI of these three functions for an electron density
very close to that of electrons in gold, i.e., 5.76 x 10^{22}
electrons/cm^3. This density corresponds to an r_s of 3.03.

Eq.2.3 and 2.4 in connection with the results plotted
in Fig. 2 shows that for x less than about -1.0 nm, U_{eff}
approaches a constant value within the bulk of the material
as anticipated. Eq. 2.5 then simplifies to the one particle
Schrodinger equation

$$[-\hbar^2/(2m) \, grad^2 + V_E(-\infty) + \mu_{xc}(N_a)] \, \Psi_i = e_i \, \Psi_i \qquad (2.12)$$

$V_E(-\infty)$ is the electrostatic potential energy of an electron
in the metal interior; $\mu_{xc}(N)$ is the exchange and correlation
part of the total chemical potential $\mu(N)$ of an infinite
uniform gas of density N. From the definitions given earlier
for $E_{xc}[N]$ and e_{xc}, and the definition of the chemical poten-
tial,

$$\mu_{xc}(N) = d(Ne_{xc}(N))/dn \qquad \text{or} \qquad (2.13)$$

$$= e_{xc}(N) + N \, d(e_{xc}(N))/dn. \qquad (2.14)$$

If the zero of energy is chosen such that

$$V_E(-\infty) + \mu_{xc}(N_a) = 0, \qquad (2.15)$$
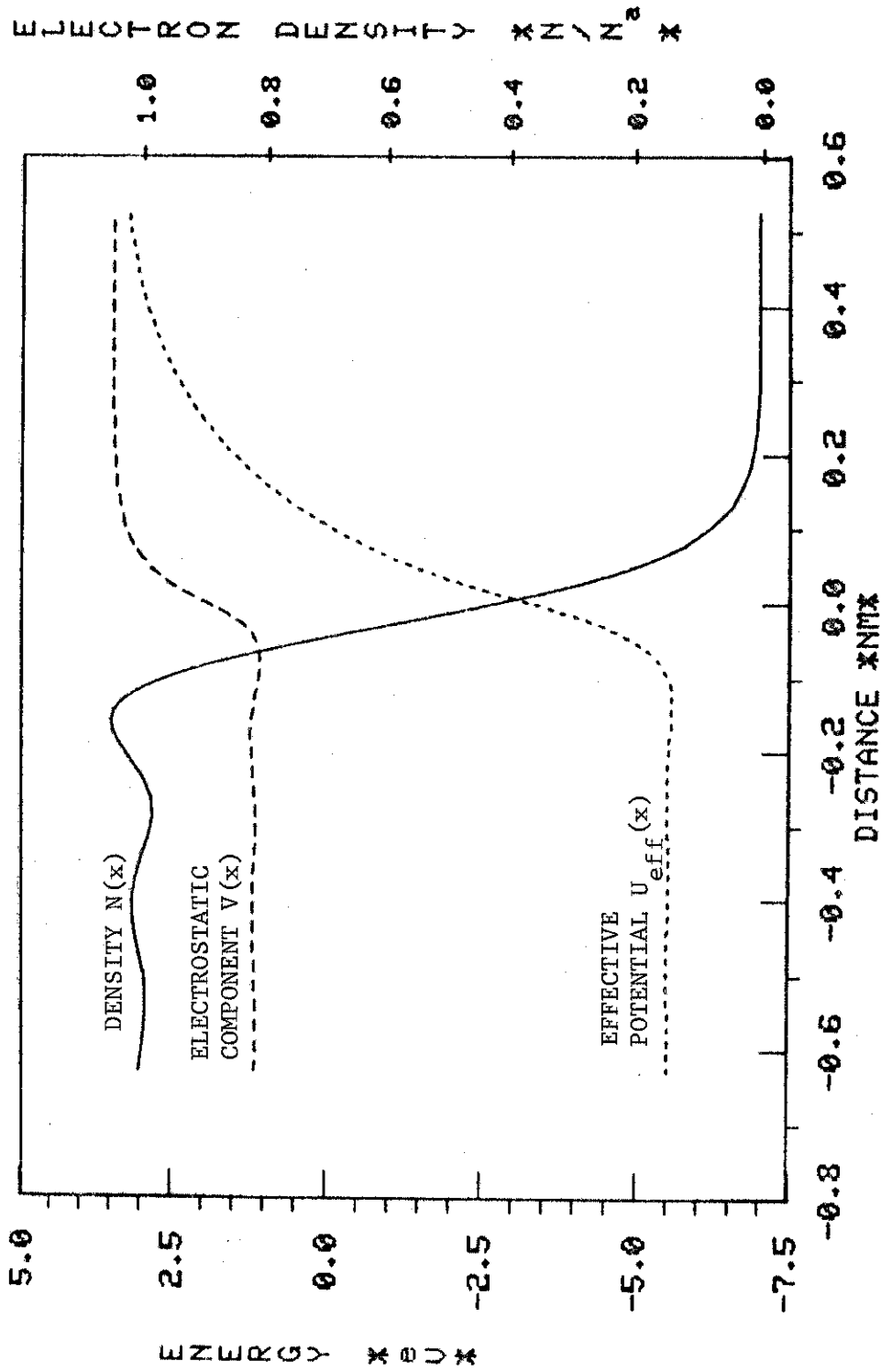
Fig. 2. Graph of Electron Density, Effective Electron Potential Energy, and Electro-static Component of the Potential at a Metal-Vacuum Interface. The positive background density corresponds to a Wigner-Seitz radius of 3. The graph is based on data from a table in N. D. Lang and W. Kohn, Phys. Rev. B1, 4555 (1970).

then the equation describing the electron motion in the electrodes at distance greater than 1 nm from the surface is

$$-(\hbar^2/2m) \; grad^2 \; \Psi_i = e_i \Psi_i. \qquad (2.16)$$

Therefore, for the case when $N(\underline{r})$ is a constant, the electrons in an interacting gas move as free particles.

Interpretation of the eigenvalues of Eq. 2.5 as the excitation energies of the elementary excitations of the electron gas is not valid for a general $U_{eff}[N;\underline{r}]$[18,19,20]. However, arguments are presented by Moruzzi et al[20] that demonstrate that for most bulk simple metals this intrepretation is a very good approximation. Slater[19] gives some numerical estimates of the energy errors involved in using this approximation for self-consistent calculations in atoms. Hedin and Lundquist[18] consider the problem from the Green function standpoint and one may conclude from a comparison of Eq. 2.5 with their equation for the excitation energies of quasielectrons that for uniform positive backgrounds the resulting energies and those of 2.5 would be the same. However, nonuniformities in the electron gas such as that generated by the pseudo-potentials of the ion-cores and the discontinuity at a metal surface cause all the usual differences between one-electron theory and many-electron theory to become manifest, i.e, self-energy corrections, relaxation times, and different energy-momentum relationships.

The work from Eq. 2.1 through 2.16 may appear an overly complex way of obtaining this free-electron result. However, the reader should observe that in addition to the free-electron behavior, this approach has also by Eqs. 2.12 and 2.15 very naturally given a means to determine the binding energy of the lowest energy state. The results also clearly demonstrate that the binding energy is due both to the electrostatic energy produced by the existence of a surface and to the energy resulting from exchange and correlation. Finally, the development through the calculated U_{eff} has produced a realistic potential energy function at a metal surface.

The work function, WF, of a metal provides the necessary reference for relating $V(-\infty)$ to the vacuum energy level. It is defined as the minimum energy required to separate an electron from the metal at zero temperature. Thus,

$$WF = (V_E(+\infty) + E_{N-1}) - E_N, \qquad (2.17)$$

where $V_E(+\infty)$ is the total electrostatic potential energy far from the metal surface and E_M is the ground state energy of the metal with M electrons. Arbitrary zeros of energy for V and E do not affect the result of Eq. 2.17. The chemical potential μ of a system is defined as $E_N - E_{N-1}$, thus, Eq. 2.17 can also be written as:

$$WF = V_E(+\infty) - \mu \qquad (2.18)$$

Since the electrostatic potential in the interior of a metal

with and without a surface differs by $V(-\infty)$, μ for a metal with a surface is

$$\mu = V_E(-\infty) + FE + \mu_{xc}(N_a),\qquad(2.19)$$

FE is the Fermi energy of a degenerate electron gas of density N_a. WF is therefore

$$WF = [V_E(+\infty) - V_E(-\infty)] + FE - \mu_{xc}(N_a).\qquad(2.20)$$

In a more compact form

$$WF = \overline{d}V_E - \overline{\mu},\qquad(2.21)$$

where $\overline{d}V_E = V_E(+\infty) - V_E(-\infty)$ and

$$\overline{\mu} = FE + \mu_{xc}(N_a).\qquad(2.22)$$

In this form the WF is seen to consist of two components, a surface part $\overline{d}V_E$, which is the rise in mean electrostatic potential energy across the metal surface and $\overline{\mu}$, a bulk part which is the intrinsic bulk chemical potential of the electrons relative to the mean electrostatic potential energy in the bulk interior. $\overline{d}V_E$ is due to the dipole layer created by the spilling-out of the electrons as shown by the distribution in Fig. 2. All many-body effects are contained in the exchange and correlation contributions to $\overline{\mu}$ and in their effect on the barrier potential $\overline{d}V_E$.

Combining Eq. 2.20 with the zero energy convention of Eq. 2.15, shows that the lowest energy eigenvalue of Eq. 2.16

is at an energy of $[\partial V_E + \nu_{xc}(N_a)]$ less than $V(+\infty)$. Eigen-states of Eq. 2.16 are then according to the Pauli exclusion principle occupied at zero temperature from this energy up to the maximum value FE. A diagram of the electron energy as a function of x position in the region of a metal vacuum interface is given in Fig. 3.

The work function of gold was estimated in LKII by again using Eq. 2.13 and Wigner's expression $e_{xc}(N)$ to obtain ν; ∂V_E was calculated from the double-layer solution of Poisson's equation,

$$\partial V_E = (e^2/\epsilon_o) \int x(N(x) - N_+(x))dx \qquad (2.23)$$

and the density distributions obtained from self-consistent solutions of Eqs. 2.5 and 2.6. In Eq. 2.23, e is the electron charge and ϵ_o is the free space dielectric constant. The results for gold were (all in units of electron volts)

$$FE = 5.57, \quad \nu_{xc}=-6.75, \quad \partial V_E= 2.32, \quad WF = 3.50. \qquad (2.24)$$

Experimental values of the work function are [21] 5.0 ± 0.2 electron volts for polycrystalline samples; the uncertainty accounts for the range of values obtained by various exper-imental techniques. Attempts to achieve better agreement by incorporating lattice effects through a pseudopotential were not successful.

It is not clear how the discrepancy between the theor-etical and experimental work functions should be apportioned
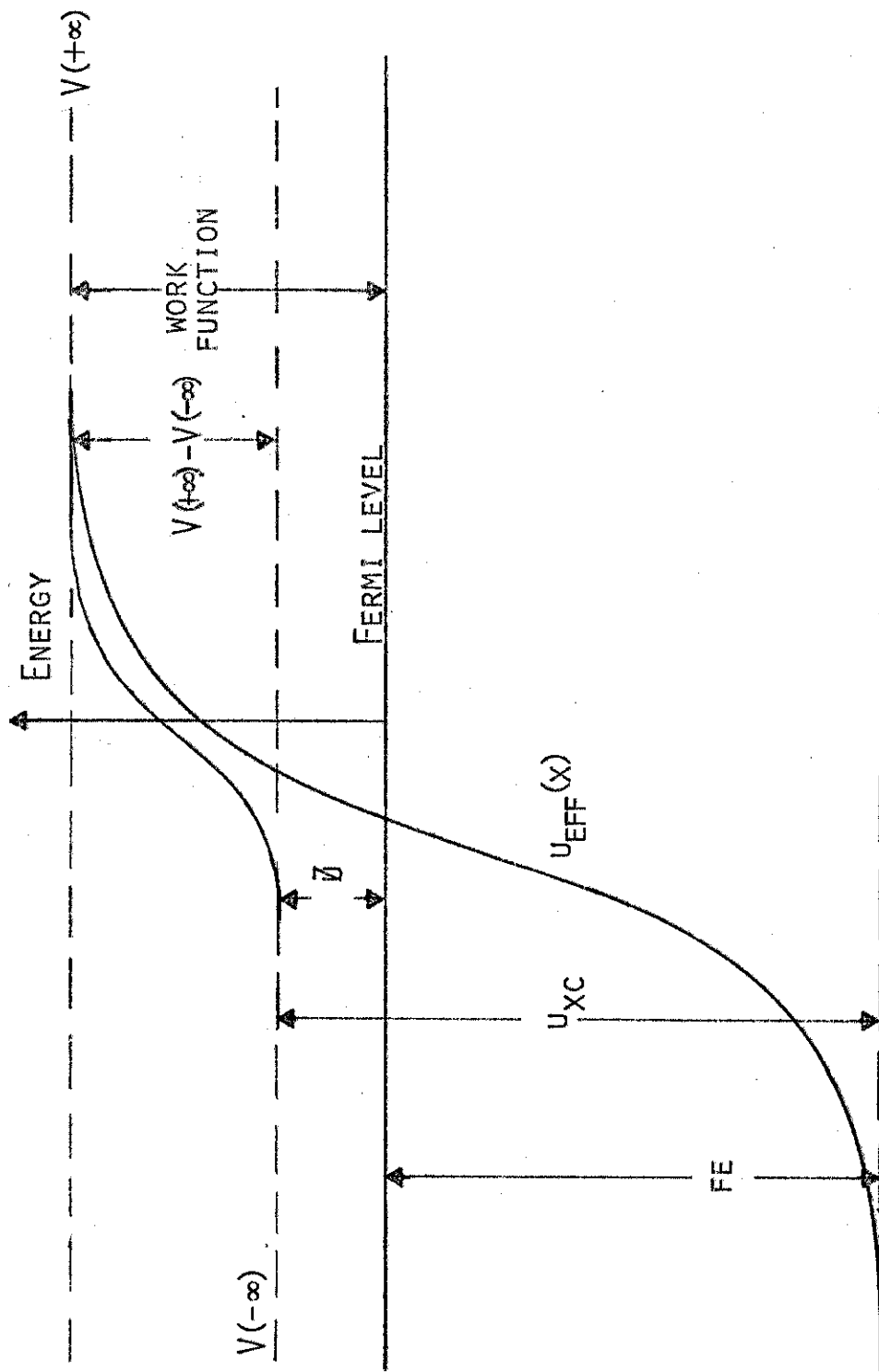
Fig. 3. Energies Pertaining to Work Function Definition. Relative energy scale was adjusted to give ratios of the quantities indicated which were that obtained by Lang and Kohn for gold.

between μ_{xc} and $\bar{d}V_E$. But regardless of this difficulty,
their calculations have shown in a definite way the relative
magnitudes of the two major contributing terms to the work
function. In addition, this insight into how the work
function energy is generated will later prove useful in
interpreting the effects of absorbed molecular species on
the values of the work function.

There remains one further significant question about
the electron structure at a metal-vacuum interface: For
purposes of a tunneling experiment, what is the potential
energy of an electron one to ten nm outside a metal surface?
A related question which must also be answered is: Where
is the effective metal surface? Both questions are addressed
in LKIII. By solving Eqs. 2.5 and 2.6 self-consistently,
an $N(\underline{r})$ is calculated from a U_{eff} determined by the sum
of the energies due to the distribution of Eq. 2.7, a point
charge outside the metal surface, and a weak external electric
field F. The unperturbed charge distribution produced by
the charge density of Eq.2.7 is then subtracted from this
result to obtain a screening charge density $N_S(x)$. The
potential energy of an electron outside the surface in the
presence of a weak uniform electric field pointing out of
the metal is then calculated as the interaction energy between
the potential of the point charge, q, and its induced
screening charge. The result for a charge located at the
position x_1 is to order $(x_1 - x_0)^{-3}$ given by

$$V_{IP}(x) = \text{const} - q^2/(4\ pi\acute{e}_0(x_1-x_0)) - qE(x-x_0). \qquad (2.25)$$

The center of mass of the induced screening charge, x_0, is defined by

$$x_0 = \int x\ N_s(x)dx\ /\ \int N_s(x)dx. \qquad (2.26)$$

For small fields, the center of mass of the induced screening charge is approximately the same as that for the point charge. The answer to the first question posed is, therefore, that the potential to a good approximation is the classical image potential referred to a plane passing through x_0. Relative to the edge x_B of the uniform positive-charge background, the position x_0 is determined by $x_0 - x_B = 0.076$ nm for an $r_s = 3$ i.e. gold's electron density. This value was obtained by interpolating between the values of $x_0 - x_B$ given in LKIII for $r_s = 2$ and $r_s = 4$.

In connection with the problem of determining the potential at a metal surface, field penetration effects are often considered to be a significant factor. As pointed out by Lang and Kohn, the analog here of penetration effects is just the fact that the induced charge distributions have finite widths.

A definite answer for the second question is not as easily obtained. Locating x_B of the positive background model relative to the lattice of the metal is the problem. The approach taken in LKIII was to locate, somewhat arbitrarily, x_B at a point one-half an interplanar spacing in front

of the last plane of ions. A justification for this assign-
ment can be obtained from the self-consistent calculations
by Applebaum and Hamann[22] for the Na (100) surface in which
the lattice properties and atomic nature of the surface
were treated at the same level of detail as is common in
bulk calculations. They give a figure which shows the effec-
tive potential and charge density in much the same manner
as Fig. 2, with the ion core locations shown. Taking the
point at which the electron charge density has dropped to
one-half the bulk value as the proper place to locate the
positive-background edge gives the x_B value assumed by LKIII.

In summary, the electron potential outside a gold sur-
face is given by Eq. 2.25 with x_0 located at a point one-half
an interplanar spacing plus 0.076 nm in front of the last
plane of ions (see Fig. 4). This along with U_{eff} is sufficient
information to determine the potential between two gold elect-
rodes in vacuum.

However, the effective spacing between the electrodes
for tunneling is reduced even more than twice the sum just
given since the tunneling distance will, as shown later, be
determined primarily by the distance between the points of
the electrodes at which $U_{eff} = FE$. For gold (see Fig. 2)
the effective tunneling surface, by this convention, would
be located 0.105 nm plus one-half an interplanar spacing in
front of the last plane of ions. For an interplanar spacing,

EFFECTIVE

METAL SURFACES

←—1/2 d

d

0.076 →
nm.

ELECTRODE I   ELECTRODE II
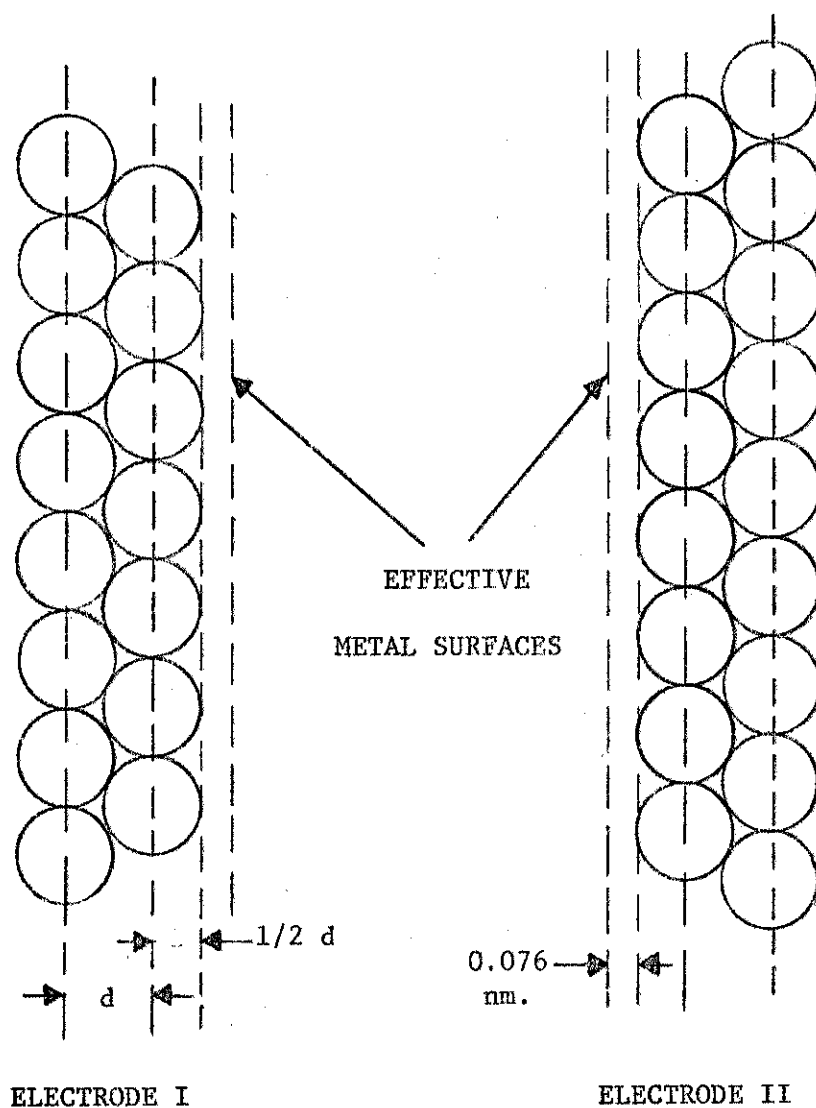
Fig. 4. Location of Effective Metal Surfaces. Diagram
is drawn to illustrate simple model of two identical gold
electrodes with the atoms spaced at the nearest-neighbor dis-
tance in a gold crystal. The electrode spacing shown would
correspond to a lattice separation of approximately 1.47 nm;
the nearest-neighbor distance was assumed to be 0.288 nm.

d, the location of the gold surface for tunneling, x_s, rela-
tive to the location of the last plane of ions, x_i, is
therefore

$$x_s = x_i + (x_B-x_i) + (x_0-x_B) + t \qquad (2.27)$$

or,

$$x_s = x_i + 0.5d + 0.076 \text{ nm} + t, \qquad (2.28)$$

where t is the distance from x_0 to where $U_{eff} = FE$; the
positive x direction is out of the metal surface.

At large, positive x, $U_{xc}[N(\underline{r})]$ is thought to become
the classical image potential $[U_{xc}(x) - (e^2/4 \text{ pi } \not{e}_0 x)]$.[14,22]
However, no form of the exchange and correlation potential
has as yet been put forth which has the expected asymptotic
functional dependence on x. The transition of an electron
from inside a metal in the presence of many other electrons
where energy changes result from electrons of like spin
avoiding each other (exchange) and electrons of either spin
avoiding each other to minimize the coulomb energy (correla-
tion) to a region in vacuum where at least the correlation
is an insignificant factor has been extremely difficult to
model. The slowly varying density approximation for $e_{xc}[N]$
given in Eq. 2.9 leads to an effective exchange and correlation
potential which vanishes exponentially as x goes to infinity
(see LKI). A control calculation was performed in LKI by check-
ing the self-consistent results against that obtained when
the image potential (1/x) form was used for x values greater

than the point where U_{eff} = FE. Differences in N(x) obtained

with the two potentials were no greater than 0.3% for r_s = 2.5

The more commonly used Slater X-α approximation for the

exchange and correlation potential varies as $N(x)^{1/3}$. With

reasonable N(x)'s it also vanishes much more rapidly than

1/x as x goes to infinity.[23]

<p style="text-align:center">The Barrier Potential Energy Function</p>

In this section and the following section on the tunnel-

ing process, the tunneling device is assumed to be composed

of two semi-infinite metal electrodes with plane parallel faces

separated by a vacuum space. The parallel faces are taken to

be normal to the x axis with electrode II located further along

the positive x direction than electrode I.

Assume first that the electrodes are in equilibrium with

each other. Then, the chemical potentials of the two elec-

trodes will be equal [24] and Eq. 2.19 gives

$$V_E^I(-\infty) + FE^I + \mu_{xc}^I(N_a^I) = V_E^{II}(-\infty) + FE^{II}$$
$$(2.29)$$
$$+ \mu_{xc}^{II}(N_a^{II}).$$

The superscripts denote the electrode labels. When the

electrodes are not contacting this condition combined

with the definition of the work function in Eq. 2.20 requires

that

$$V_V = V_E^I(+\infty) - V_E^{II}(+\infty) = WF^I - WF^{II}. \qquad (2.30)$$

Thus, if the two electrodes have different work functions, the equilibrium condition is for there to exist an electrostatic potential difference between their surfaces. This potential difference is usually known as the Volta or contact potential[25]. Recent work by Bennett and Duke[26] has, however, shown that the name contact potential would be inappropriate since they conclude that when the metals are in contact, the junction potential, V_J, is

$$V_J = FE^I + \mu_{xc}^I(N_a^I) - [FE^{II} + \mu_{xc}^{II}(N_a^{II})]. \qquad (2.31)$$

This result interpreted in terms of Eq. 2.29 means that when the electrodes are in contact, their background electrostatic potential, $V(-\infty)$, are constrained to be equal; a very reasonable conclusion. Bennett and Duke's[26] arguments are not based on Eq. 2.29. Their results follow from solutions to Schrodinger's and Poisson's equations with appropriate boundary conditions.

The problem of describing the transition between the conditions specified by Eqs. 2.30 and 2.31 has, unfortunately for use in a general vacuum tunneling configuration, not been investigated. For the particular configuration, i.e., with almost identical gold electrodes, used in the experiments of this work the effects from both V_J and V_V were minimal. In the following discussion, V_V and V_J are assumed to be zero for the gold-vacuum-gold tunneling experiment.

Assuming equal Fermi energies and work functions in the two electrodes, the barrier potential energy function, $V_B(x)$ at equilibrium is, following the conventions of Fig. 3 given by

$$V_B(x) = FE + WF + V_{IP}(x), \qquad (2.32)$$

where $V_{IP}(x)$ is the image potential of a point charge between two conductors with plane parallel faces. The energy zero is assumed to be such that $V_E^I (-\infty) + \mu_{xc}^I(n_a^I) = 0$. The classical image potential 2.25 is employed because of the difficulties given earlier about the incorrect extrapolations of available forms of the exchange and correlation potentials. In vacuum, the classical double image potential energy function is [27]

$$V_{IP}(x) = -(e^2/8 \text{ pi } \epsilon_0)\{(1/2x) \\ + [(n=1,\infty) [ns/(n^2s^2-x^2)-(1/ns)]\}. \qquad (2.33)$$

s is the distance between the faces of the two conductors and x is the coordinate relative to an origin at the face of electrode I. To facilitate numerical calculations, a simpler approximate form of Eq. 2.33 obtained by Simmons[27] will be used. The approximate form is

$$V_{IP}(x) = -1.15(\ln 2)e^2 \text{ s}/[8\text{pi}\epsilon_0 x(s-x)]. \qquad (2.34)$$

With s and x expressed in nm and $V_{IP}(x)$ in electron volts (eV), Eq. 2.34 reduces to

$$V_{IP}(x) = -0.2867 \ s/[x(s-x)].\qquad(2.35)$$

Plots of $V_B(x)$ with the V_{IP} of Eq. 2.35 and assumed electrode Fermi energies of 5.5 eV and work functions of 5.0 eV for s values ranging from 0.2 nm to 5.0 nm are given in Figs. 5 and 6. Note that in these figures, the vacuum level is at an energy of 10.5 eV. These graphs demonstrate that as the electrode spacing decreases, the maximum barrier height drops by more than one electron volt when s = 1.0 nm; when s = 0.23 nm, the maximum barrier height has dropped to the Fermi energy of 5.5 eV. This is coincidentally about equal to the nearest-neighbor distance for the gold lattice.

For the barrier potential energy function plotted in Figs. 5 and 6 to correspond with the surface location described by Eq. 2.28 and the corrections to the classical image potential given in Eq. 2.25, the x = 0 and x = s positions would correspond to the x_o described by these equations. While t, the distance from x_o to the x value at which U_{eff} = FE, was found in LKIII to be 0.029 nm for gold, the value obtained from Fig. 5 is approximately 0.06 nm. Neglecting for the moment the possible effects of nonzero t, the modifications of Eq. 2.25 and 2,28 mean that tunneling currents calculated from the barrier potential with a spacing parameter s should correspond to a true physical spacing, s_T,

$$s_T = x_i^{II} - x_i^{I} = s + d + 0.152 \text{ nm}.\qquad(2.36)$$

The importance of Eq. 2.36 will be discussed in chapter IV
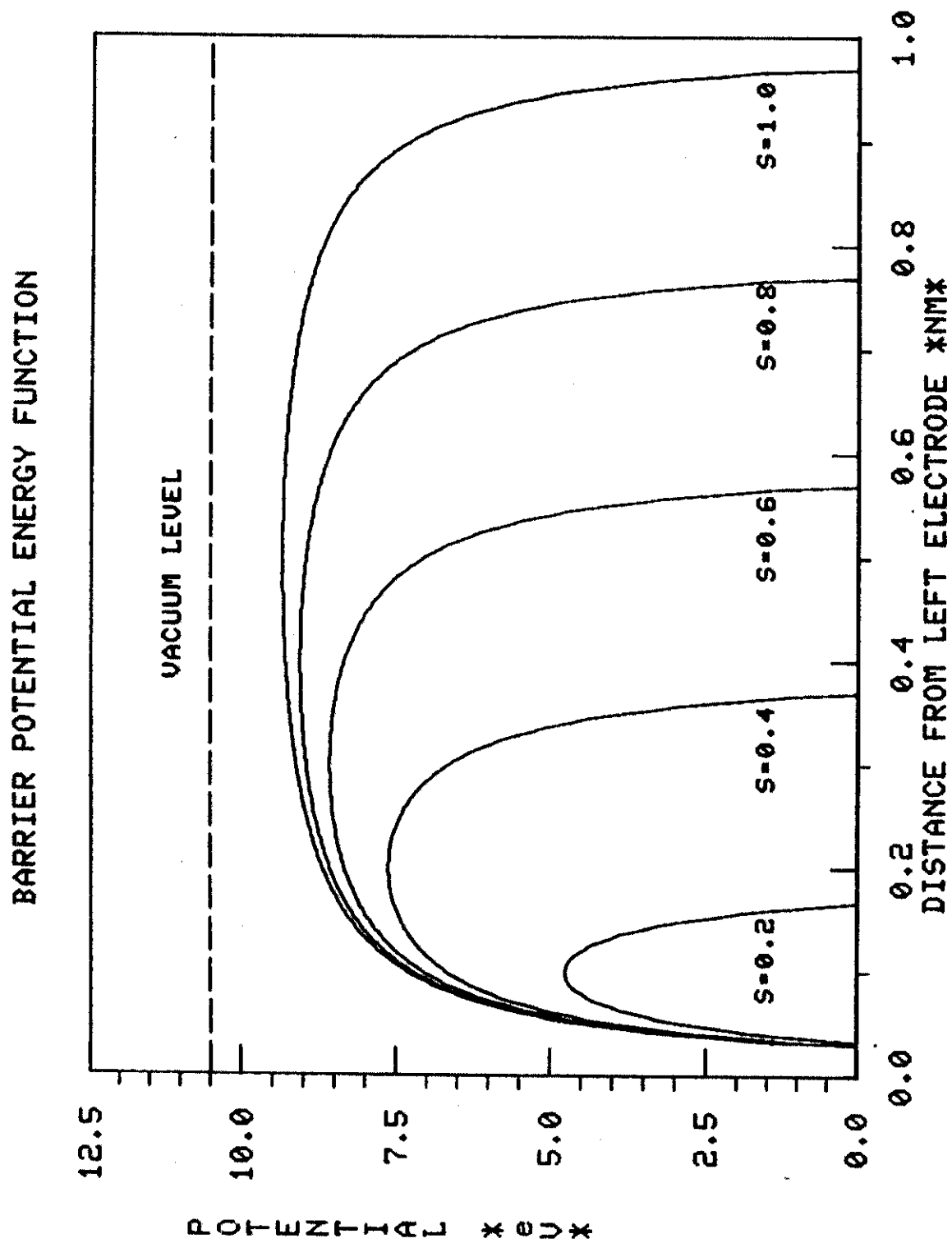
Fig. 5. Barrier Potential Energy Vs. Electrode spacing. S is in units of nm.
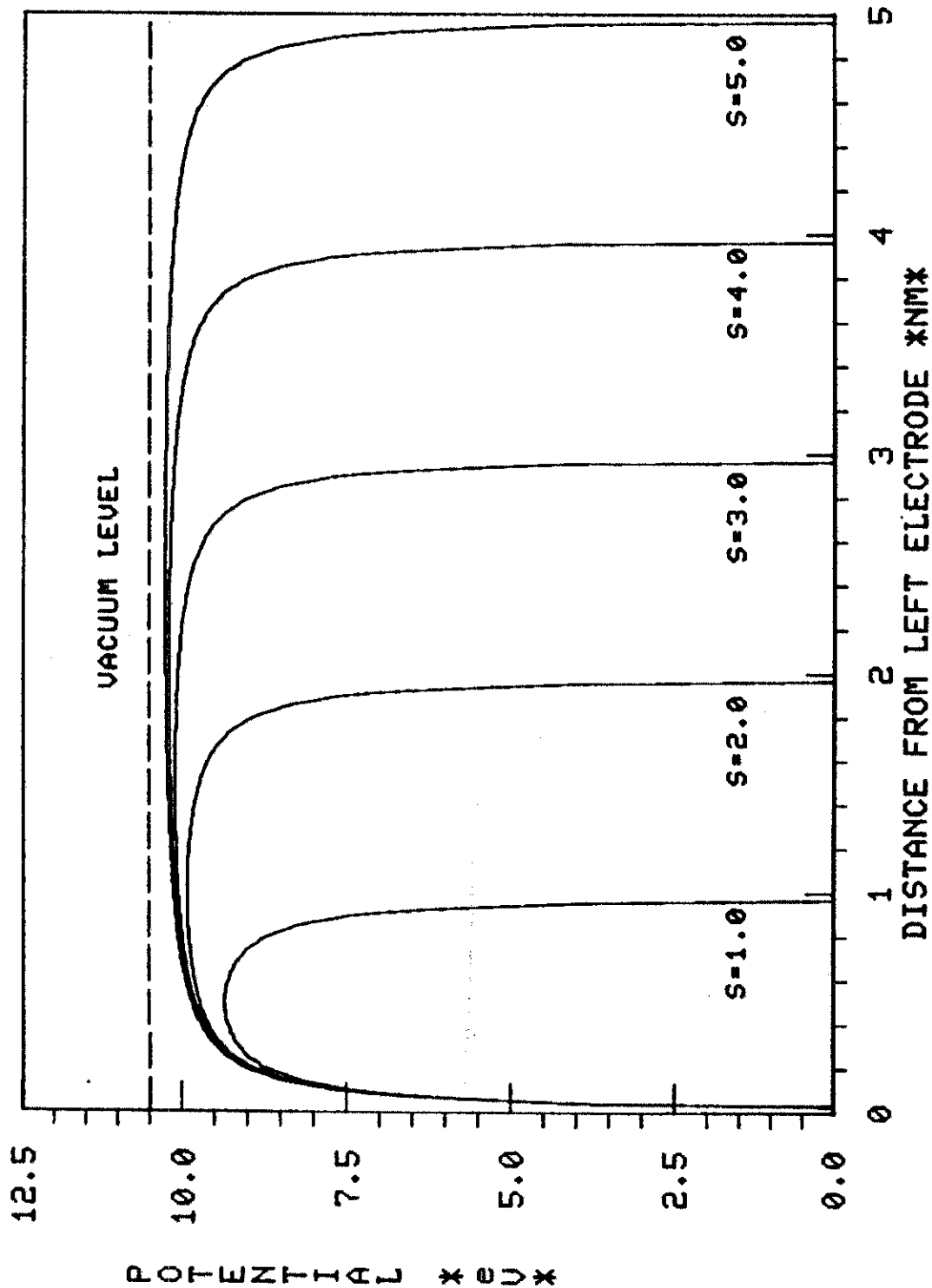
Fig. 6. Barrier Potential Energy Vs. Electrode spacing. S is in units of nm.

when an attempt is made to relate the calculated current values to measurements.

When the positive terminal of a battery of potential V is connected to electrode II and the negative terminal to electrode I, the mean electrostatic potential, for negative charges, of electrode II is lowered by an energy of eV relative to that in electrode I. Since the FE and μ_{xc} are fixed by the electron density, the Fermi level is also lowered by an energy eV. Combining the barrier potential energy function with this effect and assuming the field between the electrodes is uniform, gives a potential energy function for the metal-vacuum-metal system which can be subdivided into three areas of interest:

Region I: $V_T(x) = 0$ $x \gtrless x^I$

Region II: $V_T(x) = -eV$ $x^{II} \geqq x$ (2.37)

Region III: $V_B(x) = FE + WF - eVx/s + V_{IP}(x)$ $x^I > x > x^{II}$,

x^I and x^{II} are the values for which $V_B(x)$ is equal to 0 and -eV respectively. Fig. 7 is a schematic illustration of Eq. 2.37 combined with the concepts of Fig. 3 concerning the work function. The shaded areas of the diagram represent eigenstates that are occupied when the electrodes are at zero temperature.
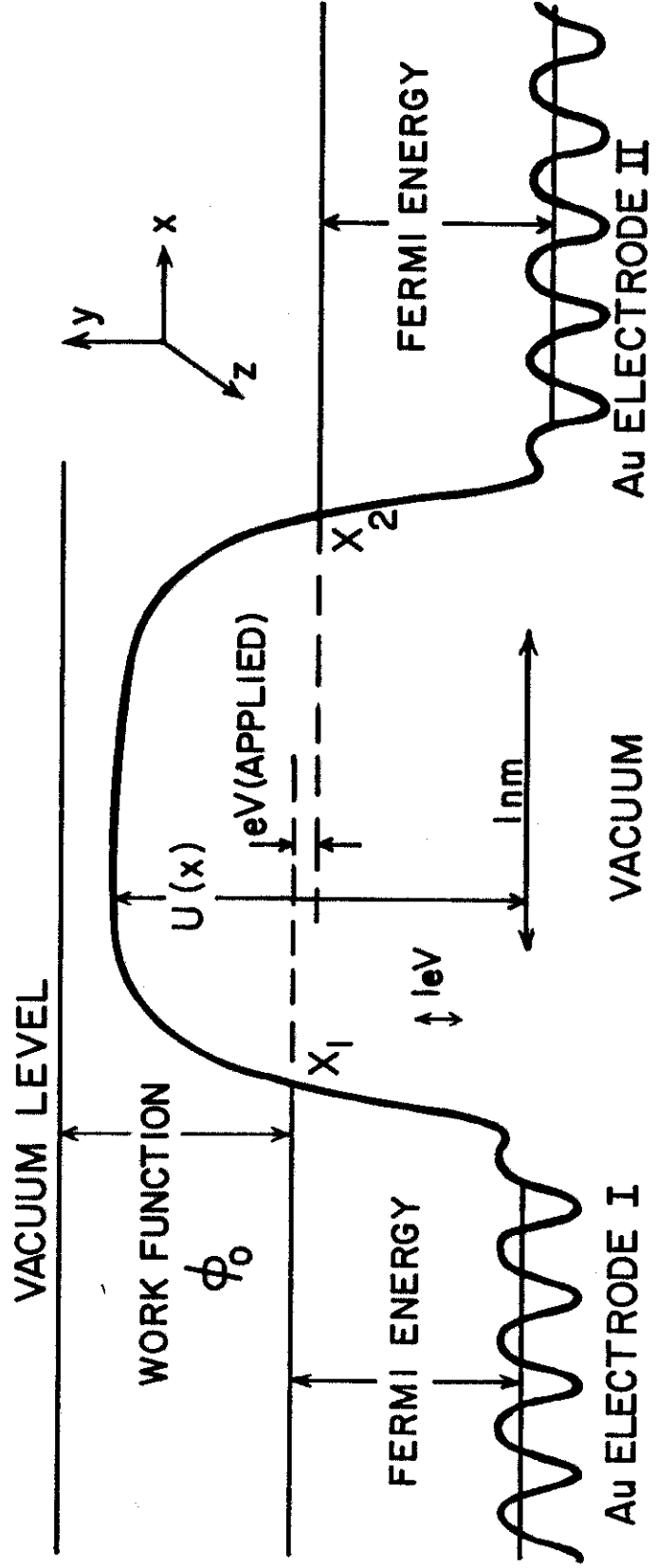
Fig. 7. Energy Diagram for Metal-Vacuum-Metal Tunneling. Energy and distance in the diagram are drawn to scale for the quantities represented. The small oscillations of the energy at the bottom of the occupied states represent the magnitude and spacing of the ion-core potentials. X_1 and X_2 are the classical turning points for an electron near the Fermi energy.

The Tunneling Process

From this point onward in the theoretical development
no further attempt will be made to account for many-electron
effects on the calculated tunneling current. All the previous
work to account for many-electron effects was required since,
as shown, the dominant sources of the work function originate
from electron-electron interactions and their effects on the
electron distribution at a metal surface. A fully independent-
electron model of the electrodes and of the tunneling process
will be used in the remainder of this chapter. There were two
major reasons for this decision. First, at the resolutions
of I-V measurements anticipated for this experiment, the small
changes in current due to electron-electron interactions,
electron-phonon interactions, and self-energy changes produced
by transition through the barrier would not be observable. The
changes are usually less than one percent. Second, within the
limitations of the independent electron model, the stationary
state method of current-carrying states is a well defined and
convenient procedure for calculating current flow in quantum
systems[28, 29].

For an electron described by one of the solutions, $\Psi_k(\underline{r})$,
to the time-independent Schrodinger equation for the potential
$V_T(x)$

$$[-\hbar^2/2m + V_T(x)]\Psi_k(\underline{r}) = E(\underline{k})\Psi_k(\underline{r}), \qquad (2.38)$$

the electron current density flow is given by [29]

$$\underline{J}(\underline{k},\underline{r}) = (-ie\hbar/2m)(\Psi_{\underline{k}} \text{grad} \Psi_{\underline{k}}^* - \Psi_{\underline{k}}^* \text{grad} \Psi_{\underline{k}}), \qquad (2.39)$$

where * denotes the complex conjugate operation. The standard
interpretation of Eq. 2.39 is that $\underline{J} \cdot \underline{n}$ is the probability
per unit time that a charge -e will flow through the unit
area with normal $\underline{n}$. Since the electrons occupying the states
$\Psi_{\underline{k}}(\underline{r})$ are assumed to not interfere with each other, the total
current density is just the sum of the current density contri-
butions from each eigenstate of the metal-vacuum-metal system
which is allowed by the Pauli exclusion principle.

The non-equilibrium aspects of a biased junction are
usually treated by assigning different thermal occupational
probability functions to each metal with the reference
energies offset by the applied voltage and differences in
Fermi energies. Thus, with $V^I(-\infty) + \mu_{xc}^I$ as the reference
energy zero and a positive polarity voltage, V, connected
to electrode II, the energies in the two electrodes would
be related by the energy conservation equation:

$$E_I = E_{II} + FE_I - FE_{II} - eV. \qquad (2.40)$$

For a net current to flow, occupied states on one side of the
barrier must exist at the same energy as empty states on
the other. In Fig. 7, the applied voltage will establish,
at zero temperature, empty states in electrode II opposite
filled states with the same energy in electrode I. Therefore,

in this instance, electrons would dominantly flow from elec-
trode I to electrode II by tunneling through the barrier,
i.e., via a current-carrying stationary state which existed
in all three regions of the system. The current density is
computed as the difference between the current density flowing
from I to II and II to I.

The thermal occupatonal probabilities are given by the
Fermi-Dirac distribution

$$f(E) = (1 + \exp[(E - FE)/k_B T])^{-1} \qquad (2.41)$$

where E is the energy eigenvalue, k_B is Boltzmann's constant
and T is the system temperature. Eq. 2.40 combined with
Eq. 2.41 gives the result

$$f_I(E) = f(E)$$
$$f_{II}(E) = f(E+eV). \qquad (2.42)$$

Again, taking the plane of the electrodes to be normal to
the x-direction, the current density, $\underline{J}_{I \to II}$, from I to II
is then given by

$$\underline{J}_{I \to II} = 2 \ [(\underline{k}) \ J^x_{I \to II}(\underline{k}, \ \underline{r}) \ f_I(E)[1-f_{II}(E)]. \qquad (2.43)$$

The factor of 2 is to account for the additional states
produced by the two electron spin orientations. $J^x_{I \to II}$ is the
x component of $\underline{J}(\underline{k}, \ \underline{r})$. Similarly,

$$\underline{J}_{I \to II} = 2 \left[(\underline{k}) \; J_{II \to I}^X(\underline{k}, \; \underline{r}) \; f_{II}(E)[1-f_I(E)] \right]. \quad (2.44)$$

Since $V_T(x)$ is a real potential, the solutions to Schrodinger's equation must obey the general reciprocity theorem of scattering proceses. Blatt and Weisskopf[36] give a succinct statement of the theorem: "This theorem states that the probability for a transition proceeding one way in time is equal to the probability for the same transition, but with the sense of time reversed." The sense of time in Eqs. 2.43 and 2.44 is manifest only in the direction of the wave vector thus, $J_{I \to II}^X(\underline{k}, \; \underline{r}) = J_{I \to II}^X(-\underline{k}, \; \underline{r}) = J_{II \to I}^X(\underline{k}, \; \underline{r})$. The expression for the net current density is therefore

$$J = 2 \left[(\underline{k}) \; J^X(\underline{k}, \; \underline{r}) \; [f(E)-f(E+eV)] \right]. \quad (2.45)$$

To calculate $J_x(\underline{k}, \; \underline{r}) = J^X(\underline{k}, \; \underline{r})$, explicit solutions to Eq. 2.38 for all three regions of $V_T(x)$ must be obtained. The solutions given here will be based on the results obtained by Merzbacher[31] with the use of the Wentzel, Kramers, Brillouin (WKB) approximation technique for solving Schrodinger's equation. If periodic boundary conditons are imposed in the y and z directions, the solutions to Eq. 2.38 may be written as

$$\Psi_{\underline{k}}(\underline{r}) = A^{-1/2} \exp(i\underline{k}_p \cdot \underline{P}) \; M_{k_x}(x), \quad (2.46)$$

where $\underline{k}_p$ and $\underline{P}$ are the wave vector and displacement, respectively, parallel to the electrode faces, k_x is the wave vector component normal to the electrode faces, and A is the

area of the tunneling device. The eigenvalues $E(\underline{k})$ are

$$E(\underline{k}) = (\hbar^2/2m)(k_p + k_x) = (\hbar^2 k^2/2m) \qquad (2.47)$$

Let $x_L(E)$ and $x_R(E)$ be the classical turning points for the energy E at electrode I and electrode II respectively, then with Merzbacher's conventions

$$M_{k_x}(x) = A \; k^{-1/2}(x) \; W_t + B \; k^{-1/2}(x) \; W_- \qquad x \gtreqless x_L(E)$$

$$M_{k_x}(x) = C \; K^{-1/2}(x) \; Z_- + O \; K^{-1/2}(x) \; Z_+ \qquad x_L < x < x_R \qquad (2.48)$$

$$M_{k_x}(x) = F \; k^{-1/2}(x) \; q_+ + G \; k^{-1/2}(x) \; q_- \qquad x_R(E) \gtreqless x,$$

where,

$$W_{\pm} = \exp[\pm i \int_{x_L}^{x} k_x x) dx]$$

$$Z_{\pm} = \exp[\pm \int_{x_L}^{x} K(x) dx] \qquad (2.49)$$

$$q_{\pm} = \exp[\pm i \int_{x_R}^{x} k_x(x) dx]$$

and

$$K(x) = [(2m/\hbar^2)(V_B(x)-(E(k)-\hbar^2 k_p^2/2m))]^{1/2}. \qquad (2.50)$$

With these conventions, Bohm[32] then shows in detail that with the use of connection formulas

$$A = [(1/2)(2\theta + 1/(2\theta)] F \tag{2.51}$$

where
$$\theta = \exp\left(\int_{x_L}^{x_R} K(x)dx\right). \tag{2.52}$$

If now the solution in region I is assumed to be

$$M_{k_x}^{I}(x) = e^{ik_x x} + R\, e^{-ik_x x} \tag{2.53}$$

with R being adjusted for normalization, then the solution in region II is, assuming G = 0,

$$M_{k_x}^{II}(x) = 2[2\theta + 1/(2\theta)]^{-1}\, e^{ik_x(x_L - x_R)}\, e^{ik_x x} \tag{2.54}$$

The conservation of $\underline{k}_p$ and total energy in the tunneling process was implicitly assumed in the calculations from Eqs. 2.46 to 2.54. Since $M_k^{II}(x)$ is the stationary state solution in region II and probability current is "conserved," it may be used as well as the solution in the other two regions to calculate the current density. Substituting Eq. 2.54 into Eq. 2.46 and then the result into Eq. 2.39 gives

$$J_x(\underline{k},\ \underline{r}) = 4[2\theta + 1/(2\theta)]^{-2}\, e\hbar k_x/m. \tag{2.55}$$

Let

$$D(E,\ \underline{k}_p) = 4(2\theta + 1/(2\theta)]^{-2} \tag{2.56}$$

then

$$J_x(\underline{k}, \ \underline{r}) = D(E, \ \underline{k}_p) \ e\hbar k_x/m. \tag{2.57}$$

$D(E, \ \underline{k}_p)$ may be interpreted as a transmission coefficient for the part of the solution in region I into region II.

Substituting Eq. 2.57 into Eq. 2.45 gives the complete expression for the current density J as

$$J = 2e\hbar/m \ \left[(\underline{k}) \ k_x D(E,\underline{k}_p) \ [f(E)-f(E+eV)]. \right. \tag{2.58}$$

The summations are most conveniently carried out by changing to integrations over the variable E_x defined as

$$E_x = \hbar^2 k_x^2/2m = E(\underline{k}) - \hbar^2 k_p^2/2m. \tag{2.59}$$

The conversion is performed with the following three relations: the first is the well known sum to integral conversion in k-space, the second one is based on the free-electron properties expressed in Eq. 2.47 and the third is the differential of Eq. 2.59:

$$\left[(\underline{k}) \quad \right] d^3k/(2pi)^3$$

$$d^2k_p = (2pim/\hbar^2)dE_p \tag{2.60}$$

$$k_x dk_x = (m/\hbar^2)dE_x$$

With these relationships, Eq. 2.58 may be written in the following form:

$$J = \int_0^\infty dE_x \, D(E_x) \, N(E_x) \qquad (2.61a)$$

$$N(E_x) = (4\text{pime}/h^3) \int_0^\infty [f(E) - f(E + eV)]dE_p. \qquad (2.61b)$$

In words this states that the net current density is equal
to the sum of the number of electrons with the "x-part of
their energy" within dE_x that are incident on the surface
of the negatively biased electrode per unit time per unit
area, $N(E_x)dE_x$, times the tunneling probability of an elec-
tron at this energy, $D(E_x)$.

This is the same form of the equations obtained by Duke[33]
and as such is an acknowledgement that his work was frequently
consulted in developing Eqs. 2.61. Another form of Eq. 2.61a
which is more useful for interpreting the energy aspects of
the tunneling process is

$$J = 2e/h \int dE[f(E)-f(E+eV)] \int (2\text{pi})^{-2}d^2k_p \, D(E,k_p). \qquad (2.61c)$$

Eq. 2.61c facilitates the physical interpretation of the
origins of the tunneling current in terms of the overlapping
of energy surface projections onto the tunneling plane and
enables direct connection with energy diagrams such as that
given in Fig. 7. However, calculation of the tunneling
current, particularly for the free-electron model of the
electrodes, is most easily accomplished with the use of
Eq. 2.61a.

Eq. 2.61b may be integrated by parts to obtain

$$N(E_x) = (4 \ mek_BT/h^3) \ln(FDI/FDII),$$

$$FDI = 1 + \exp[(FE-E_x)/k_BT] \qquad (2.61d)$$

$$FDII = 1 + \exp[(FE-E_x-eV)/k_BT]$$

Note that the Fermi energies of the two electrodes have been assumed equal. Collecting all the definitions involved in Eq. 2.56 together for reference gives

$$D(E_x) = 4[2\theta + 1/(2\theta)]^2,$$

$$\theta = \exp(\int_{x_L}^{x_R} K(x)dx), \qquad (2.61e)$$

$$K(x) = [(2m/\hbar^2)(V_B(x)-E_x)]^{1/2},$$

$$V_B(x) = FE+WF-eVx/s-(const)s[x(s-x)]^{-1},$$

$$const = 1.15(Ln2)e^2/8pi\epsilon_o$$

$$= 0.2867(eV \ nm).$$

The accuracy of the WKB approximation for calculating the transmission coefficient has been extensively investigated in the literature of this field. One of the most thorough checks was performed by Politzer[34], who compared values computed with the form

$$D(E) = \exp[-2 \int_{x_L}^{x_R} K(x)dx], \tag{2.62}$$

of the WKB transmission coefficient with those obtained from a numerical solution of Schrodinger's equation using essentially the same V_T as given in Eq. 2.37. Her results show that the WKB result is valid at the fields, i.e. less than 10^8 V/cm, and energies involved in most configurations of the vacuum tunneling experiment, i.e., energies much less than barrier height.

The major difference between the exact results and the WKB approximation was that the exact $D(E)$ was an oscillatory function of energy for energies and fields which resulted in an effective bound state potential well above the top of the barrier. The amplitude of the oscillations in the exact $D(E)$ was relatively small and such that

$$0.5 < Log(D(E)_{WKB}/D(E)_{NUM}) < 0.8 \tag{2.63}$$

for all fields and for energies more than 0.5eV from the top of the potential barrier. Near the Fermi energy, at which the major contribution to the tunneling current occurs, the ratio's mean value was about -0.2. The mean difference between the tunneling current for the two calculations of $D(E)$ was not calculated by Politzer and barrier heights applicable to the vacuum tunneling experiment were not investigated.

Approximate Analytical Expressions For Tunneling Current

In this section, the qualitative properties of the tunneling current will be derived from the zero temperature, low voltage solutions to Eqs. 2.61. The overall character of the tunneling current will be shown to be approximately ohmic with a small cubic dependence on voltage having importance at higher voltages. At all voltages, the tunneling current is found to be exponentially dependent of the electrode spacing. Finally, the zero temperature solutions are extended to finite temperatures and estimates of the effects of room temperature on the tunneling current are given.

The tunneling characteristics determined by Eqs. 2.61 are most easily understood by first investigating the zero temperature behavior. At zero temperature

$$
\begin{aligned}
N(E_x) &= A_T eV, & 0 \lessgtr E_x \lessgtr FE-eV \\
&= A_T(FE-E_x), & FE-eV < E_x < FE \qquad (2.64) \\
&= 0 & FE \lessgtr E_x,
\end{aligned}
$$

A_T is the "thermal" constant $4pi\ me/h^3$. Thus, Eq. 2.61a takes the form

$$
J = A_T[eV \int_0^{FE-eV} D(E_x)dE_x + \int_{FE-eV}^{FE} (FE-E_x)D(E_x)dE_x]. \qquad (2.65)
$$

For large θ in Eq. 2.61e, which for most barriers in tunneling experiments is a true conditon, $D(E_x)$ can be approximated by the form given in Eq. 2.62. Simmons[35] has proposed an average barrier height method to further simplify $D(E_x)$. His approach

is to approximate the integral in Eq. 2.61e over $K(x)$ with an average barrier height, B, above the Fermi level of the negatively biased electrode, i.e., he defines B as

$$B = W^{-1} \int_{X_{LF}}^{X_{RF}} V_B(x)dx, \qquad (2.66)$$

where x_{LF} and x_{RF} are the classical turning points for $E_x = FE$, and $W = x_{RF} - x_{LF}$ is the width of the barrier at this energy.

With this definition, Simmons[35] shows that for voltages less than about one volt

$$D(E_x) = \exp[-aW(FE + B-E_x)^{1/2}], \qquad (2.67)$$

$a = (4\ pi/h)(2m)^{1/2} = 10.25(eV)^{-1/2}\ nm^{-1}$. By utilizing this $D(E_x)$, an approximate low voltage tunneling current density can be calculated from Eq. 2.65. Let $N = FE-E_x$ and $p = aWB^{1/2}$, then, Eq. 2.65 may be written as

$$J = A_T \left\{ -eV \int_{FE}^{eV} \exp[-p(1+N/B)^{1/2}]dN \right.$$

$$\left. - \int_{eV}^{0} N\ \exp[-p(1+N/B)^{1/2}] \right\}dN. \qquad (2.68)$$

For small voltages, N/B, will be much less than one, so the approximation $(1+N/B)^{1/2} = (1+N/2B)$ may be used. The

integrals may then be evaluated to obtain the result:

$$J = A_T \left\{ 4e^{-p}/(aW)^2) (1-\exp[-aWeV/(2B^{1/2})]) \right\}. \quad (2.69)$$

Only a factor of $\exp(-a\ W\ FE/B^{1/2})$ was neglected to obtain Eq. 2.68. If one takes just the leading term in the series for the exponential, the following result for the tunneling current density at low bias voltages and zero temperature is obtained:

$$J_L(T=0) = J_{OL} \exp(-p)V, \quad (2.70)$$

where $J_{OL} = [(2m)^{1/2}/W](e/h)^2\ B^{1/2}$.

If B is expressed in electron volts and W in nm, J_{OL} is

$$J_{OL} = 3.16 \times 10^{13}\ B^{1/2}\ W^{-1}(\ A/m^2/V). \quad (2.71)$$

By evaluating Eq. 2.68 in a more exact manner, Simmons[35] derives a general formula for the current density at zero temperature. The formula and its associated relations are given below in what has been found to be a consistent algebraic form, which due to misprints etc. is not correct in published forms. It is given here because it will be used for comparing with the numerical results of the next section. With the same definitions given in Eqs. 2.66 and 2.67, the formula is

$$J(T=0) = J_0\ (B\ \exp(-aWB^{1/2})-(B+eV)\exp[-aW(B+eV)^{1/2}]), \quad (2.72a)$$

$$J_0 = e(2pi\ h)^{-1}\ W^{-2} = 6.2 \times 10^{12}W^{-2}(A\ nm^2)/(m^2 \cdot eV)$$

Based on Eq. 2.66, the analytic approximation for B including image potential effects is

$$B = WF - (V/2S)(S_1 + S_2) - [0.286/(S_2 - S_1)]$$
$$X \ln[S_2(S - S_1)/(S_1(S - S_2))] \qquad (2.72b)$$

S = electrode spacing in same sense as previously discussed.

$S_1 = 0.3/WF$

$S_2 = S[1 - 2.3/(3WFS + 10 - 2Vs)] + S_1.$

In Eq. 2.72b, the work function should be expressed in electron volts and all distances involved in nanometers.

Eq. 2.72a reduces, after some algebra, quite easily to Eq. 2.70 by expanding both exponentials in a series and neglecting terms containing V^2 and higher orders. However, if one keeps all terms out through V^3, it is found that the quadratic terms cancell to give the next higher order approximate result[8]. For identical electrodes

$$J(T=0) = J_{OL}[V + (j_3S^2/B)V^3], \qquad (2.73a)$$

with

$$j_3 = (pi^2me/h^2) = 3.27 \ Volt^{-1}nm^{-2}. \qquad (2.73b)$$

This value of j_3 was taken from the results of Brinkman, et al[8] who expanded Eqs. 2.61 in powers of the voltage and obtaining approximate expressions for the coefficients of the linear and quadratic terms of the conductance. They considered Eq. 2.73b to be accurate to within 10% for S

greater than one nm for trapezoidal shaped barriers. An earlier value obtained by Simmons[36] for the same conditions was $j_3 = 1.15$ Volt^{-1}nm^{-2}. No calculations of j_3 with image potentials corrections are available in the literature. In spite of this ill-known constant, the qualitative behavior predicted by Eq. 2.73a has been fairly well established in many different experiments[37, 38, 8].

In summary, the ideal tunneling characteristics are then as follows.

1) Current density varies exponentially with electrode spacing, with an exponent of, -10.25 X mean barrier height in electron volts X electrode spacing in nanometers.

2) The current-voltage characteristic should be symmetric for identical electrodes. [This just serves as check on formalism or the experimental method since it must be true if the electrodes are truly identical.]

3) For low voltages, the current-voltage characteristic is approximately ohmic.

4) For voltages up to the work function, the non-ohmic conduction should be dominantly a cubic function of the applied voltage, with higher order terms becoming more important as the voltage is increased up to the work function.

The extension of the previous results to finite temperatures is the last topic to be discussed in this section. If

the approximations which led to Eq. 2.68 are substituted into Eqs. 2.61, the following result is obtained:

$$J(T) = A_T k_B T \exp(-aWB^{1/2})$$

$$x \int_{FE} \ln(FDI/FDII) \exp(-aWN/2B^{1/2})dN,$$

(2.74)

where again $N = FE-E_x$. When $k_B T$ is less than $2B^{1/2}/aW$, the integral may be evaluated by the techniques of Murphy and Good[39] to obtain

$$J(T) = A_T Q^{-2}[\ Qk_B T/\sin(pi\ Qk_B T)]$$
$$x \exp(-p)[1-\exp(-QeV)],$$

(2.75)

where $Q = (1/2)aWB^{-1/2}$. For T approaching zero, the factor in the first bracket goes to one, and Simmons[35] shows that the remainder of the terms are equal to $J(T=0)$. Therefore

$$J(T)/J(T=0) = Qk_B T/\sin(pi\ Qk_B T).$$

(2.76)

Q is typically less than $4(eV)^{-1}$. The argument of the sine is therefore much less than one at room temperature. The series expansion gives

$$J(T)/J(T=0) = 1+(1/6)(pi\ Qk_B T)^2$$

or in practical units

(2.77)

$$J(T) = J(T=0)(1+[3x10^{-11}(eV/nm^2/\ K^2)(WT)^2/B]).$$

For W=1 nm, T=300 K, and B=2eV; J(T)=1.013 J(T=0). Such
small changes in the tuneling current would not be detectable
with the present experiment. No significant effect from con-
ducting the experiment at room temperature was therefore
anticipated.

Numerical Calculations of Tunneling Current

In order to facilitate the analysis of measured I-V
and I_{cv}-S tunneling data, the following calculations, based
on Eqs. 2.61 were performed. The results are given in
accompanying figures and tables.

1. The product of $D(E_x)$ $N(E_x)$ as a function of E_x
for four voltages; 0.001, 0.010, 0.10, and 1.0 V, at
each of three electrode spacings; S=0.3, 1.0, and 2.0 nm.
See Figs. 8, 9, and 10.

2. For a simple model of the tunneling between spherical
electrodes, described below, calculations of the tunneling
current density and current were made for a fixed bias
voltage of 0.1 V as a function of electrode spacing and
work function. Computation times were long for the current
calculations, 15 seconds per data point, so only a limited
number were obtained. These results are given in Table 1,
and Figs. 11 through 17. The graphs in Figs. 11 and 12
were at first plotted in a normalized form, but after
finding that much information was lost because of the large
orders of magnitude changes between graphs, the four separate
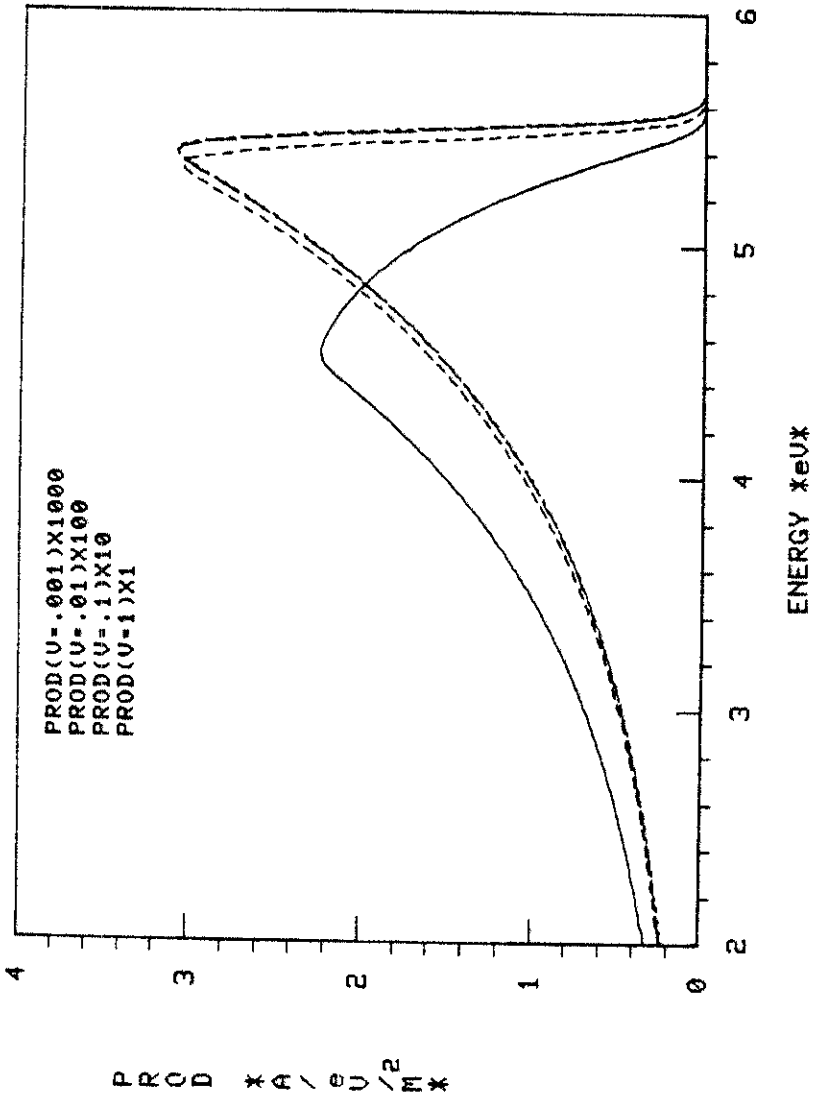
Fig. 8. Distribution of Energy Associated with Normal Component of the Tunneling Electron Momentum; Electrode Spacing of 0.3 nm. The Fermi energy, FE, and the work function, WF, are in units of electron volts.

Fig. 9. Distribution of Energy Associated with Normal Component of the Tunneling Electron Momentum; Electrode Spacing of 1.0 nm. The Fermi energy, FE, and the work function, WF, are in units of electron volts.

PROD VS. ENERGY   T=300.   FE=5.5   WF=5.0   D=2.0

PROD(V=.001)X1000
PROD(V=.01)X100
PROD(V=.1)X10
PROD(V=1)X1
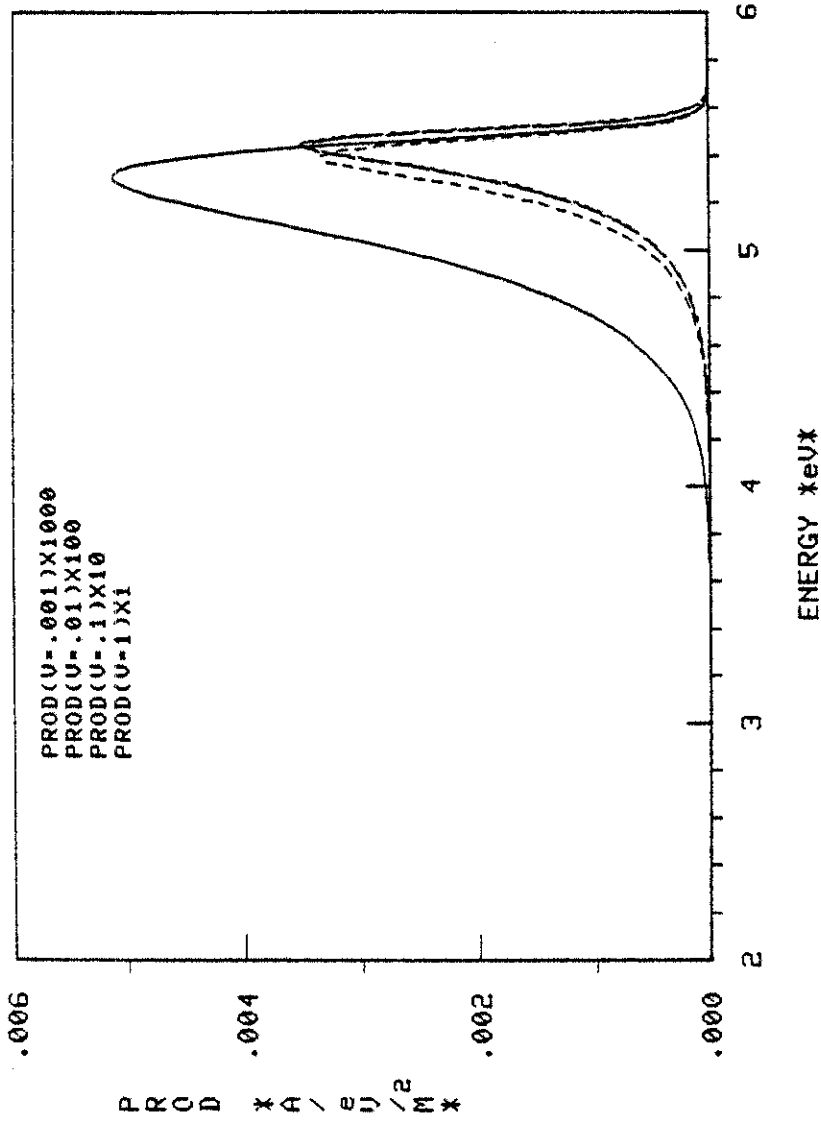
ENERGY *eV*

Fig. 10. Distribution of Energy Associated with Normal Component of the Tunneling Electron Momentum; Electrode Spacing of 2.0 nm.   The Fermi energy, FE, and the work function, WF, are in units of electron volts.

TABLE 1

TUNNELING BETWEEN IDENTICAL SPHERICAL ELECTRODES

CURRENT AND CURRENT DENSITY VERSUS ELECTRODE SPACING AND WORKFUNCTION

BIAS VOLTAGE = 0.1 VOLT
TEMPERATURE = 300 DEGREES KELVIN
FERMI ENERGY = 5.5 ELECTRON VOLTS

ELECTRODE SPACING (NM)	...WF=4.0 EV....		...WF=4.5 EV....		...WF=5.0 EV....		...WF=5.5 EV....	
	CURRENT (A)	CURRENT DENSITY (A/MxM)	CURRENT (A)	CURRENT DENSITY (A/MxM)	CURRENT (A)	CURRENT DENSITY (A/MxM)	CURRENT (A)	CURRENT DENSITY (A/MxM)
.3	.256+01	.924+13	.155+01	.627+13	.955+00	.424+13	.601+00	.287+13
.4	.420+00	.168+13	.210+00	.918+12	.110+00	.515+12	.601-01	.297+12
.5	.610-01	.253+12	.262-01	.117+12	.120-01	.567+11	.576-02	.287+11
.6	.852-02	.357+11	.319-02	.143+11	.128-02	.609+10	.546-03	.273+10
.7	.118-02	.495+10	.384-03	.173+10	.136-03	.648+09	.514-04	.258+09
.8	.161-03	.680+09	.460-04	.207+09	.144-04	.685+08	.481-05	.242+08
.9	.218-04	.926+08	.547-05	.247+08	.151-05	.721+07	.449-06	.226+07
1.0	.295-05	.126+08	.649-06	.294+07	.158-06	.756+06	.418-07	.211+06
1.1	.398-06	.169+07	.766-07	.347+06	.165-07	.790+05	.388-08	.196+05
1.2	.534-07	.228+06	.902-08	.410+05	.171-08	.823+04	.360-09	.181+04
1.3	.716-08	.306+05	.106-08	.482+04	.178-09	.856+03	.333-10	.168+03
1.4	.956-09	.409+04	.124-09	.566+03	.185-10	.889+02	.307-11	.155+02
1.5	.127-09	.545+03	.146-10	.663+02	.191-11	.921+01	.283-12	.143+01
1.6	.170-10	.727+02	.170-11	.775+01	.198-12	.954+00	.261-13	.132+00
1.7	.226-11	.966+01	.199-12	.906+00	.205-13	.986-01	.240-14	.122-01
1.8	.299-12	.128+01	.232-13	.106+00	.211-14	.102-01	.221-15	.112-02
1.9	.397-13	.170+00	.270-14	.123-01	.218-15	.105-02	.203-16	.103-03
2.0	.526-14	.226-01	.314-15	.143-02	.225-16	.108-03	.187-17	.946-05

44)

graphs were chosen as the more useful representation. Fig. 11
shows the changes in curvature or lack thereof in the I-V
characteristic as a function of work function for a fixed
spacing of 2000 pm. Fig. 12 shows the increase in curvature
of the I-V characteristic as a function of electrode spacing
for a fixed work function of 4.5 eV. Figs. 13-17 are
graphs of the data in Table 1 and enable a comparison of
the current and current-density so that the tunneling area
may be estimated.

3. The tunneling current density for a wide range of
voltage and electrode spacing; $V = Nx0.05$ volts, $N = 1$ to
12 and $S=(0.3 + M \times 0.1)$nm, $M = 0$ to 27. See Table 2.

4. As a cross-check on the correctness of the
numerical calculations and to determine the correct form
of Simmons' equations, Eqs. 2.72 and 2.77 were used to
compute the tunneling current density as a function of
electrode spacing and bias voltage. The results are
given in Table 3 and demonstrate that his theory gives
values which are surprisingly close to those of the
numerical calculations.

The product $D(E_x)$ $N(E_x)$ is known as the normal-energy
distribution[40], and is the distribution of tunneling electrons
in energy associated with the component of momentum normal
to the electrode faces. The normal-energy distributions were
calculated and plotted to give insight into the thermal
distributions and barrier transmission aspects of the tunneling

process. Interpretation of Figs. 8, 9, and 10 in terms of
the Pauli exclusion principle and the energy diagram of
Fig. 7 is difficult. For a <u>total</u> energy distribution, the
graphs should have a sharp peak at the Fermi level of the
negatively biased electrode and have a width equal to the
bias voltage with some small amount of thermal smearing at
both edges. Plots of the total energy distribution for
tunneling in Al-GaSe-Au structures are given by Kurtin et al[12].
The utility of the normal-energy distribution may be seen
by recalling that $N(E_x)$ for zero temperature is given by
Eq. 2.64; $N(E_x)$ at room temperature is only slightly different
with small spreading at $E_x=FE$ and rounding at $E_x=FE-eV$.
Combining this truncated triangular shape with the graphs
of Figs. 8, 9, and 10 enables one to readily see the
exponential changes in the distribution due to changes in the
tunneling probability as $FE-E_x$ and $(FE-eV)-E_x$ are changed.
Other observations from Figs. 8, 9, and 10 are: (1) that
the sources of non-linearity of the distributions for differ-
ent voltages are apparent in the increasingly unequal heights
as the electrode spacing increases, and (2) that the thermal
smearing of about 25 mV at room temperature results in the
distributions for 1 and 10 mV being almost identical.

The other figures are reasonably self-explanatory and,
while no further discussion of them will be given here, they
will be referred to in the analysis of experimental data.
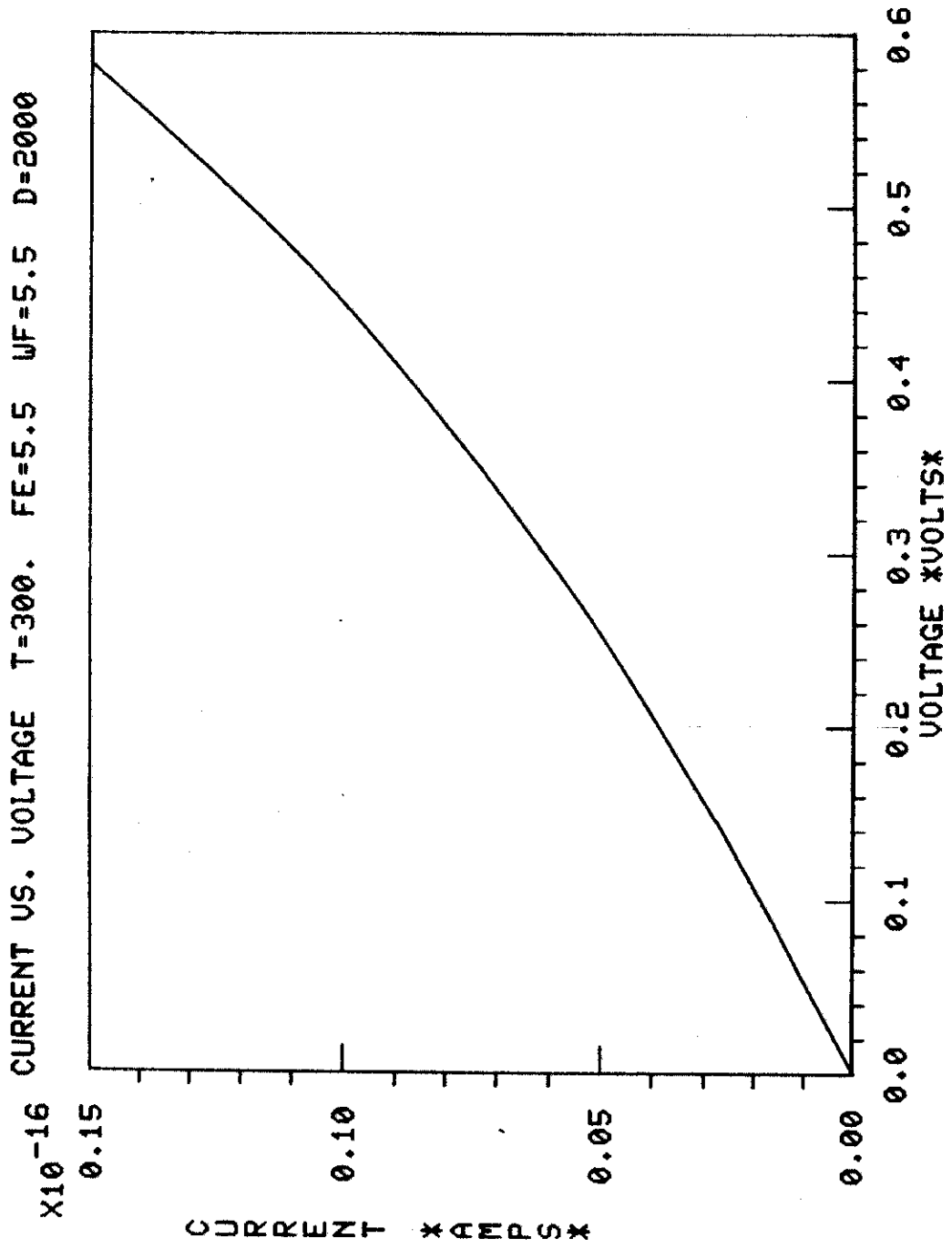
Fig. 11a.   Theoretical Current-Voltage Characteristic; FE and WF are in eV; D is in pm.
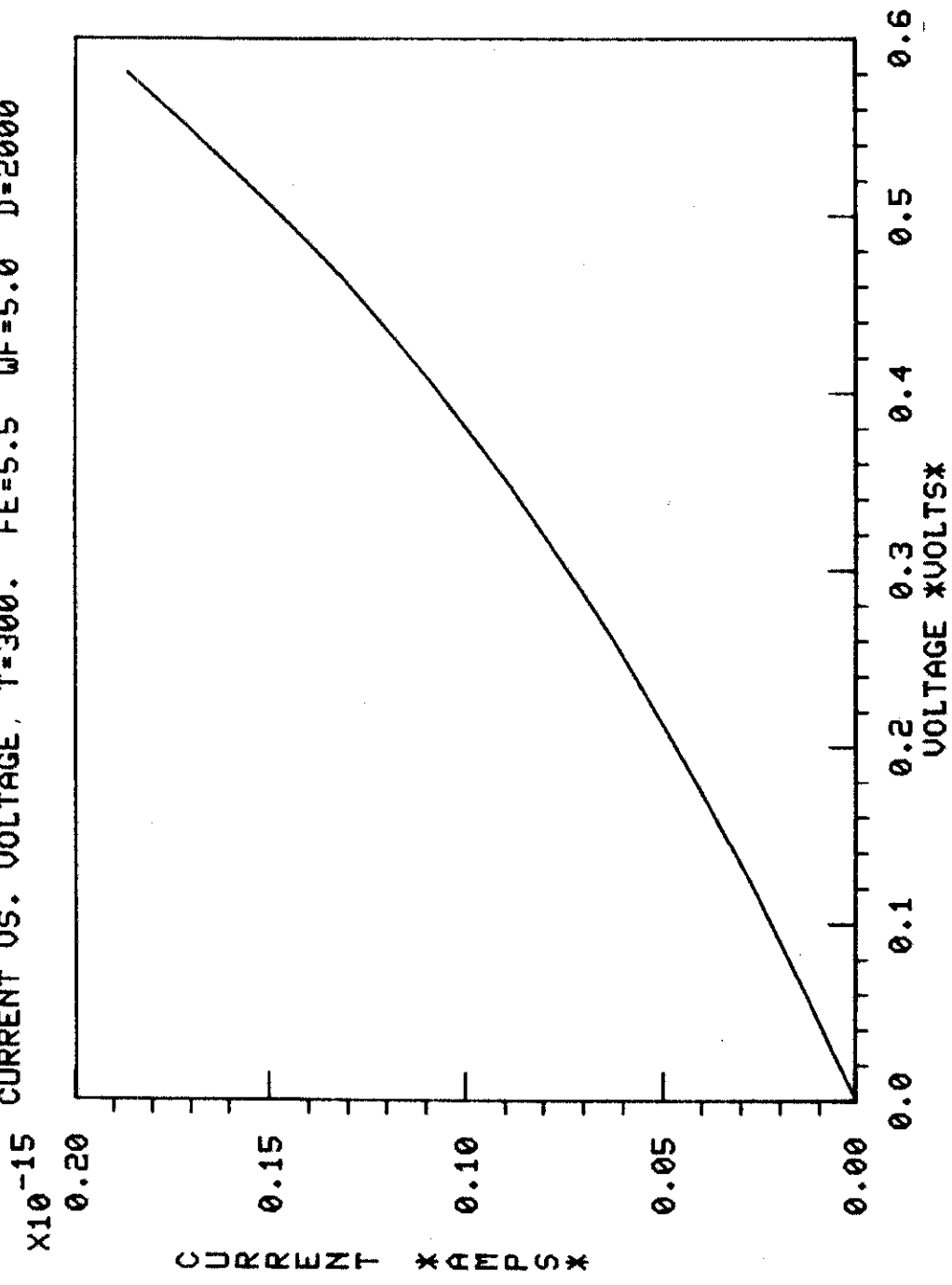
Fig. 11b. Theoretical Current-Voltage Characteristic; FE and WF are in eV; D is in pm. Graph is a repeat of Fig. 11a with WF of 5.0 eV.

CURRENT VS. VOLTAGE   T=300.   FE=5.5   WF=4.5   D=2000

X10⁻¹⁴

CURRENT *AMPS*

VOLTAGE *VOLTS*
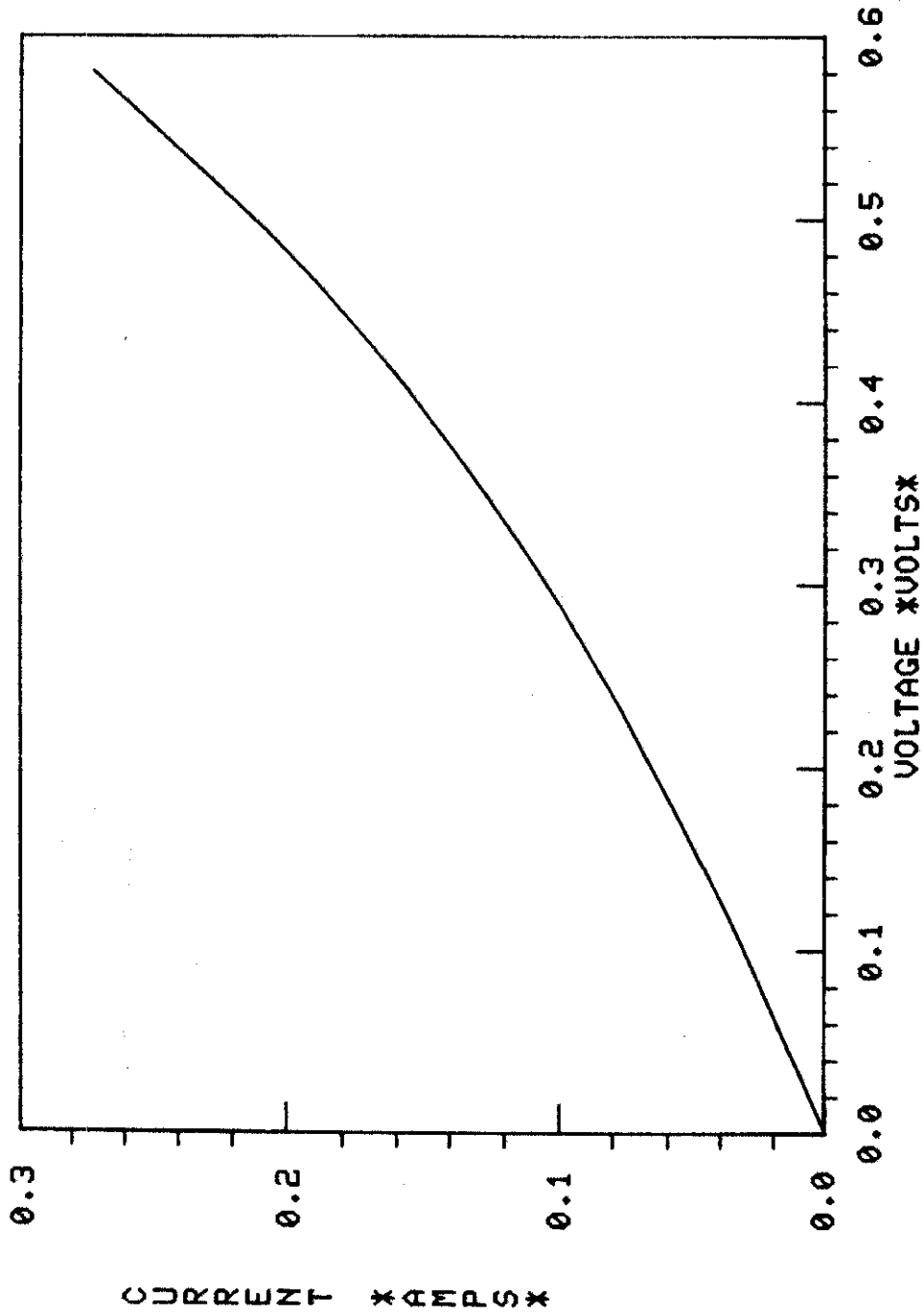
Fig. 11c. Theoretical Current-Voltage Characteristic; FE and WF are in eV;
D is in pm. Graph is a repeat of Fig. 11a with WF of 4.5 eV.

CURRENT VS. VOLTAGE   T=300.   FE=5.5   WF=4.0   D=2000

VOLTAGE *VOLTS*

CURRENT *AMPS*

x10⁻¹³
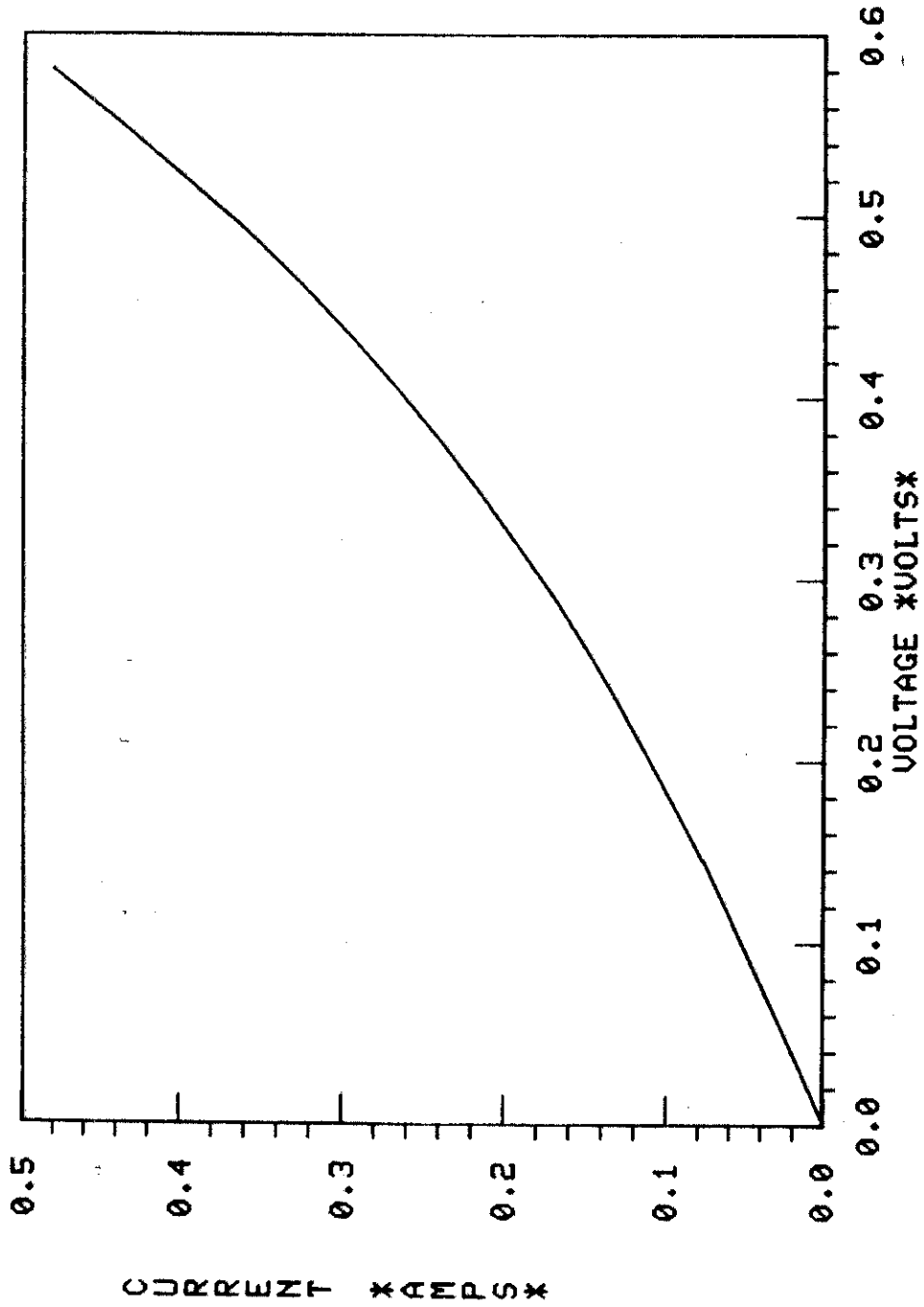
Fig. 11d. Theoretical Current-Voltage Characteristic; FE and WF are in eV;
D is in pm. Graph is a repeat of Fig. 11a with WF of 4.0 eV.
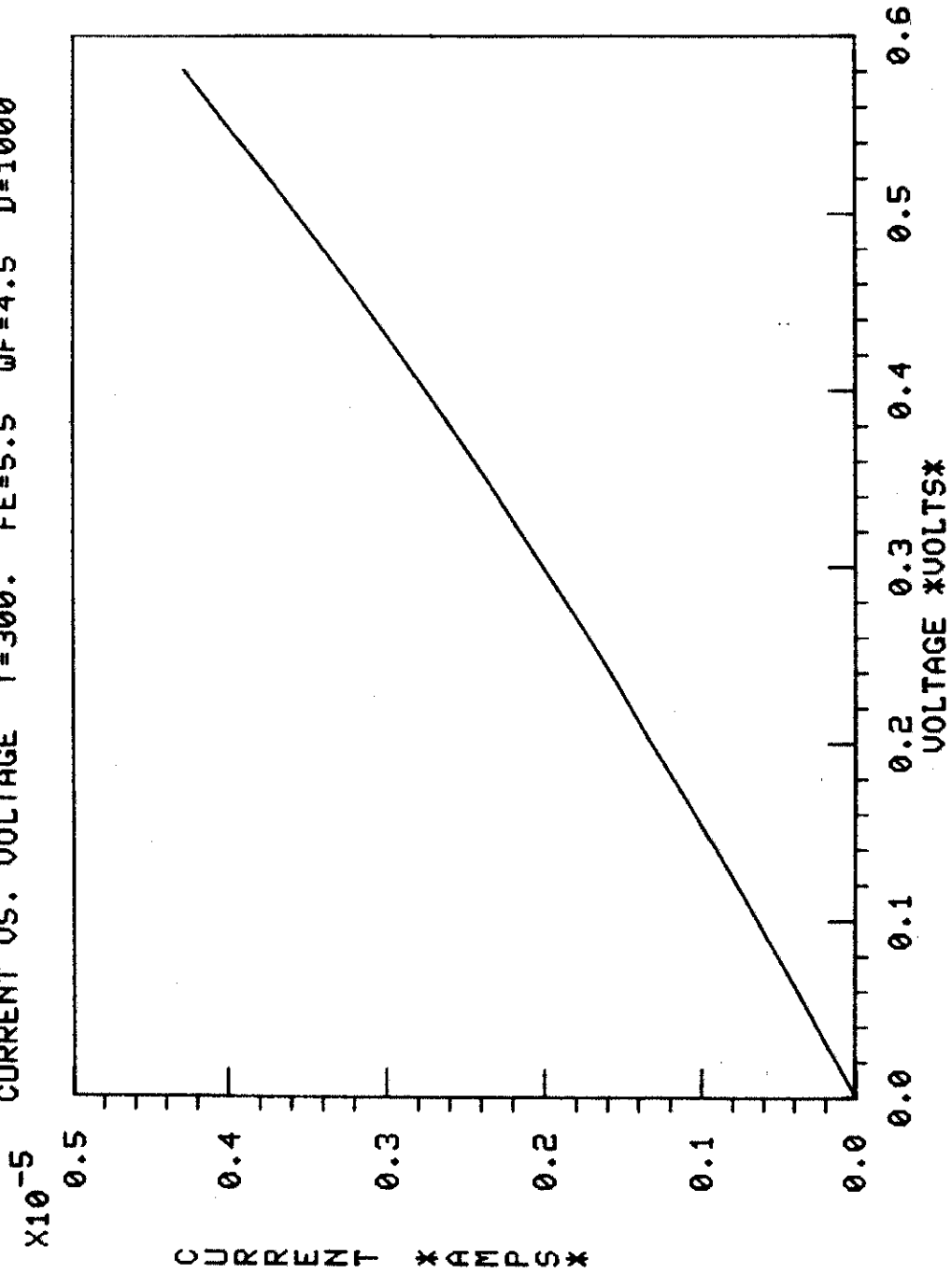
Fig. 12a. Theoretical Current-Voltage Characteristic; FE and WF are in eV;
D is in pm. Figures 12b, 12c, and 12d are repeats of this characteristic with
different electrode spacings.

64
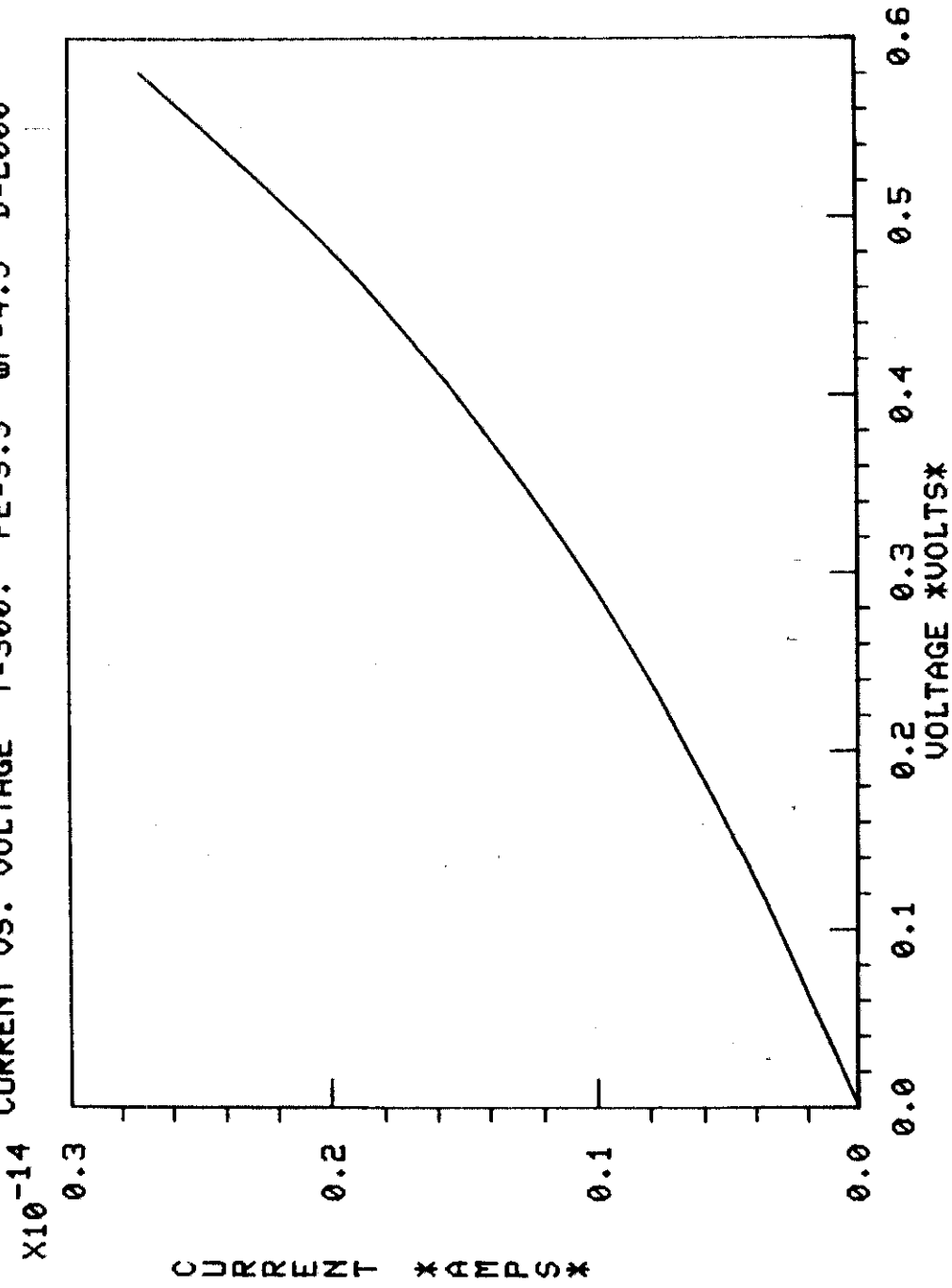
Fig. 12b. Theoretical Current-Voltage Characteristic. Repeat of Fig. 12a with an electrode spacing of 2000 pm.

CURRENT VS. VOLTAGE   T=300.   FE=5.5   WF=4.5   D=2500

$X10^{-19}$
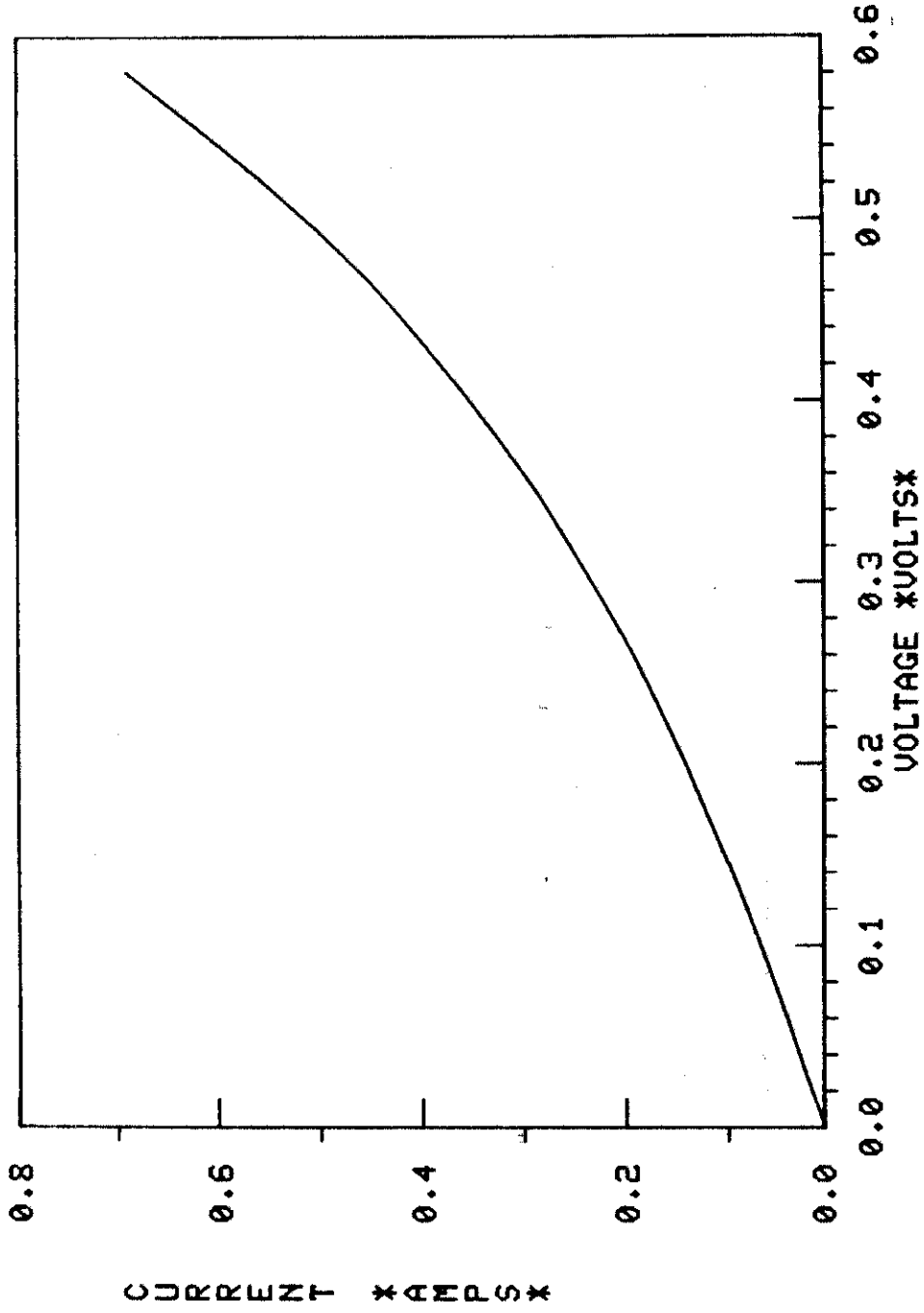
Fig. 12c. Theoretical Current-Voltage Characteristic. Repeat of Fig. 12a with an electrode spacing of 2500 pm.
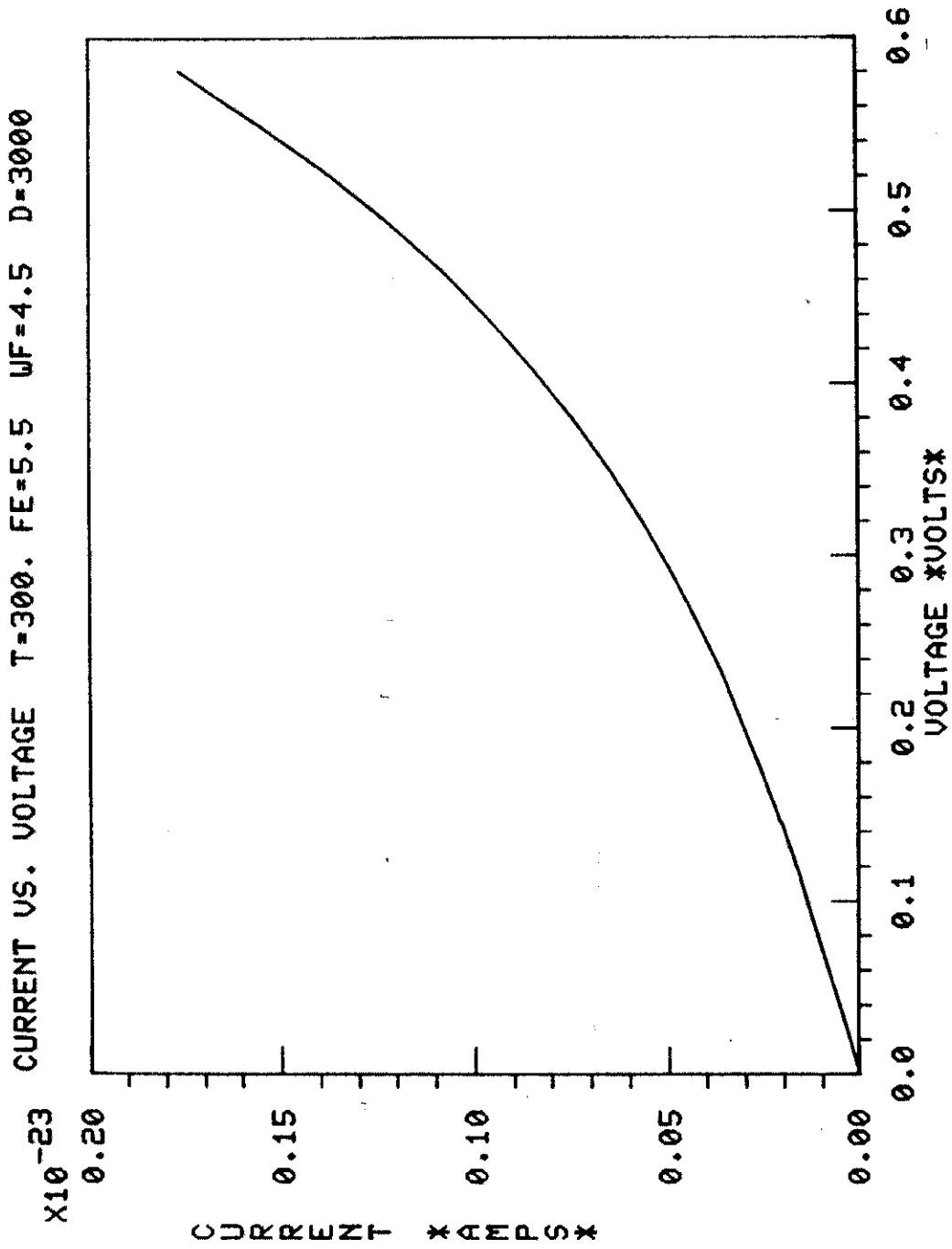
Fig. 12d. Theoretical Current-Voltage Characteristic. Repeat of Fig. 12a with an electrode spacing of 3000 pm.

Fig. 13. Theoretical Log Current-Spacing Characteristic for Four Work Functions ; Bias Voltage of 0.01 Volts. Work functions are in eV.

CURRENT VS. DISTANCE   T=300.   FE=5.5   V=.100
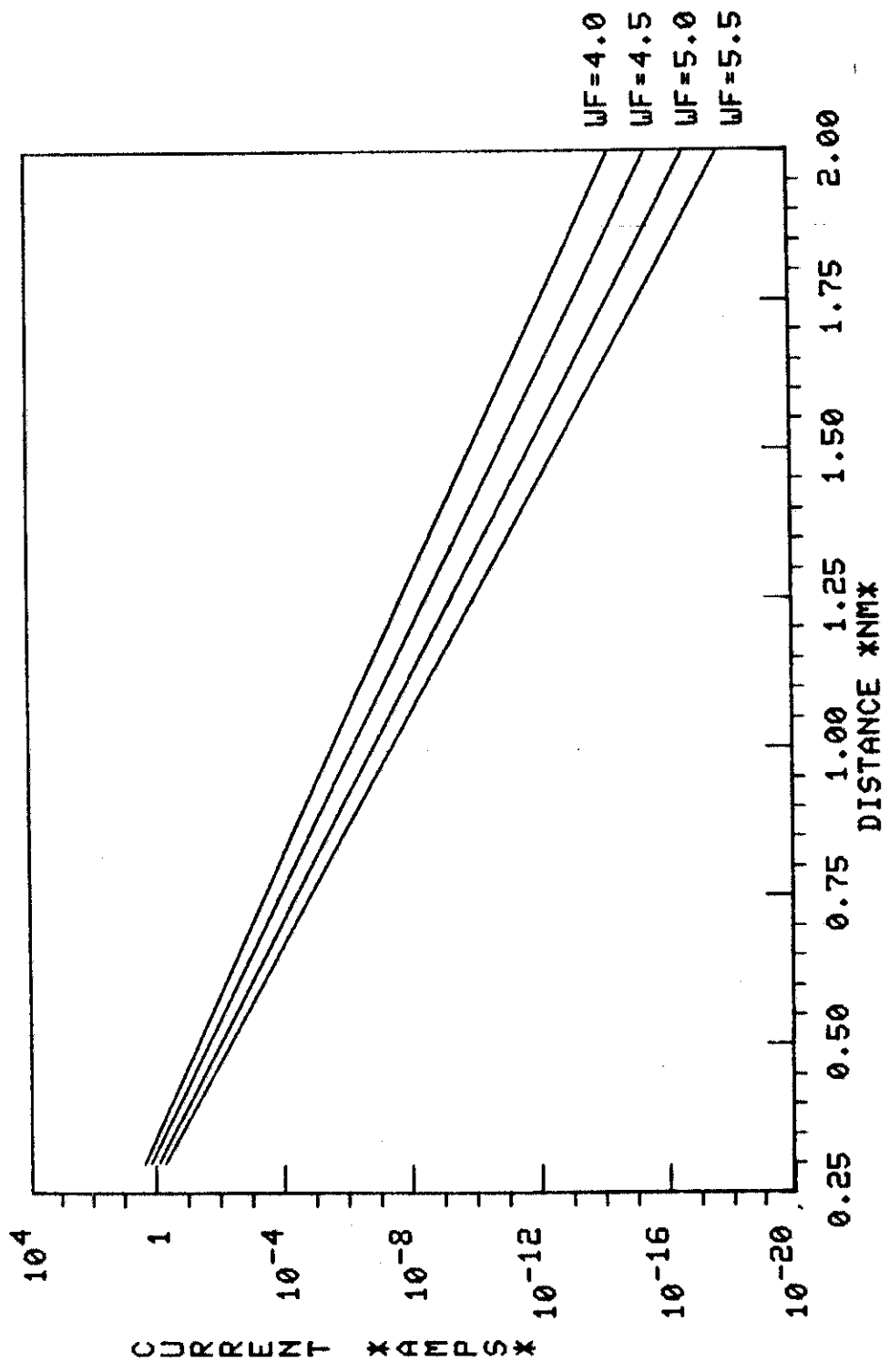
Fig. 14.   Theoretical Log Current-Spacing Characteristic for Four Work Func-
tions; Bias Voltage of 0.10 Volts. Work functions are in eV.
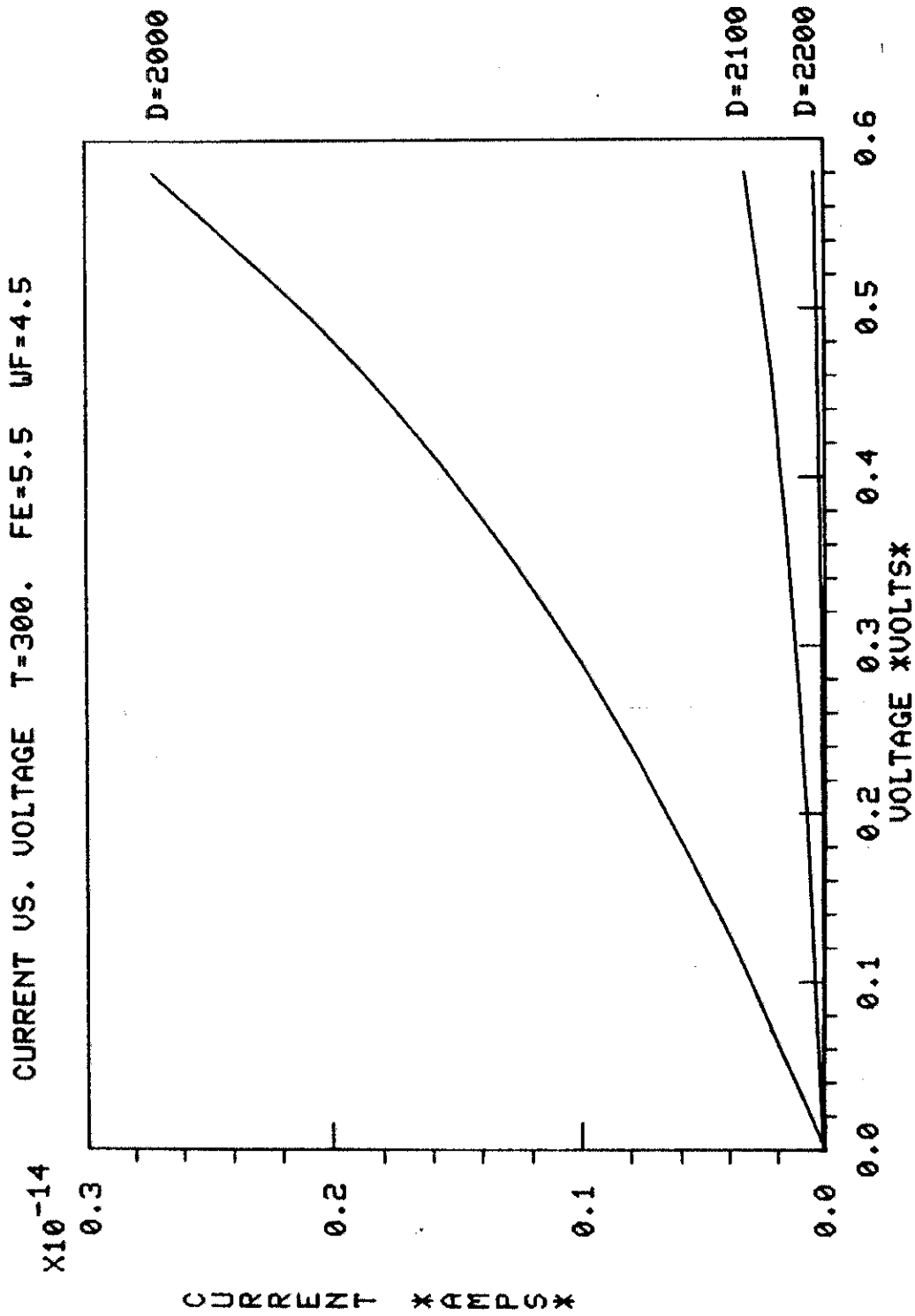
Fig. 15. Theoretical Current-Voltage Characteristic; Work Function of 4.5 eV, Electrode Spacings of 2.0, 2.1, and 2.2 nm.

CURRENT DENSITY VS. DISTANCE   T=300.   FE=5.5   V=.1

WF=4.0
WF=4.5
WF=5.0
WF=5.5

DISTANCE *NM*
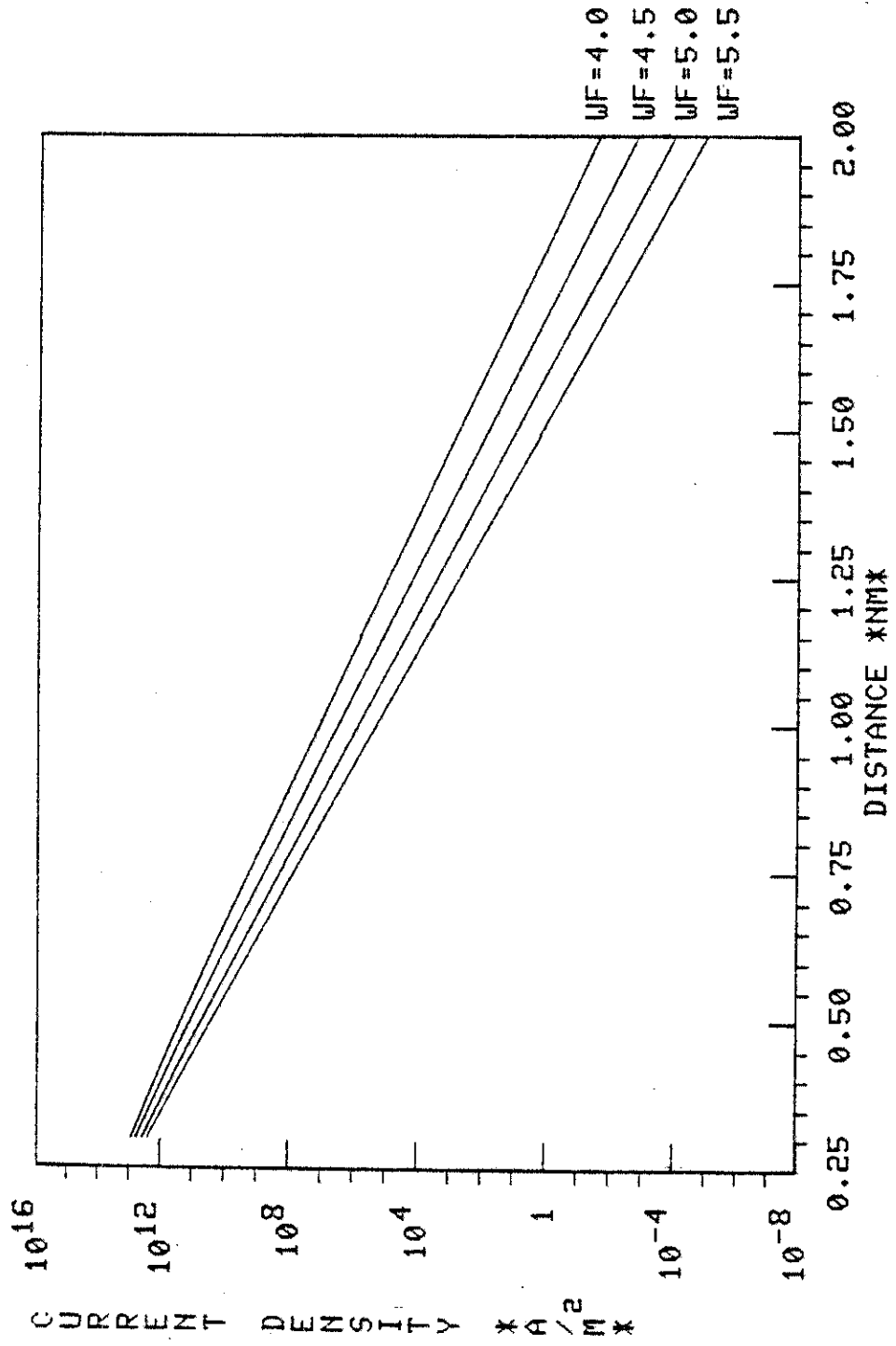
Fig. 16.   Theoretical Log Current Density-Spacing Characteristic; Work Functions of 4.0, 4.5, 5.0, and 5.5 eV.
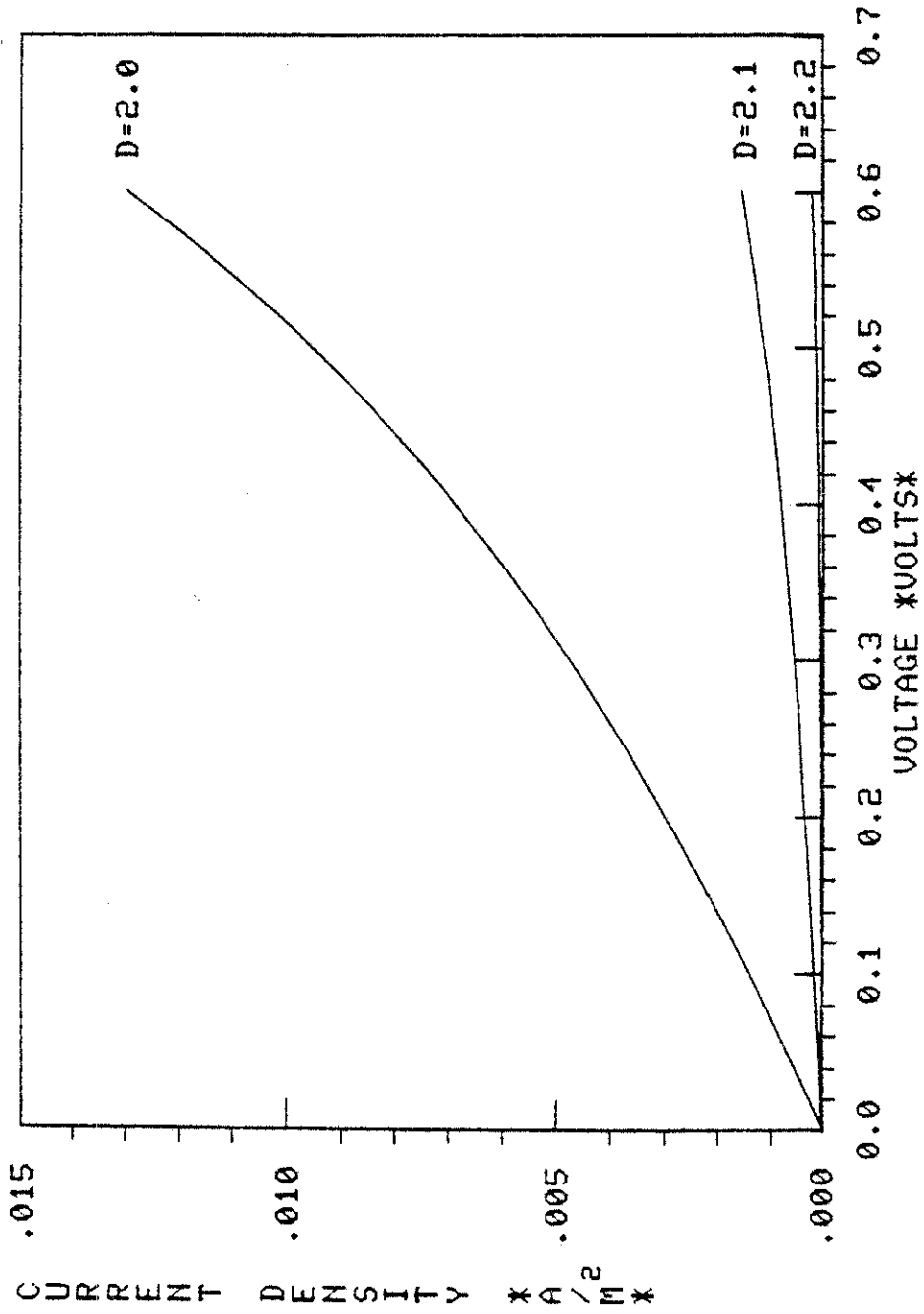
Fig. 17. Theoretical Current Density-Voltage Characteristic; Work Function of 4.5 eV, Electrode Spacings of 2.0, 2.1, and 2.2 nm.

TABLE 2

TUNNELING BETWEEN IDENTICAL ELECTRODES

CURRENT DENSITY VERSUS ELECTRODE SPACING AND VOLTAGE

(CURRENT DENSITY IN UNITS OF AMPS/MXM)

TEMPERATURE = 300 DEGREES KELVIN
WORK FUNCTION = 5.0 ELECTRON VOLTS
FERMI ENERGY = 5.5 ELECTRON VOLTS

VOLTAGE (VOLTS)

ELECTRODE SPACING (NM)	.05	.10	.15	.20	.25	.30	.35	.40	.45	.50	.55	.60
.3	.212+13	.424+13	.636+13	.849+13	.106+14	.128+14	.149+14	.171+14	.192+14	.214+14	.236+14	.258+14
.4	.257+12	.515+12	.773+12	.103+13	.129+13	.155+13	.182+13	.208+13	.235+13	.262+13	.289+13	.317+13
.5	.283+11	.567+11	.852+11	.114+12	.143+12	.172+12	.201+12	.231+12	.260+12	.291+12	.321+12	.353+12
.6	.304+10	.609+10	.916+10	.122+11	.154+11	.185+11	.217+11	.249+11	.282+11	.315+11	.349+11	.383+11
.7	.324+09	.648+09	.975+09	.130+10	.164+10	.197+10	.232+10	.266+10	.302+10	.338+10	.375+10	.413+10
.8	.342+08	.685+08	.103+09	.138+09	.173+09	.209+09	.246+09	.283+09	.322+09	.361+09	.402+09	.444+09
.9	.360+07	.721+07	.109+08	.145+08	.183+08	.221+08	.260+08	.300+08	.342+08	.384+08	.428+08	.474+08
1.0	.377+06	.756+06	.114+07	.153+07	.192+07	.233+07	.274+07	.317+07	.362+07	.408+07	.456+07	.506+07
1.1	.394+05	.790+05	.119+06	.160+06	.201+06	.244+06	.288+06	.334+06	.382+06	.432+06	.484+06	.539+06
1.2	.410+04	.823+04	.124+05	.167+05	.211+05	.256+05	.303+05	.351+05	.403+05	.456+05	.513+05	.573+05
1.3	.426+03	.856+03	.129+04	.174+04	.220+04	.267+04	.317+04	.369+04	.424+04	.482+04	.544+04	.610+04
1.4	.442+02	.889+02	.134+03	.181+03	.229+03	.279+03	.332+03	.387+03	.446+03	.508+03	.576+03	.648+03
1.5	.458+01	.921+01	.139+02	.188+02	.238+02	.291+02	.347+02	.406+02	.469+02	.536+02	.609+02	.688+02
1.6	.474+00	.954+00	.144+01	.195+01	.248+01	.303+01	.362+01	.425+01	.492+01	.565+01	.644+01	.731+01
1.7	.490-01	.986-01	.149+00	.202+00	.257+00	.315+00	.378+00	.444+00	.517+00	.596+00	.682+00	.777+00
1.8	.506-02	.102-01	.155-01	.209-01	.267-01	.328-01	.394-01	.465-01	.543-01	.628-01	.721-01	.825-01
1.9	.522-03	.105-02	.160-02	.217-02	.277-02	.341-02	.411-02	.486-02	.570-02	.661-02	.763-02	.877-02
2.0	.538-04	.108-03	.165-03	.224-03	.287-03	.354-03	.428-03	.509-03	.598-03	.697-03	.808-03	.933-03
2.1	.554-05	.112-04	.170-04	.232-04	.297-04	.368-04	.446-04	.532-04	.628-04	.735-04	.856-04	.993-04
2.2	.570-06	.115-05	.175-05	.239-05	.308-05	.382-05	.465-05	.556-05	.659-05	.775-05	.906-05	.106-04
2.3	.586-07	.118-06	.181-06	.247-06	.319-06	.397-06	.484-06	.582-06	.692-06	.817-06	.960-06	.112-05
2.4	.603-08	.122-07	.186-07	.255-07	.330-07	.412-07	.504-07	.608-07	.726-07	.862-07	.102-06	.120-06
2.5	.619-09	.125-08	.192-08	.263-08	.341-08	.428-08	.525-08	.636-08	.763-08	.909-08	.108-07	.128-07
2.6	.636-10	.129-09	.198-09	.272-09	.353-09	.444-09	.547-09	.665-09	.802-09	.960-09	.115-08	.136-08
2.7	.654-11	.133-10	.204-10	.281-10	.366-10	.461-10	.570-10	.696-10	.842-10	.101-09	.122-09	.145-09
2.8	.671-12	.136-11	.210-11	.289-11	.378-11	.479-11	.594-11	.728-11	.886-11	.107-10	.129-10	.155-10
2.9	.689-13	.140-12	.216-12	.299-12	.391-12	.497-12	.619-12	.762-12	.931-12	.113-11	.137-11	.166-11
3.0	.707-14	.144-13	.222-13	.308-13	.405-13	.516-13	.646-13	.798-13	.980-13	.120-12	.146-12	.177-12

TABLE 3

TUNNELING BETWEEN IDENTICAL ELECTRODES

CURRENT DENSITY VERSUS ELECTRODE SPACING AND VOLTAGE

CALCULATED FROM SIMMONS THEORY (CORRECTED)

(CURRENT DENSITY IN UNITS OF AMPS/MXM)

TEMPERATURE = 300 DEGREES KELVIN
WORK FUNCTION = 5.0 ELECTRON VOLTS

VOLTAGE (VOLTS)

ELECTRODE SPACING (NM)	.05	.10	.15	.20	.25	.30	.35	.40	.45	.50
.3	.704+12	.142+13	.216+13	.292+13	.371+13	.452+13	.538+13	.627+13	.721+13	.821+13
.4	.191+12	.204+12	.308+12	.413+12	.520+12	.628+12	.738+12	.849+12	.962+12	.108+13
.5	.182+11	.367+11	.556+11	.749+11	.946+11	.115+12	.135+12	.156+12	.178+12	.200+12
.6	.236+10	.478+10	.725+10	.978+10	.124+11	.150+11	.178+11	.206+11	.235+11	.265+11
.7	.279+09	.564+09	.856+09	.116+10	.146+10	.178+10	.211+10	.245+10	.280+10	.316+10
.8	.314+08	.636+08	.966+08	.131+09	.166+09	.202+09	.239+09	.278+09	.319+09	.361+09
.9	.345+07	.698+07	.106+08	.144+08	.183+08	.223+08	.265+08	.308+08	.354+08	.401+08
1.0	.372+06	.755+06	.115+07	.156+07	.198+07	.242+07	.288+07	.336+07	.386+07	.439+07
1.1	.398+05	.807+05	.123+06	.167+06	.212+06	.260+06	.310+06	.362+06	.417+06	.476+06
1.2	.421+04	.855+04	.130+05	.177+05	.226+05	.277+05	.331+05	.387+05	.447+05	.511+05
1.3	.444+03	.901+03	.138+04	.187+04	.239+04	.293+04	.351+04	.412+04	.477+04	.547+04
1.4	.465+02	.946+02	.144+03	.197+03	.251+03	.309+03	.371+03	.437+03	.507+03	.583+03
1.5	.486+01	.988+01	.151+02	.206+02	.264+02	.325+02	.391+02	.461+02	.537+02	.619+02
1.6	.506+00	.103+01	.158+01	.215+01	.276+01	.341+01	.411+01	.486+01	.568+01	.656+01
1.7	.526-01	.107+00	.164+00	.224+00	.288+00	.357+00	.431+00	.511+00	.599+00	.695+00
1.8	.545-02	.111-01	.170-01	.233-01	.300-01	.373-01	.451-01	.537-01	.631-01	.735-01
1.9	.565-03	.115-02	.177-02	.242-02	.313-02	.389-02	.472-02	.563-02	.664-02	.776-02
2.0	.584-04	.119-03	.183-03	.251-03	.325-03	.405-03	.493-03	.590-03	.698-03	.819-03
2.1	.603-05	.123-04	.189-04	.260-04	.337-04	.422-04	.515-04	.618-04	.734-04	.865-04
2.2	.621-06	.127-05	.196-05	.270-05	.350-05	.439-05	.537-05	.647-05	.771-05	.912-05
2.3	.640-07	.131-06	.202-06	.279-06	.363-06	.456-06	.560-06	.677-06	.810-06	.962-06
2.4	.659-08	.135-07	.208-07	.288-07	.376-07	.474-07	.584-07	.708-07	.851-07	.101-06
2.5	.678-09	.139-08	.215-08	.298-08	.389-08	.492-08	.608-08	.741-08	.894-08	.107-07
2.6	.697-10	.143-09	.221-09	.307-09	.403-09	.511-09	.634-09	.775-09	.939-09	.113-08
2.7	.716-11	.147-10	.228-10	.317-10	.417-10	.530-10	.660-10	.810-10	.986-10	.119-09
2.8	.735-12	.151-11	.235-11	.327-11	.431-11	.550-11	.687-11	.847-11	.104-10	.126-10
2.9	.755-13	.155-12	.242-12	.338-12	.446-12	.571-12	.716-12	.886-12	.109-11	.133-11
3.0	.774-14	.159-13	.249-13	.348-13	.461-13	.592-13	.746-13	.927-13	.114-12	.140-12

The computer programs used to obtain the data described in items 1 through 4 are given in Appendix I, along with annotations which explain the major mathematical difficulties encountered while bringing the programs up to a correctly operating state. There are, however, several additional points about the physics involved which should be described here. To calculate all the constants involved, the following values of the fundamental constants were used:

m = mass of the electron = 9.11×10^{-31} kg

e = charge on the electron = 1.60×10^{-19} C

k_B = Boltzmann's constant = 1.38×10^{-23} J/K = 86.2 μeV/K*

h = Planck's constant = 6.625×10^{-34} J s.

With these values,

$$N(E_x) = 1.3585 \times 10^{10} \, T \, \ln \, [\quad] \, A/eV \, K \, m^2. \qquad (2.78)$$

The value of $a = 10.25(eV)^{-1/2}(nm)^{-1}$ and $1.15e^2 \ln 2/(8pi\epsilon_o) = 0.2867(eV \, nm)$ were also obtained with these values for the fundamental constants.

Due to the nature of $N(E_x)$, which was explained earlier, Eq. 2.61a was decomposed into three parts:

$$J_1 = A_T k_B T [(eV/k_B T) \int_0^{FE-c-eV} D(E_x) dE_x], \qquad (2.79a)$$

---

* Here and in Chapters III and IV, μ denotes "micro".

$$J_2 = A_T k_B T \int_{FE-c-V}^{FE+WF-ETOP} \ln(FDI/FDII) dE_x, \qquad (2.79b)$$

$$J_3 = A_T k_B T \int_{FE+WF-ETOP}^{FE+80k_B T} \ln(FDI/FDII) dE_x, \qquad (2.79c)$$

with $J=J_1+J_2+J_3$. c was chosen as $40k_B T$ and ETOP is the top of the barrier potential function. Neglecting small changes in the maximum barrier height with applied bias voltages, ETOP is given by

$$ETOP = [0.575\ e^2 \ln 2/(8pi\ \not{e}_o)]S^{-1} \qquad (2.80)$$

J_3 was not included in the calculations unless ETOP was less The form for $D(E_x)$ used in the calculations was

$$D(E_x) = (1+\exp[2 \int_{x_L}^{x_R} K(x) dx])^{-1}, \qquad (2.81)$$

$K(x)$ is as defined in Eq. 2.61e. This form may be approximately obtained from Eq. 2.61e by factoring $4\theta^2$ from the second term and performing a series expansion. The result is $D(E_x) = (1/2+\theta^2)^{-1}$. Eq. 2.81 has been obtained by Miller and Good[41] by analytic continuation and was shown to hold for all energies, including energies greater than the barrier height; one determines complex turning points in this instance. The Miller and Good form of the WKB transmission

enabled the calculations to proceed smoothly up to the top of the barrier, where $x_L = x_R$ and $D(E_x) = 0.5$. The value for the exact transmission coefficient of a particle with energy at the top of a rectangular shaped barrier is 0.2. Since, one would expect the image potential rounded barrier to be less reflective, the 0.5 value is at least intuitively correct. To avoid the complexities of determining complex turning points, a simple linear interpolation between 0.5 and 1 was used from ETOP to the vacuum level.

Current Calculations For Sperical Electrodes

Current flow was obtained from the current density calculations by assuming that in the almost planar electrode structure, the current flow was parallel to the axis of the two spheres. The incremental tunneling areas are then rings around this axis of radius r with spacing greater than the closest spacing between the electrodes. The current flow in this approximation is

$$I = \int_{x_o}^{x_m} J(x)\,dA, \qquad (2.82)$$

$J(x)$ is the current density for an electrode spacing x, x_o is the on-axis electrode spacing and x_m is the spacing between points off-axis at which $J(x)$ has dropped to a negligible value. For R much smaller than the sphere madius R:

$$r(x) = [R(x-x_o)]^{1/2}. \qquad (2.83)$$

With dA=2 pi r dr, Eq. 2.82 is therefore:

$$I = piR \int_{x_o}^{x_m} J(x) \, dx. \qquad (2.84)$$

The 10^{-12} factor employed in the programs in Appendix I results from the use of x in nm and R in mm.

CHAPTER III

EXPERIMENTAL APPARATUS AND METHOD

The rule-of-thumb expression for the tunneling current, I, at small voltage, V

$$I = C \exp(-a\ S\ B^{1/2})\ A\ V, \qquad (3-1)$$

and its ramifications were the major factors which determined all aspects of the apparatus design, construction, and use. As shown in Chapter II, C is approximately a constant, A is the device tunneling area, a is 10.25 $(eV)^{-1/2}$ $(nm)^{-1}$, S is the electrode spacing, and B is the mean barrier height. Some insight into the experimental problems which had to be addressed may be obtained by observing that according to Eq. 3-1 a change in electrode spacing of 0.1 nm, about one-half an atom diameter, will generate a factor of ten change in the tunneling current. This statement assumes that the barrier height is 5 eV. In a metal-vacuum-metal tunneling device, an electrode spacing stability of one pm is therefore required to achieve a noise level of two percent or less in the tunneling current for a fixed voltage. This corresponds to a signal-to-noise ratio of only 34dB.

Mechanical and Thermal Requirements

The electrode spacing stability is in turn determined by the mechanical and thermal properties of the electrodes and the assembly into which they are placed. As representative values, let the effective length, L, for thermally generated changes in electrode spacing be 5 nm and the expansion coefficient, k_T, of the materials involved be 10 ppm/K. Then, the required temperature stability, dT, to achieve a one pm stability, dL, in electrode spacing is

$$dT = dL(L \; k_T)^{-1} = 20 \; \mu K \qquad (3-2)$$

The laboratory in which the experiment was to be performed had a temperature stability of $\pm$ 0.5 K over a 24 hour period. However, when local sources of heat such as that of the body heat of the experimenter are taken into account, the local variations in environmental temperature are more represented by $\pm$ 1 K. An approximate attenuation to 10^{-5} of the environmental temperature variations must, therefore, be provided by a temperature control system.

Requirements for mechanical stability were determined by measuring the amplitude and frequency composition of building vibrations at the planned laboratory location of the experimental apparatus. The transducer used for these measurements was a Texas Instruments S-36 very low frequency seismic detector whose sensitivity was 1.97 V/cm/s. The

transducer's response was approximately ten percent greater

at its resonance frequency of 2 Hz and dropped by about

fifteen percent at one Hz. Fig. 18 shows the velocity ampli-

tude spectrum of the building vibrations in the National Bur-

eau of Standards Reverberation Chamber. Measurements were per-

formed here because it was one of the quietest possible loca-

tions for conducting the vacuum tunneling experiment and, in

addition, it was the only laboratory which allowed convenient

access to the Fourier transform electronics necessary for

obtaining real-time vibration spectra. Vibration spectra from

this location were compared with other possible locations for

the experiment with the use of oscillographs. These oscillo-

graphs showed that the vibrations present on a vibration table

with a resonant frequency of one Hz and located in a basement

laboratory were similar in amplitude and frequency content

to those measured in the well isolated NBS Reverberation Cham-

ber. The NBS Reverberation Chamber is a room-within-a-room

structure with an inside room volume of about 400 m^3. The

inner room is supported on springs to produce a room-spring

resonance frequency of 3.5 Hz.

Depending on the frequency, the vibration amplitudes

which must be accounted for, even with a vibration isolation

table, are therefore between 40 and 200 nm; the 40 nm

amplitude corresponding to frequencies of about 30 Hz.

Fig. 18 only shows the vertical component of vibration

displacements; measured horizontal components were similar
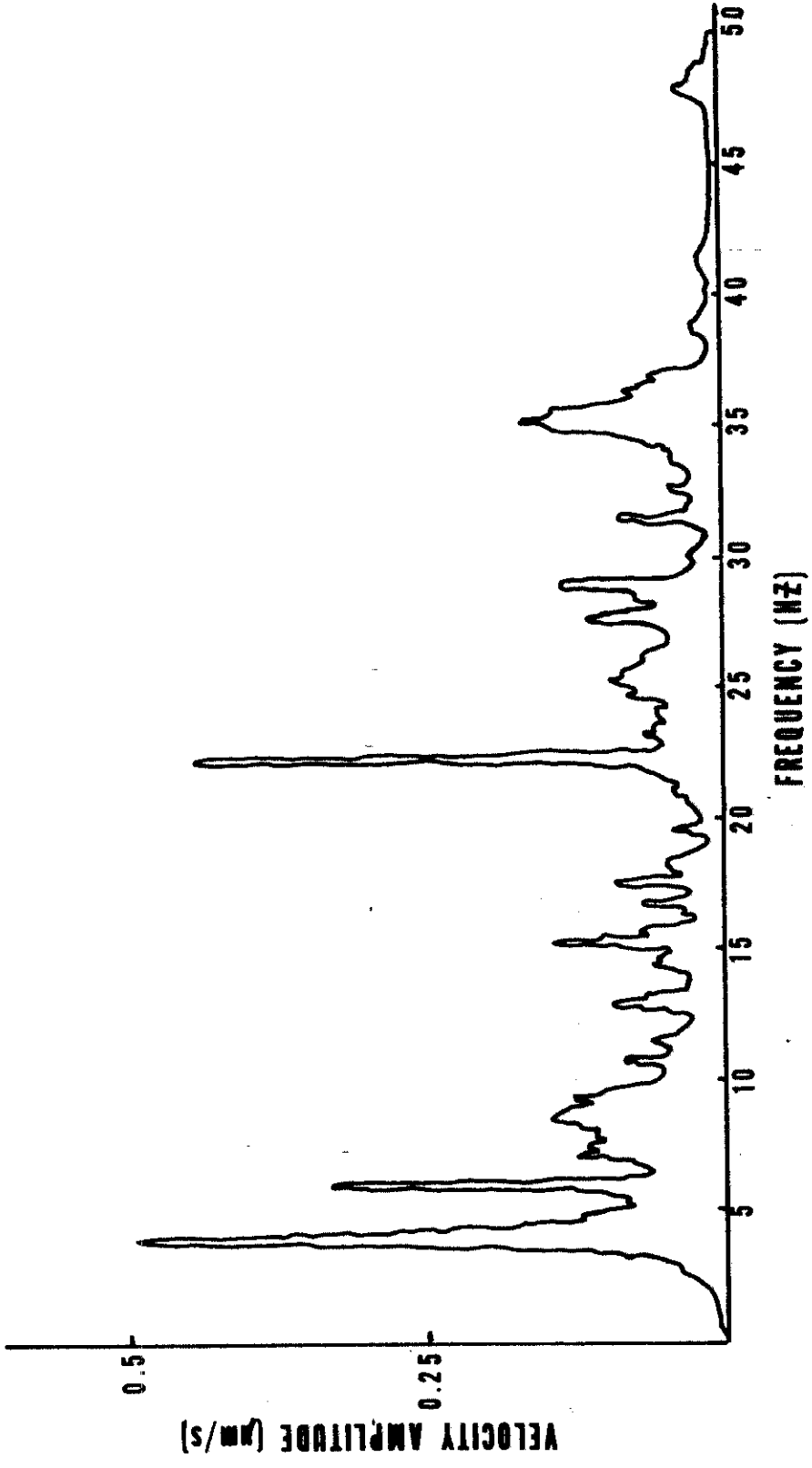
Fig. 18. Measured Velocity Amplitude Spectrum of Building Vibrations in the National Bureau of Stamdards Reverberation Chamber.

in amplitude, but with major contributions existing only at frequencies near 35 Hz and below 10 Hz. The mechanical design of the electrode holder must, therefore, attenuate these vibrations by about 10^{-4} to 10^{-5} to produce the one pm stability.

A second factor which must be accounted for in designing for mechanical stability is acoustical pressure variations in the air around the experimental apparatus. No measurements of the magnitude and frequency content of the acoustical pressure variations were made since reliable estimates could be obtained from the literature. Hunter[42] gives a graph of the noise amplitude as a function of frequency for an average room. For a mean noise level of 40 dB referenced to 2×10^{-5} N/m^2, the amplitude at 20 Hz was 40 dB and dropped almost linearly to -5 dB at 5000 Hz. Within the laboratory used for this experiment, there were no distinctive noise sources, so this description of the acoustical environment was taken as representative.

Choosing an Electrode Material and
Preparing the Electrodes

Variations in the mean barrier height also produce large changes in the tunneling current. For small changes in B, dB, Eq. III-1 may be used to obtain

$$dI/I = -1/2 \ a \ S \ B^{-1/2} \ dB. \qquad (3-3)$$

With S = 1 nm, B = 4 eV, and dB = 0.1 eV, dI/I = -0.26. To achieve the 34 dB signal to noise ratio for this noise

component with S = 1 nm and B = 4 eV requires that B be stable to 0.008 eV.

Changes in work function and thus barrier height are produced by the adsorption and chemisorption of any kind of foreign atom on a metal surface [16, 21]. The change in the work function, WF is a local microscopic effect, but in terms of a spatially averaged change, it can formally be related to an effective dipole moment p per adsorbed particle via the equation[21, 43]

$$WFC = 4 p N, \qquad (3-4)$$

where N is the number of adsorbed atoms or molecules per unit area, and WFC represents a change in the WF. Adsorption is viewed as changing the $[V(+\infty)-V(-\infty)]$ term of the WF described in Chapter II. Changes in WF range from +0.08 eV for a 1/4 monolayer of selenium on nickel to -3.1 eV for a monolayer of cesium on tungsten (100)[21, 43]. Larger increases in the WF are also found, but usually no greater than 1 eV. WFC's due to more common adsorbates such as oxygen, nitrogen, and hydrogen are typically about 1 eV, and may be of either sign depending on the substrate-adsorbate combination.

This demand for stable clean electrode surfaces must be carefully balanced with the opposing need for high temperature stability. There are two major reasons for the conflict between these two requirements. First, to achieve

atomically clean metal surfaces, such that the work function would not be changed by any contaminants, some form of in-situ vacuum cleaning process must be employed. The most common and reliable methods for in-situ cleaning all require large energy inputs either to simply evaporate or decompose all surface and near surface contaminants, e.g. high temperature flashing of W or high temperature cycling in oxidizing and reducing atmospheres e.g., Ni in O_2 and H_2. Second the time for a contaminating layer to form on a clean surface is comparable with estimated times for an electrode assembly to thermally equilibrate to the stabilities demanded by the vacuum tunneling experiment.

The time, T, in which an initially clean surface will become covered with a monolayer of adsorbate when the surface is exposed to a gas at pressure P Torr is (see Appendix III)

$$T \doteq 2 \times 10^6/P \text{ seconds.} \tag{3.5}$$

Eq. III-5 is only a rough estimate, but is useful in determining the vacuum conditions necessary for this particular application. A minimum time in a system that had been raised to 1300 K to obtain a 10 ujK stability would be about 24 hours or 8.6×10^5 seconds. To maintain a clean surface over this period of time would require the partial pressures of all possible adsorbates be much less than 10^{-12} Torr, since according to Eq. 3.5 one monolayer

would accumulate at a pressure of 2×10^{-12} Torr. Vacuum pressures at this level are at the limits of modern technology and are achieved with only cryopumping or by very careful use of vacuum materials.

As a compromise between the demands of temperature stability and the requirement for clean surfaces, gold was chosen as the electrode material because none of the common adsorbates, including molecular oxygen have been found to chemisorb at room temperature and it could be conveniently formed into electrodes with clean, smooth surfaces prior to installation into the temperature control and micropositioning assembly.

The approach taken was to fabricate the gold electrodes in one UHV system, to store and transport the fabricated electrodes in dessicated containers, and finally to assembly the electrodes into an electrode assembly in the laboratory atmosphere. As discussed in the next paragraph, this procedure certainly does not result in an ideally clean surface. However, after the electrodes are placed in a UHV environment, the surfaces should be altered by at most a monolayer of hydrocarbon and require no further processing before the vacuum tunneling experiment could reliably be performed at a stable temperature.

The most definite study of gold's resistance to adsorbing molecular species was performed by Chesters and Somorjai[44]. They found that of the species most likely to be encountered in a laboratory environment, oxides, sulphides, hydrocarbons,

nitrides, and water vapor, the only ones which were observed

to adsorb on a gold (111) crystal face or a stepped crystal

face were heavy hydrocarbons. Their investigations were with

the crystal's temperature less than $500^{\circ}C$ and partial pres-

sures less than 10^{-6} Torr. Napthalene adsorbed on both types

of gold surfaces and the adsorption behavior indicated dis-

sociative chemisorption. Surface steps did not play a critical

role in the adsorption properties of gold, in contrast to

that of the similar chemical material, platinum. Earlier work

by Trapnell[45] using polycrystalline gold films showed that

reversible molecular adsorption of CO, C_2H_4, C_2H_2 and other

light hydrocarbons did occur with low heats of adsorption

(0.4 eV/molecule) for high pressures. These low heats of

adsorption allow the adsorption process to be reversible and

Trapnell[45] shows that at low pressures and room temperature,

the light hydrocarbons de-sorb with no measurable, i.e., less

than 2 percent, coverage at pressures less than 10^{-6} Torr.

Work function changes, WFC, in gold due to adsorption

have received very little study, in part because gold is

the most common reference electrode for measurements of the

work function[21]. In particular, no work to determine the

WFCs due to the adsorption of heavy hydrocarbons was found

in the literature. However, WFC in platinum have been studied

for a wide variety of molecular species. While the type and

behavior of molecular species which adsorb on gold surfaces

is markedly different from that on platinum surfaces, the

WFCs observed in the studies of adsorption on platinum at least set an upper bound on the WFCs to be expected for adsorption on gold. The values of the WFCs of the platinum do reflect the effective dipole moments of the adsorbed molecules on a dominantly s-electron like surface and should give a valid estimate of the dipole moment of the molecule when it is adsorbed on gold. The major difference between platinum and gold from the standpoint of chemical properties is that platinum has an unfilled 5d electronic subshell. For platinum, the WFCs were measured by Gland and Somorjai[46] for a wide range of heavy hydrocarbons. WFCs were found to be between -1.0 and -2.0 eV depending on the type of adsorbate and the degree of coverage of the platinum surface.

The gold electrodes were formed by melting the end of a 1.25 mm gold wire in UHV with electron bombardment. The apparatus used for forming the electrodes is shown and described in Fig. 19. Gold wire with 99.99 percent purity was used. Following degreasing with a trichloroethylene, acetone, ethanol sequence, the wires were etched in boiling aqua-regia, i.e., 3.5 parts HCl and 1 part HNO_3; both acids were fresh ACS grade chemicals. After rinsing the wires thoroughly in running tap water, they were ultrasonerated in de-ionized, filtered water and finally blown dry with hot air. The wires were then installed in the electron bombardment apparatus and vacuum pumping begun.

1.25 MM D. NICHROME WIRE

6 MM D. X 2 CM H.
STAINLESS STEEL
THERMAL MASS AND RESISTANCE

GOLD WIRE FOR FORMING
ONE ELECTRODE
1.25 MM D. x 5 CM LONG

0.5 MM D. TUNGSTEN
FILAMENT

1400 V.

120 VAC

10:1 STEPDOWN

CERAMIC
INSULATOR
1 CM D. X 3 CM H.

STAINLESS STEEL
SHEET FOR
SUPPORT AND FOR
ELECTROSTATIC
SHIELDING AND FIELD
SHAPING, 0.75 MM X 10CM D.

COPPER LEADS FOR
FILAMENT AND TO
SUPPORT ENTIRE
ASSEMBLY, 6 MM D.

Fig. 19. Apparatus for Forming the Gold Electrodes.

The vacuum system used for the melting operation utilized a sublimation-ion pump combination which maintained pressures of 2 to 4 x 10^{-8} Torr while the gold was molten. With the 1.4 kV indicated in Fig. 19, only about 15 mA of bombardment current was required to melt the end of the gold wires.

The stainless steel mass-thermal resistance is an essential component of the melting apparatus. This component combined with the nichrome wire provides sufficient thermal resistance to allow an equilibrium between input and dissipated power to be obtained by convenient manual adjustment of the filament heating current. Without these components, the equilibrium is difficult to obtain; the nonequilibrium result in this case is that the molten region of the wire moves up the length of the wire, forms a sphere and drops off the wire. After several of these occurences, the configuration shown in Fig. 19 was developed to avoid this problem. With this design, a molten sphere could be maintained on the end of the wire with the support of the liquid's surface tension for 10 to 20 minutes. These long periods in the molten state in vacuum provided a means to evaporate many contaminants from the surface and were sufficient for the surface tension forces to determine the microscopic surface topography.

After melting, the electrode surfaces were inspected with an optical microscope at a magnification of 300X. The

process from etching in aqua regia to melting was then repeated until no surface contamination was visible. For the pair of electrodes used in the experiment, the process was repeated four times. The resulting surfaces were very smooth with no visible topography or contaminants. The electrodes were finally examined with a scanning electron microscope (SEM) after the experiment was completed. The SEM micrographs of the electrode surfaces are shown in Figs. 20 and 21. The surfaces were sufficiently smooth that in both the electron and optical microscopes good focus was difficult to obtain.

The anticipated electrode surfaces for this experiment were, therefore, clean gold surfaces altered by at most a monolayer of adsorbed heavy hydrocarbons to produce work functions which could range from gold's work function, 5.0 eV, down to a minimum of 3.0 eV.

Temperature Control System

In order to provide the required stability of $\pm$ 1 pm for the interelectrode spacing, the design goal for the temperature control system was to produce a temperature stability of $\pm$ 20 μK. Other workers[47, 48] have shown that by careful design, temperature stabilities at this level can be achieved with the use of a two-stage control system. This approach was therefore adopted. The first and outer stage was designed to operate at a temperature of 5 K above the laboratory temperature with a stability of $\pm$ 1 mK. The
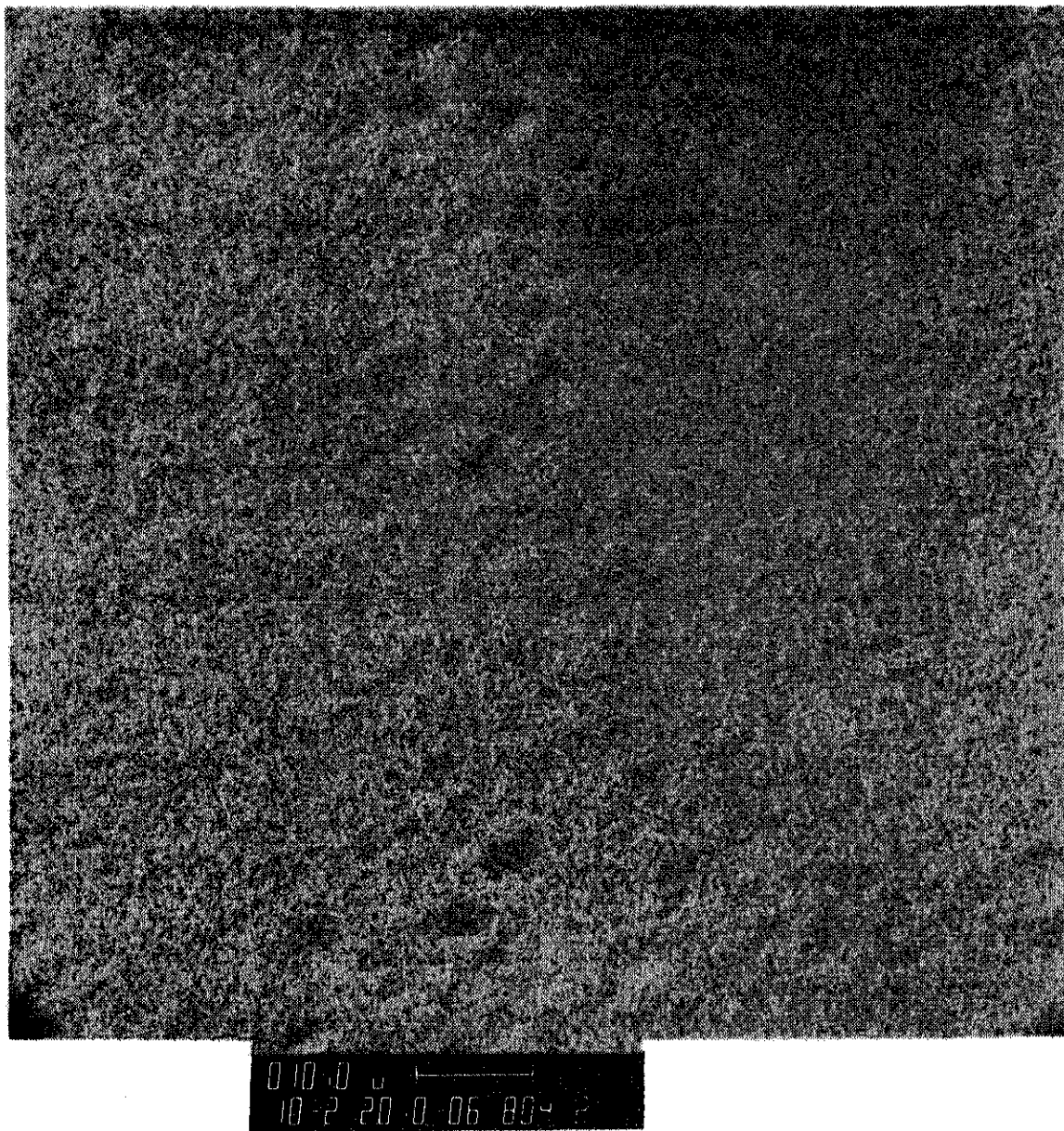
Fig. 20. Scanning-Electron-Microscope Photomicrograph of Gold Electrode Surface; View Normal to Electrode Surface.
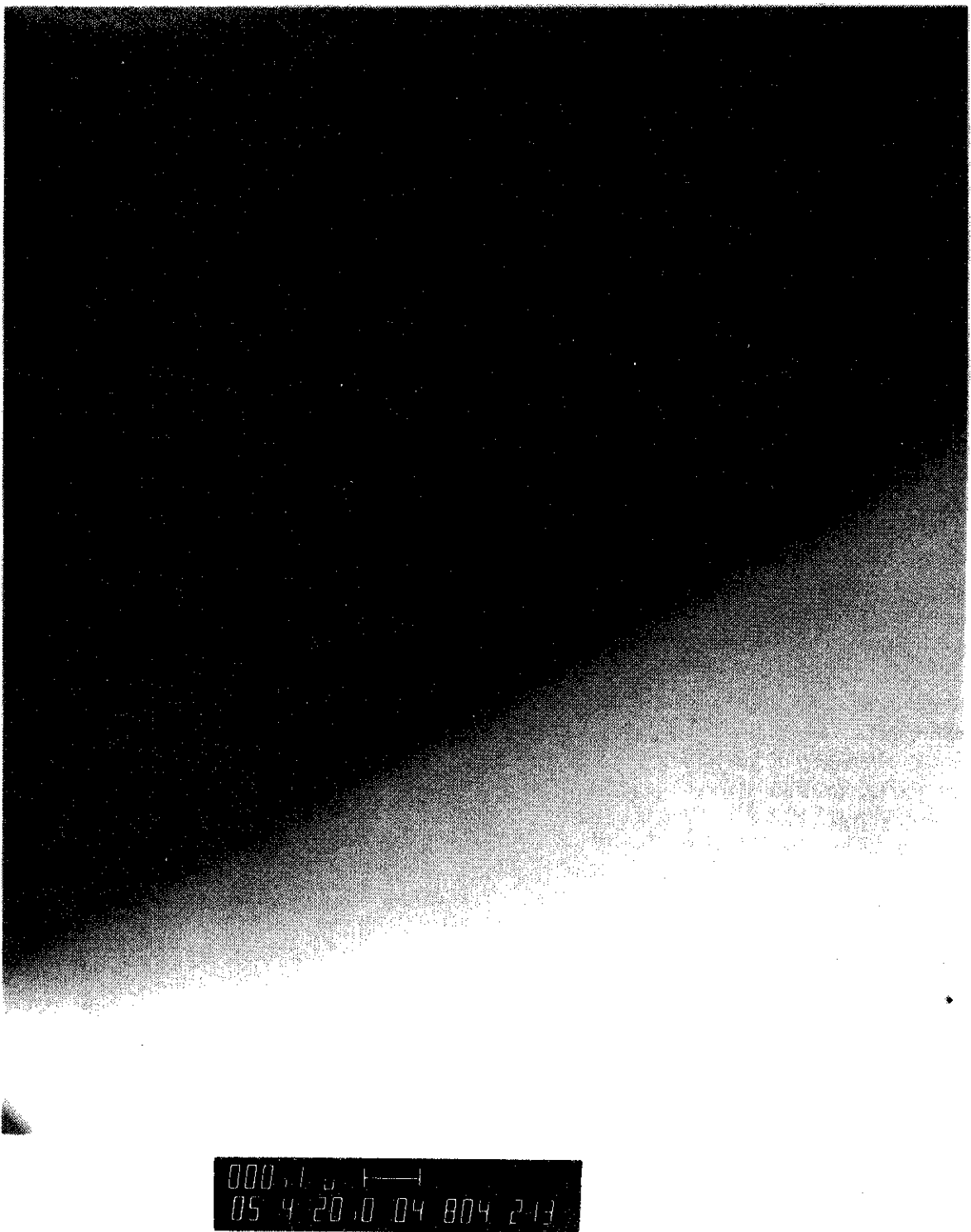
Fig. 21. Scanning-Electron-Microscope Photomicrograph of Gold Electrode Surface; Surface Projection.

second and inner stage was designed to operate at a tempera-
ture 0.5 K above the outer stage's temperature with the
specified design goal stability.

The apparatus used for the combined purposes of tempera-
ture control, vibration isolation, and acoustical isolation
is shown and described in Fig. 22. Vibration and acoustical
isolation aspects of the apparatus are described in a later
section. Several features of this apparatus should be empha-
sized. (1) Bifilar windings were used for both control heaters
to insure that stray magnetic fields in the region of the
electrode assembly would be minimal. (2) Radiation baffling
was provided at the vacuum pumping part of the inner heater
enclosure to minimize the radiant coupling between the outer
heater's fluctuations and the electrode assembly. The baffle
design insures that any radiation entering the pumping port
must be scattered at least five times from the surface of
the inner heater enclosure. (3) All joints in the polyurethane
insulation and openings for the various vacuum parts were
taped with building construction duct tape to minimize connec-
tion losses. (4) Electrical leads passing from the laboratory
through the first stage and from the first stage through the
second stage to the electrode assembly were in both cases
solidly heat-sunk to the enclosure of each respective stage.
For the outer stage, thermal contact for each electrical lead
was obtained by soldering one point of the lead to a copper
post which was mounted to the outer enclosure with the same

Fig. 22---Apparatus for Vibration Isolation, Acoustical

Isolation, and Temperature Control.

The apparatus consisted of the following components.

(1) Electrode holder and micropositioning assembly. These are

described in Fig. 25. (2) Inner stage temperature control en-

closure (6061 Aluminnum) and heater. The heater wires shown

are only schematic, actual wires were of #30 nichrome in a

bifilar configuration which almost completely covered the en-

closure's cylindrical surface. The radiation baffle is the

cross-hatched piece located immediately above the electrode

assembly. (3) Aluminum (6061 alloy) base for inner enclosure.

(4) Alumina standoffs. Three were used to provide thermal iso-

lation between the two temperature control stages. (5) Outer

stage temperature control enclosure, heater and vacuum chamber

walls. The cylinder wall thickness was 3.2 mm, top and bottom

thicknesses were 1.9 cm. Heater wires were #31 copper spaced

approximately as indicated in the drawing. An epoxy coating

approximately 3.0 mm thick with a thermal conduction coeffi-

cient of 0.01 (cal cm)/(sec cm^2 $^{\circ}$C)[49], was used to bond the

heater wires to all surfaces of the outer enclosure and to

provide acoustical damping. (6) 8 cm thick polyurethane foam.

This foam served the double function of providing thermal

and acoustical isolation of the system. enclosure and vacuum

system from vibration isolation table. (7) Epoxy standoffs,

three, were used to provide thermal insulation of outer enclo-

sure and vacuum system from the vibration isolation table.

These standoffs were bonded to the vibration isolation tabletop

and permitted rigid coupling of the entire apparatus to the

isolation table top. and (8) Granite isolation table. The

table was 61 cm x 25 cm and had an approximate mass of 409

kg. It was supported with four damped steel springs from a

simple aluminum frame. The resonant frequency of the system

was less than 1 Hz for vertical motion.
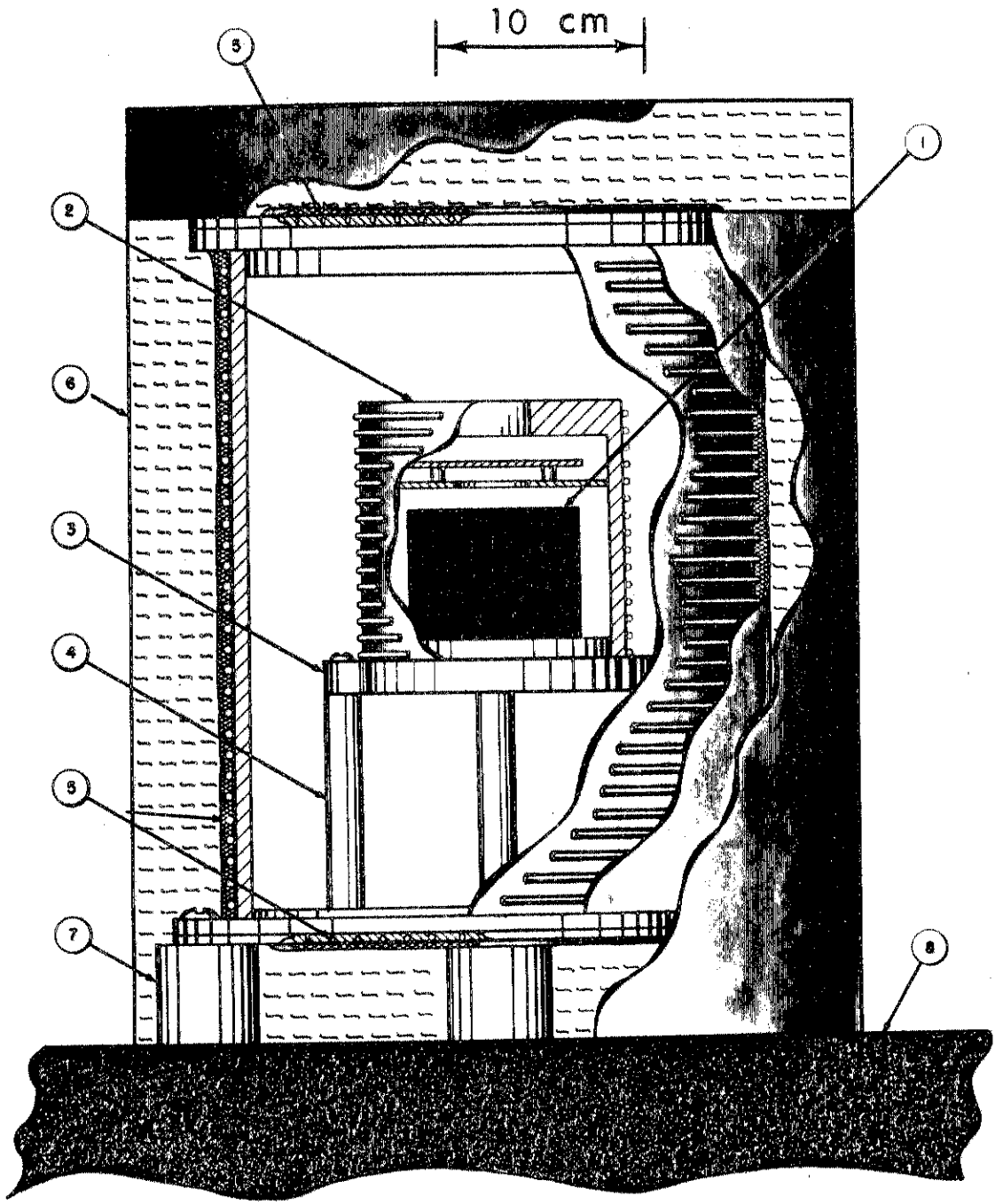
high thermal conductivity epoxy used to mount the heater
wires, see Fig. 22. Thermal contact for leads passing through
the inner stage enclosure was obtained by using copper feed-
throughs in the base of the enclosure, item 3 in Fig. 22,
which were electrically insulated with beryllium oxide wash-
ers. Total contact area for each lead was 3 cm^2.

A block diagram of the temperature control system
employed for both control stages is shown in Fig. 23. The
basic design approach of both stages was to use the output
of a bridge to drive a high gain amplifier and compensation
network to account for the lags of the detectors and stage-
masses, then to close the control loop by incorporating a
thermistor detector as one element of the bridge. A full
discussion of the electronics of both control stages is given
in Appendix V. There it is shown that one of the most impor-
tant parameters of the control loop is the time response of
the thermistors with respect to changes in power input to
the heaters. For this reason, the thermistors were mounted
in a manner to allow the closest possible coupling between
the heaters and the thermistors.

The principal difference between the two stages of
temperature control was that a dc bridge and sensor ampli-
fier were used for the outer stage while an ac excited bridge
and lock-in amplifier were used for the inner stage. The com-
pensation network, power amplifier capabilities and heaters
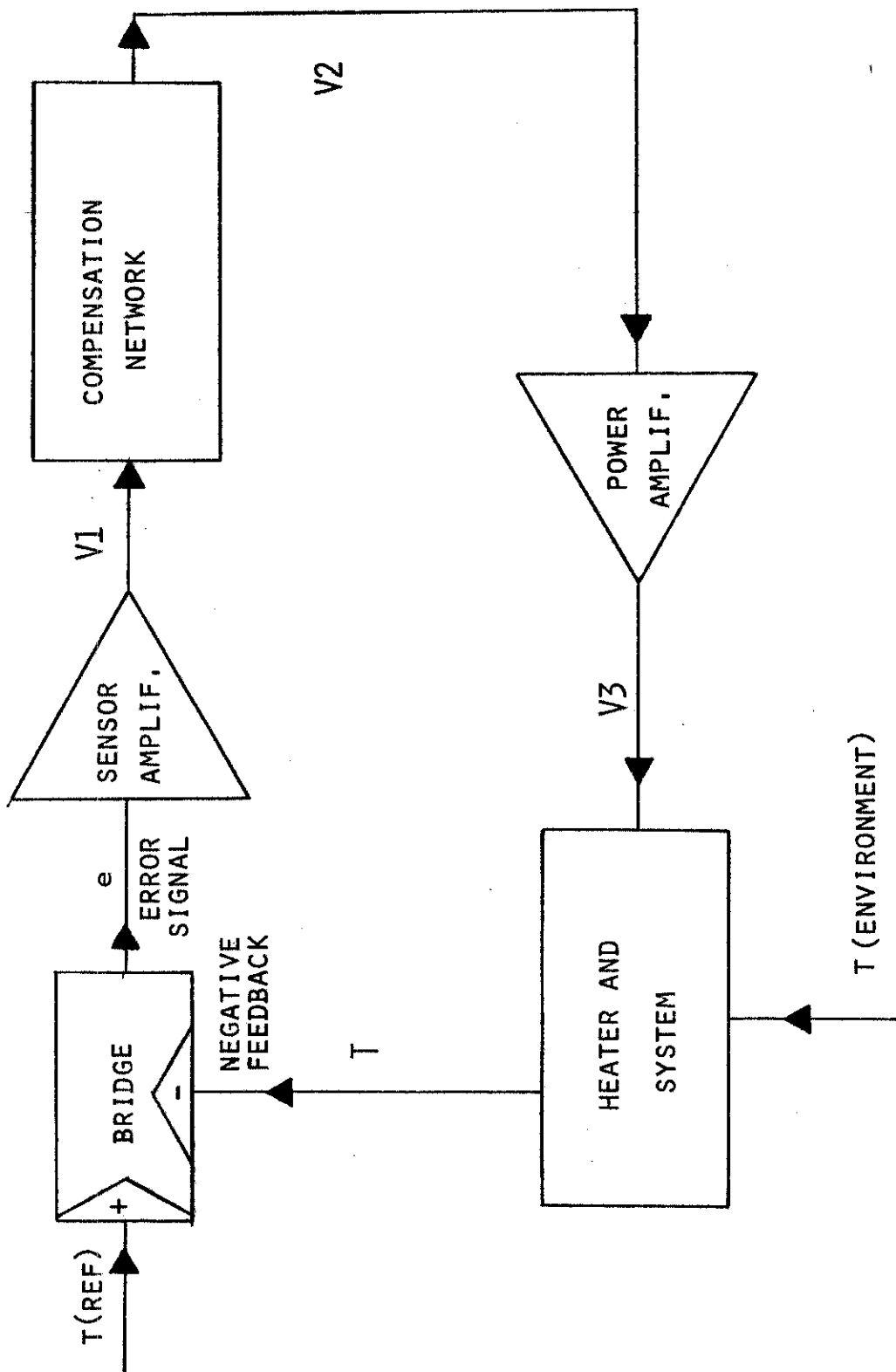
Fig. 23. Block Diagram of Temperature Control Electronics.

were tailored for the requirements of each stage. Values for the heat capacities, thermal resistances, and masses of each stage are given in Appendix V.

Both controllers were designed to allow convenient and accurate changes in operating temperature. The outer stages setpoint could be changed in 2 mK increments with the use of a switched resistor network. Setpoints for the inner stage were changed with a seven-digit ration transformer which permitted 10 μK increment changes.

Performance of the outer control stage was checked by using the inner stage detector system as a temperature monitor. When this stage's compensation network was adjusted as described in Appendix V, temperature deviations from the setpoint, measured over a ten hour period, were no greater than ± 0.5 mK. The only check on the inner control stage's performance was to monitor the stability of the interelectrode spacing. The results of this check are given in Chapter IV where it is shown that no changes in electrode spacing due to temperature variations were observed. A major indication of the sensitivity of the inner stage controller was that a setpoint change of 30 μK would cause an observable change in the output of this stage's sensor amplifier. The response of both stages to setpoint changes is described in Appendix V.

Vacuum System For the Tunneling Experiment

A schematic diagram of the vacuum system used for the
tunneling experiment is given in Fig. 24. The vacuum chamber
and pumping system were constructed from 304 stainless steel
with standard UHV copper gasket flanges employed for all
connections between system components. The system was pumped
from atmospheric pressure down to the operating pressure using
only the three pumps shown in Fig. 24 in order to avoid expos-
ing the gold electrodes to any unnecessary hydrocarbon gases.
Base pressure of the vacuum chamber as determined by a cross
check of the ion-pump current and the Bayard-Alpert gauge
was 5×10^{-9} to 1×10^{-8} Torr after several weeks of pumping.
The Bayard-Alpert guage was not operated during the critical
temperature control parts of the experiment.

Electrode Holder and Micropositioning Assembly

The final design of this critical part of the vacuum
tunneling experiment is shown in Fig. 25. A photograph of
the electrode assembly, along with the temperature control
heaters and vacuum system is given in Fig. 26. The assem-
bly as shown in Fig. 26 provides a system which is compatible
with ultra-high vacuum, has mechanical rigidity to maintain
electrode spacings to stabilities of approximately 1 pm,
and permits the electrodes to be assembled into a tunneling
structure on a laboratory scale. In addition, the assem-
bly is capable of producing interelectrode spacings of

OVERPRESSURE RELEASE

SORPTION PUMP

TITANIUM SUBLIMATION PUMP

BAYARD–ALPERT TYPE IONIZATION GAUGE

THERMO-COUPLE GAUGE

FORELINE VALVE

UP–TO–AIR VALVE

VACUUM CHAMBER

GOLD SEAL UHV VALVE CONDUCTANCE FULL OPEN 10 L/S

TRIODE ION VACUUM PUMP 20 L/S

20 PIN ELECTRICAL FEEDTHROUGH
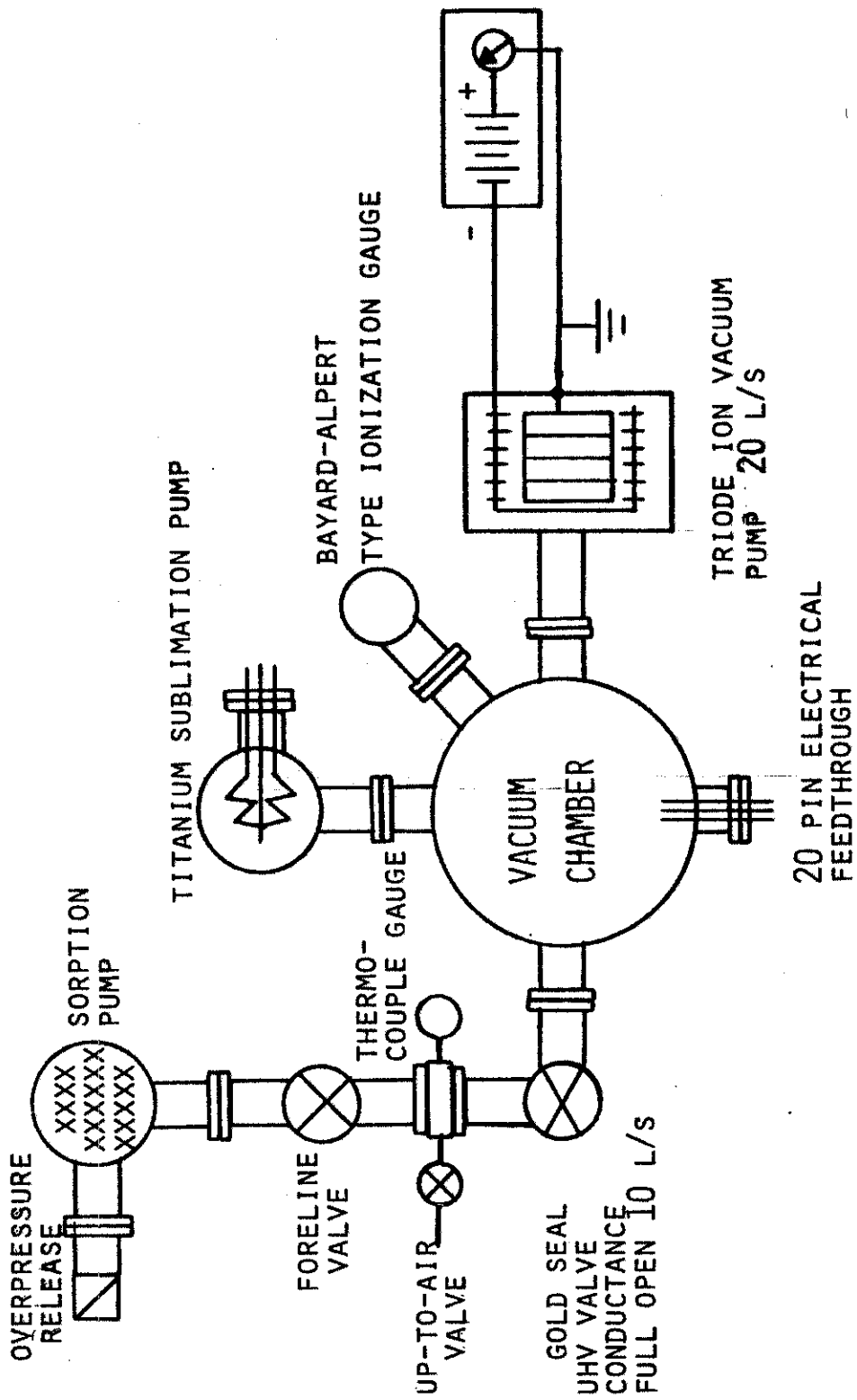
Fig. 24. Schematic Diagram of Vacuum System Used for the Tunneling Experiment.

Fig. 25--Electrode Holder and Micropositioning Assembly.
(1) Housing for electrode holders. This housing is basically
an aluminum (6061 alloy) block 8.9 cm x 6.35 cm x 6.35 cm with
a 3.17 cm hole bored and reamed to accept the electrode holders.
The diameters of the electrode holders were machined to match
the hole in the housing to a clearance no greater than 0.01
mm. (2) Gold electrodes. In the experiment, both gold wires
were inserted into their respective holders as far as the
spherical ends would allow. (3) OFHC copper mount for the
differential-screw mechanism and main body of left electrode
holder. (4) 0.025 mm thick polyimide film[52] to provide elec-
trical insulation between the electrical holders and the hous-
ing. (5) Diaphragm flexures. The thickness of both flexures
was 0.38 mm. (6) Threads to allow prestressing of the piezo-
electric element-diaphragm flexure system. (7) Prestressing
nut. (8) Hardened steel washer to prevent motion transfer
between prestressing nut and the piezoelectric element. (9)
Electrical connections to gold electrodes. (10) Clamp-holder
for left electrode, OFHC copper. (11) Threads to allow mounting
of the differential-screw mechanism. (12) Hardened steel end
caps to distribute stress uniformly over piezoelectric ele-
ment's surface. (13) Clamp-holder for right electrode. (14)
Support for outer diaphragm flexure, OFHC copper. (15) PZ
displacement element.

1.5cm
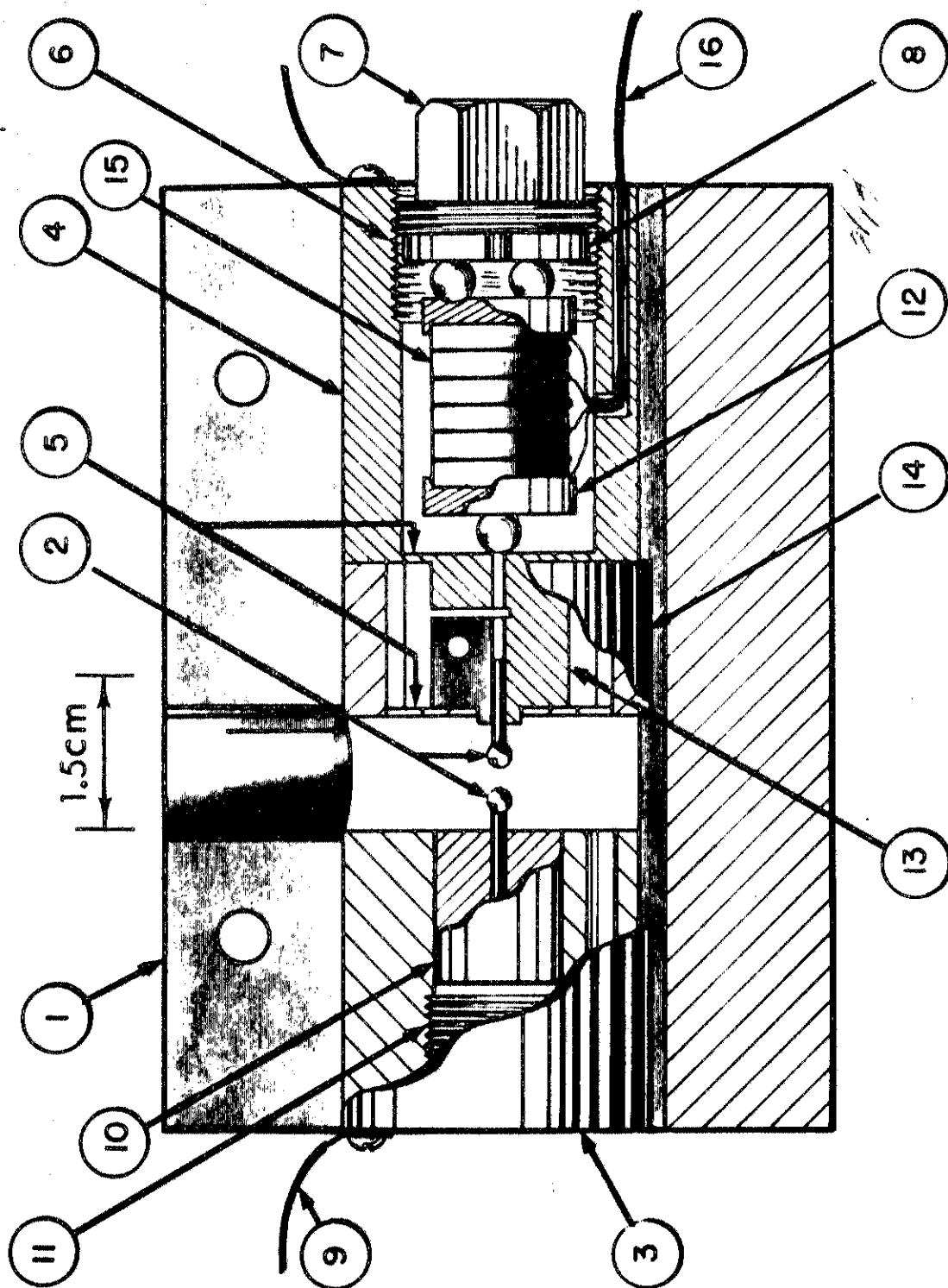
Fig. 26. Photograph of Electrode Assembly,
Temperature Control Heaters and Vacuum System.

one to two nm and has the facility to change the electrode spacing in a rapid and convenient manner.

The basic approach of this design is that a precision-differential screw mechanism is inserted at point 11 in Fig. 25 to position the left electrode clamp, item 10, which contains one gold electrode until the electrode spacing is less than the distance which can be spanned by the piezoelectric (PZ) element. At this point, all components of the assembly are clamped rigidly in place, the differen-tial-screw mechanism is removed, and final fine tuning of the electrode spacing is achieved by temperature adjustment and piezoelectrically generated displacements of the second electrode holder.

With reference to Fig. 25, the left electrode holder is composed of the electrode clamp, and a differential-screw-mount. Both were made of OFHC copper to obtain minimum thermal resistance between the electrode and the holder housing and minimum electrical resistance between the electrode and its electrical connection. The electrode clamp was essentially two half-cylinders connected together by a 0.25 mm x 0.5 mm flexure along the length of the clamp and located next to the hole for the electrode. A separate screw is provided for clamping the electrode into place. The mount for the differential-screw had a similar form. All other clamping is performed with the electrode-holder housing which is cut only in the shaded area of the drawing.

Each vernier division of the differential-screw-mechanism corresponded to an output displacement of about 25 nm. This resolution was such that approximately one-quarter turn of the differential-screw's input covered the PZ element's 500 nm range.

The right electrode holder consisted of an electrode clamp mounted to a double diaphragm-flexure support to insure axial motion of the electrode, a PZ element, and a mechanism to prestress the driving element-flexure combination so that microscopic motion losses would be minimized. End caps for the PZ element and the prestressing mechanism were made from hardened steel. The diaphragm-flexures and piezoelectric element were prestressed with a force of approximately 890 N (200 pounds). All other parts of the electrode holder, except the 304 stainless steel fasteners, were machined from OFHC copper. The PZ element was electrically insulated from the rest of the holder with four sapphire spheres.

The PZ element consisted of six ceramic discs, each 1.27 cm in diameter by 0.25 cm thick. The ceramic was a barium-titanate-zirconate composition which has very low hysterisis, linear characteristics[50]. The relevant expansion coefficient for the material is $d_{33} = 225$ pm/V for fields along the poled direction of the ceramic; here perpendicular to the disc faces. The individual discs and end caps were bonded into one element with the use of a low viscosity, electrically conductive epoxy. The epoxy's electrical

resistivity was less than 0.002 ohm-cm[51]. After baking in air at 100°C for one hour, the outgassing rate was sufficiently low that the 10^{-10} Torr base pressure of a bell jar system with a 50 l/s ion pump was unaffected by the presence of the epoxy bonded piezoelectric element.

Displacement characteristics of the completely assembled micropositioning system were measured before and after the tunneling experiments described in Chapter IV. Before the experiments, the displacements were measured with a precise but uncalibrated mechanical gauge to be (.56 ± .06) nm/V. After the experiment, the displacements were measured with a Hewlett-Packard 5526A laser interferometer measurement system in combination with a 10565B remote interferometer and retroreflector. This measurement system enables displacements to be measured with an accuracy of ± 25 nm. For both expansion and contraction of the piezoelectric element, the displacements were measured as (0.47 ± 03) nm/V. Thus, taking into account the uncalibrated state of the mechanical gauge, the displacement characteristics of the micropositioning system were stable throughout the experiment.

The need for one pm electrode spacing stability combined with the 470 pm/V displacement sensitivity of the PZ element requires that the high voltage power supply used to drive the PZ element have a very low voltage noise level. These two constraints required that the noise level be less than 2 mV. The power supply used for this purpose had a noise

level of less than 75 μV peak-to-peak and the capability
of being switched in 1 mV increments from -1100 volts to
+1100 volts[53]. To enable continuous voltage sweeps over
± 10 volts, a ramp generator was added in series with this
power supply. The circuit diagram of the ramp generator
and a filter circuit to suppress switching transients are
shown in Fig. 27.

Two other experimental techniques for holding and
positioning the tunneling electrodes were thoroughly explored
before finally adopting the electrode holder and micro-
positioning assembly design just described. The technique
first explored was to fabricate the tunneling structure as a
microelectronic device with the use of photolithographic
methods. This approach was not adopted because the technol-
ogy to which the author had access could not meet the
dimensional requirements of the tunneling device. However,
as a byproduct of this work, the approach may result in an
electronic device with a very high transconductance; values
up to 1 mho appear feasible. A patent application on the
concept is being submitted to the National Bureau of Standards
Patent Review Committee. The concept and a prototype device
are described in Appendix IV.

Lever amplification of the piezoelectric element's length
changes was also explored as a possible means to bridge the
gap between laboratory scale distances and the microscopic
dimensions required by the tunneling experiment. While this
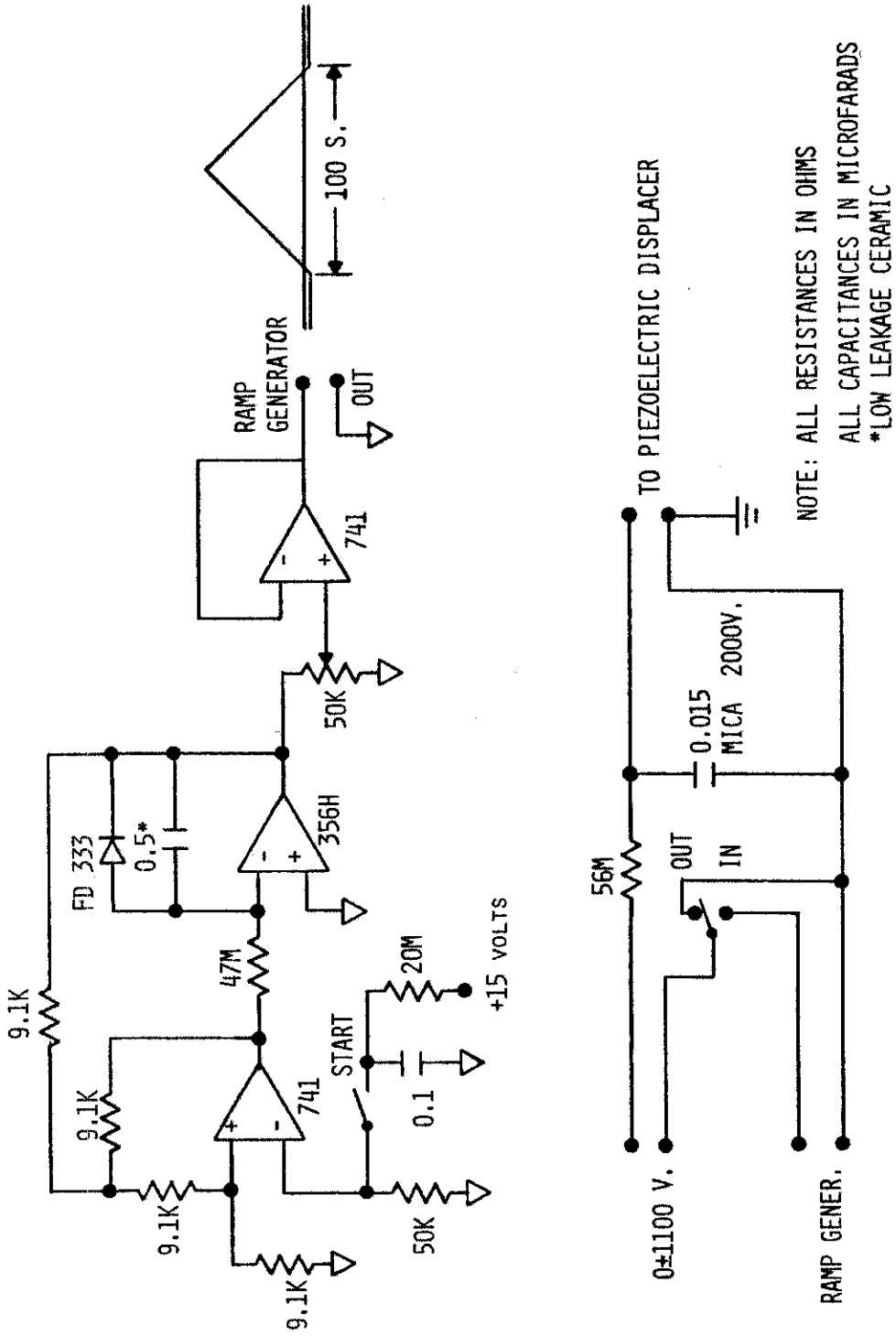
Fig. 27. Schematic Diagram of Ramp Generator and High Voltage Power Supply
For the Piezoelectric Element.

technique proved to have excessive vibration levels for the tunneling experiment, it has characteristics which are very useful for scanning-electron and optical microscope stages[54].

Vibration and Acoustical Isolation

In the previous metal-vacuum-metal tunneling experiment[2a] similar to this work and in all earlier attempts made in connection with this work, vibrations of the tunneling device structure at the one nm level have limited a successful execution of the experiment. Every effort was, therefore, made to carefully examine the mechanical design of each part of the apparatus to insure that all known sources of vibrational energy were attenuated to levels which would not result in detrimental changes in the electrode spacing. The vibrational properties of what was thought to be the most likely contributors to changes in electrode spacing will now be described in terms of one-dimensional models.

Starting with the electrode holder and micropositioning assembly, the most likely contributor is vibrational motion of the right electrode holder as the entire assembly is vibrated along the assembly's axis. This motion could be produced either from acoustical pressure variations on the bottom of the vacuum chamber or from building vibrations driving the isolation table top and, thus, the entire vacuum chamber. As a model of this motion, let a mass, m, be connected by a spring with force constant k, and a viscous damper characterized by the

constant C, to a vibrating wall whose displacement is given by $x_W = A_0 \sin Wt$. Then, the equation of motion of m in terms of x, measured relative to the wall, is

$$m(\ddot{x} + \ddot{x}_W) + C\dot{x} + kx = 0. \tag{3-6}$$

The steady state solution to Eq. 3-6 with the assumed form of x_W is

$$x = R^2[(1-R^2)^2 + 4V^2R^2]^{-1/2} x_W, \tag{3-7}$$

$R = W/W_0$, $W_0 = (k/m)^{1/2}$, and $V = 1/2C(mk)^{-1/2}$. If W is much less than W_0, then

$$x = R^2 x_W. \tag{3-8}$$

Thus, if W_0 is the lowest resonant mode frequency of the micropositioning assembly for axial vibrations and the full amplitude of the isolation table top's horizontal motion is transmitted along the axis to the electrode holder housing, $f_0(= W_0/2 \text{ pi})$ must be greater than 6 kHz. This follows with the use of an W of (2 pi)30 radians/sec, an x_W of 40 nm and a requirement that x be less than one pm. The only mechanical element with a resonant frequency near this value is the diaphragm flexures, which were designed to have a resonant frequency of 10 kHz, when unstressed. When stressed, the frequency would be even higher and motion would then be determined almost entirely by the prestressing mechanism.

For motions normal to the axis of the assembly all reson-
ant frequencies are much higher than 10 kHz. The relatively
large gold wires were used to avoid low resonant frequencies
in these directions. For example, even with a very high
modulus of elasticity material such as tungsten, the trans
verse vibrational resonant frequency of a cantilever only
2 mm long and .025 mm in diameter is 4 kHz[55].

To minimize the affects of any acoustically generated
vibrations the electrode holder and micropositioning assembly
are only connectedmechanically to the laboratory environment
by the bottom plate of the vacuum chamber. This plate is
heavily damped both by the epoxy layer for attaching the
heater wires and by the polyurethane foam.

The four lowest eigenfrequencies of the bottom plate
are approximately: 884 Hz, 1.85 kHz, 3.0 kHz, and 3.5 kHz[55].
These neglect any mass loaded increases in the frequencies
due to the mass of the tunneling assembly, which is sup-
ported by the plate and any increases in the frequencies
due to the epoxy damping. The lowest of these frequencies
again is the most likely source of transmitting acoustical
pressure variations to the electrode assembly. As a safety
factor for design, a 40 dB white noise spectrum was assumed
to exist up to one kHz, i.e., pressure variations, P_W, with
amplitudes of 2×10^{-3} N/m^2. For frequencies much less
than the eigenfrequencies, the vibrational amplitudes, Y,
of the plate at the center of the plate would be[55]

*

$$Y = 3P_W(1-s^2)a^4/(4tQ), \qquad\qquad (3-9)$$

s = Poisson's ratio = 0.33, a = radius of the plate = .127 m,

t = thickness of the plate = 1.9 cm, and Q = modulus of

elasticity of the plate = 1.86 x 10^{10} N/m^2. With the

indicated P_W, Y is only 8.7 pm. For frequencies on resonance,

the amplitudes of vibration should be no larger than ten times

this value with the epoxy and polyurethane damping[56]. Since

the assumed pressure variations were larger than expected

and did not account for any attenuation due to the polyure-

thane foam, no further stiffening of the plate was performed.

Tunneling Electronics

The electronics used to measure the conduction properties

of the tunneling devices are shown in Figs. 28 and 29.

Requirements of the electronics were that it permit one to

test devices whose impendences could range from 10^{-2} to 10^{11}

ohms with dc test voltages of typically 10 mV. The design

shown in Fig. 28 utilized an operational amplifier in a

follower configuration to insure that other than voltage

drops in the current leads the output impedance of the vol-

tage source would be less than 0.005 ohm. The operational

amplifier was a 356H integrated circuit device. The four-

wire lead system was carried through to the connection

points on the electrode holders shown in Fig. 25.

With all systems of the tunneling experiment in opera-

tion, i.e., vacuum system, temperature control system, high

BLOCK DIAGRAM OF
TUNNELING ELECTRONICS
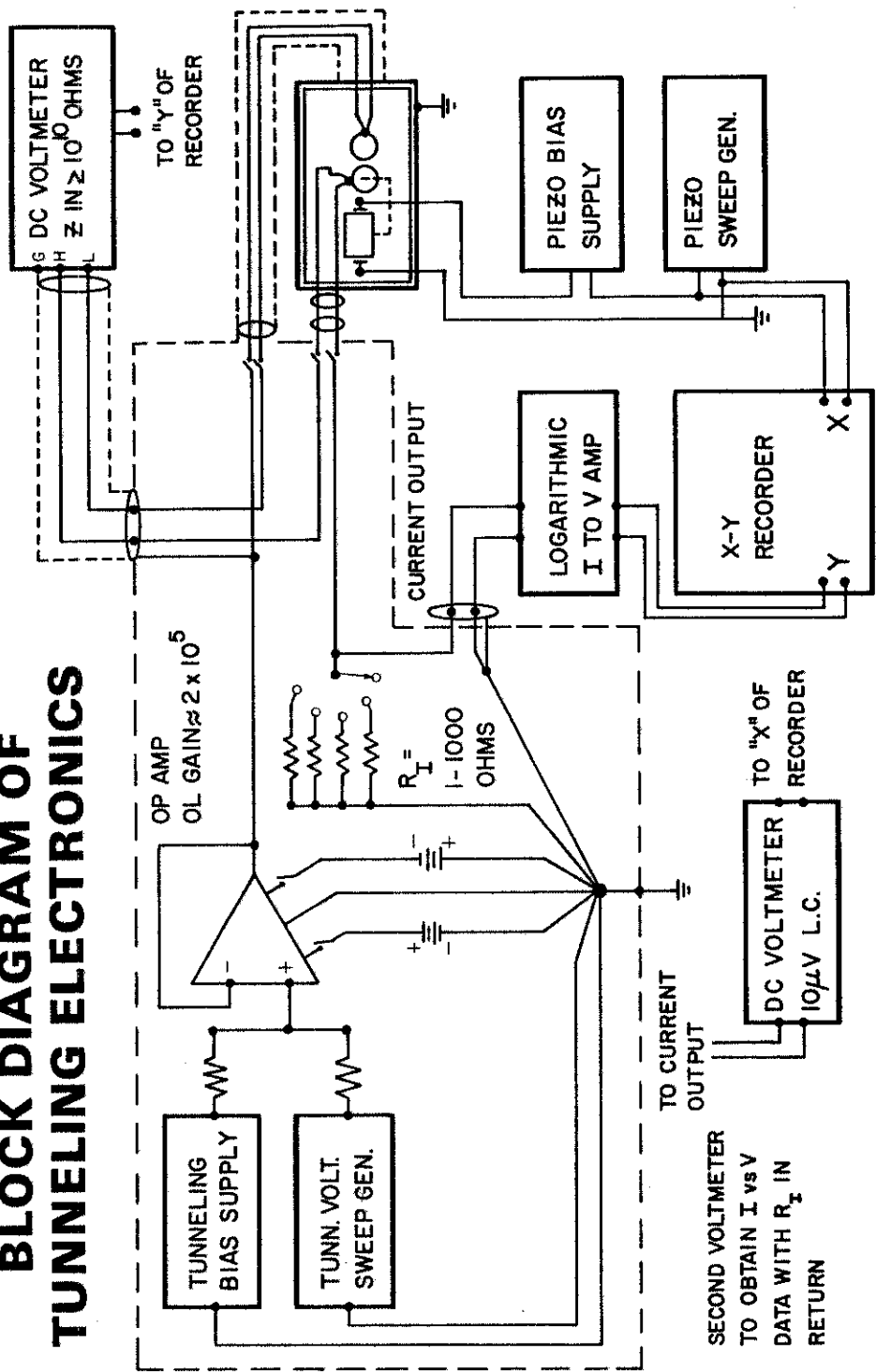
Fig. 28   Block Diagram of Tunneling Electronics.
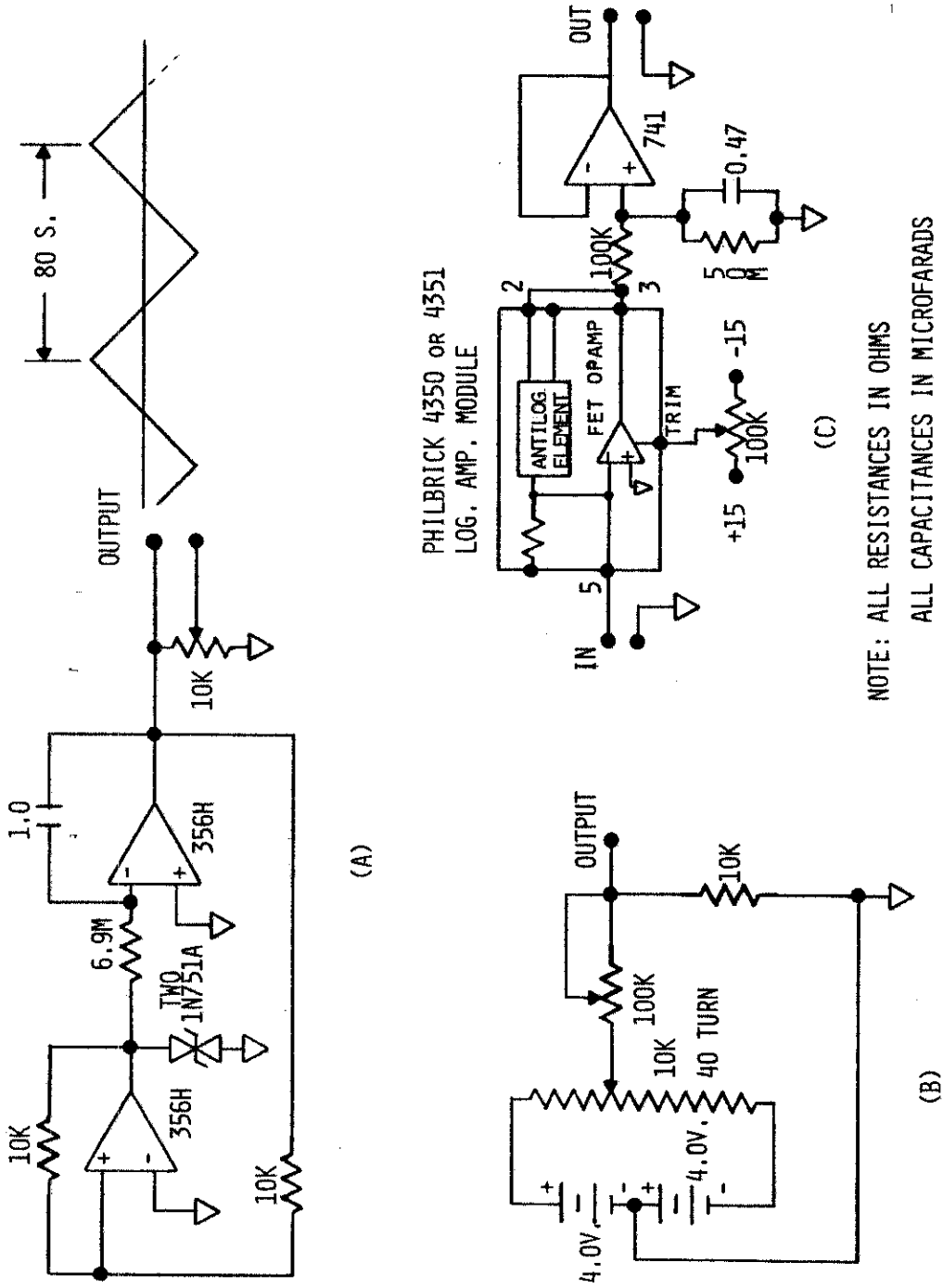
Fig. 29. Schematics for Components of the Tunneling Electronics.
(A) Ramp Generator for sweeping bias voltage. (B) Manual Sweep and Bias
Supply. (C) Logarithmic Amplifier.

voltage power supply for the micropositioning assembly,
and the tunneling electronics, the total system was care-
fully debugged for ground loop problems and 60 Hz pickup.
The noise current in the tunneling electronics after this
process was about 10^{-11} A. This value was measured with
a 10^8 ohm test resistor substituted for the tunneling device
and obtained from both the I-V characteristics of the
resistor and the output of the logarithmic current to voltage
converter. The major source of this noise was the operational
amplifier and could have been reduced with a more elementary
resistive voltage generator. However, the level was adequate
for this experiment, and the alternative was a greatly
increased source resistance.

Both dc voltmeters employed with the tunneling
electronics had floating-guarded inputs with dc common-mode
rejection ratios of greater than 140 dB. The voltmeter
used to measured the bias voltage applied to the tunneling
device had a gain of 10 with readout resolution to 10 uV
The voltmeter for measuring the tunneling current, in the
I-V configuration of the electronics, had variable gains
up to 10^6 with a meter noise of about 150 nV p-to-p.

The logarithmic current-to-voltage amplifier output was
trimmed according to the manufacturers specifications. After
warmup, the offset was less than 100 uV. Specifications
for the amplifier modules were that the output voltage would

be a linear function of the logarithm of the input current over a range from 10^{-9} to 10^{-3} A to within one percent. Measurements with test resistors showed that, in addition, the nonlinearity was only five percent for the positive polarity module and less than two percent for the negative polarity module for currents of 10^{-10} A. To reduce the acoustical noise level of the chart recorder when the tunneling device formed an open circuit, a lowpass filter with a cutoff frequency of 32 Hz, see Fig. 29c, was installed.

In operation, the electronics were changed from the Log I_{cv}-D configuration shown in Fig. 28 to the configuration for I-V measurements by first shorting the input of the Log module with the one ohm resistor, disconnecting the Log module and the piezoelectric sweep generator and finally connecting the dc voltmeter for current detection. Changing back to the Log I_{cv}-S configuration was performed in a similar manner.

CHAPTER IV

RESULTS AND ANALYSIS

Taking into account the extreme delicacy of the inter-
electrode spacing adjustments, the apparatus described in
Chapter III has proven to be very reliable and to give
reproducible results. The data which will be presented was
obtained with the same essential characteristics in two sep-
arate experiments with data being obtained over a period of
several weeks in both instances.

After several unsuccessful attempts at getting the app-
aratus to perform as anticipated, a standard sequence of
operations was evolved which permitted the experiment to
be carried out in a consistent manner. Following formation
of the electrodes and their installation into the holder
and micropositioning assembly, as described in Chapter III,
the assembly was placed on a temperature-controlled plate
of copper. The temperature of the plate was maintained at
(300 $\pm$ .05) K which was the planned operating temperature
for the experiment. The electrode spacing was then observed
with a low power stereo-microscope and adjusted with the
differential-screw mechanism until the electrodes appeared as
shown in Fig. 30.

Concurrent with this adjustment the current flow through
the electrodes for an applied voltage of 10 mV was monitored

Fig. 30. View of Gold Electrodes Mounted in Electrode Assembly. All the apparent structure and cuts in the electrodes are images formed by the mirror like properties of the electrode surfaces.
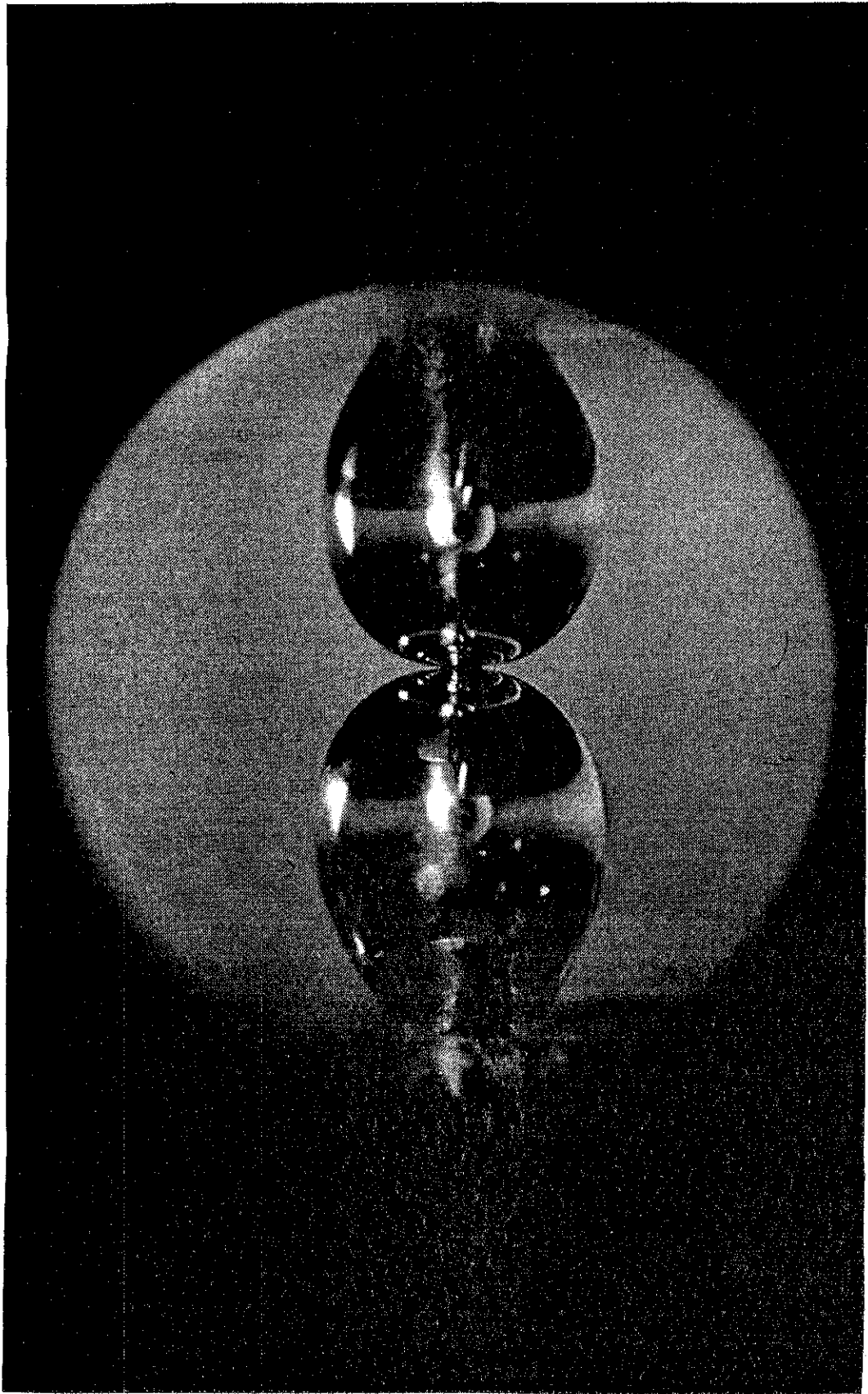
with the tunneling electronics. Final adjustment of the left
electrode in the sense of Fig. 25, was such that with the PZ
element at the maximum extension possible in air the elec-
trodes would just make contact. Since the extension of the
PZ element in air was only 0.7 of that possible in vacuum,
slight misadjustments could be corrected after installation
in the temperature control and vacuum system. Misadjustments
out of range of the PZ element, either in contraction or
expansion, could be corrected with small, ± 0.5 K, changes
in the operating temperature. Use of the temperature control-
led copper plate was required to overcome the expansion and
contraction generated by unknown changes in temperature re-
sulting from body heat during the adjustment process.

All parts of the electrode holder and micropositioning
assembly were firmly clamped in place at this time. The
assembly was then allowed to equilibrate with "hands-off."
(Plastic gloves over cotton gloves were actually used at
all times during the assembly to provide thermal insulation
and to insure the cleanliness required for UHV.) After con-
firming that an open and a short could be produced by
contracting and expanding the PZ element, the electrode
assembly was installed in the vacuum system and pumped to
a pressure of approximately 1×10^{-8} Torr. This usually re-
quired several weeks with the small ion pump which was used
on the vacuum system.

Determining the PZ element voltage and operating temp-
erature at which the electrodes were positioned to within
1 to 2 nm of each other was accomplished by searching for
the abrupt change in tunneling current as the electrode spac-
ing was swept through the tunneling region. With the circuit
shown in Fig. 27 the sweep rates for a range of 5 nm was
approximately 0.1 nm/s. The search was greatly facilitated with
the logarithmic current amplifier. In fact, all attempts at
finding the required PZ voltage and temperature settings with-
out the use of a logarithmic amplifier were unsuccessful.
After completing this procedure to locate the tunneling region
the first time, successive searches were not difficult.

Data and Analysis

The first sets of Log I_{cv}-S data, while exhibiting the
character of many orders of magnitude change in current over
1 to 2 nm change in electrode spacing, contained much structure
akin to noise, see Fig. 31. Some of the structure may however
be due to the oscillations in the tunneling probability predic-
ted by numerical calculations based on an exact solution to
Schrödingers equation[34]. Regardless of the possibilities, the
exploration of the phenomenon was prevented by an accidental
electrical discharge as an attempt was being made to measure
the constant-current characteristics which were measured in
both previous vacuum tunneling experiments[2].

124
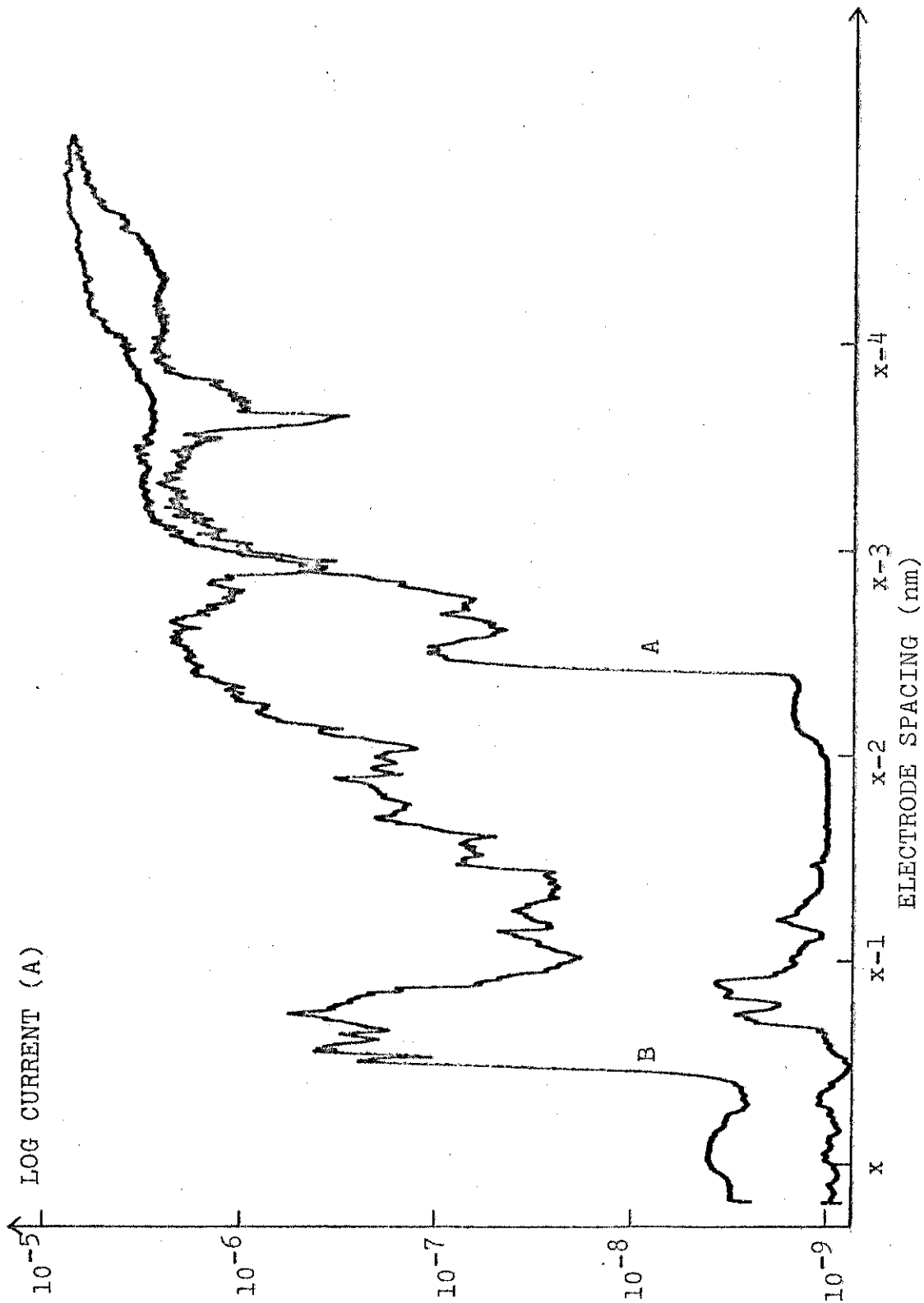
Fig. 31. One of the First Measured Log Current-Spacing Characteristics. Curve A was measured as the PZ element was expanded then curve B as it contracted. The hysteresis is a combination of hysteresis in the PZ element and mechanical relaxation of the electrodes. Cycling gave reasonable reproduction of both parts of the graph.

The series of measurements which were made subsequent
to this accidental discharge of the constant-current power
supply will be referred to as the first experiment. Represent-
ative Log I_{cv}-S data obtained during this experiment are given
in Figs. 32a and 32b. A comparison of Figs. 32 and 31 shows
that much of the structure present in Fig. 31 was probably due
to fluctuating surface conditions. The larger scale oscilla-
tions in Fig. 31 were not found in any subsequent Log I_{cv}-S
measurements even though they were consistently present in all
measurements prior to the accidental discharge. Exploration
of the meaning of the oscillations and the conditions necessary
for their observation was left for future experiments.

The overall shape and features of the data shown in
Fig. 32 were reproduced about 50 times over a period of several
weeks. Small changes in average slope and local details were
observed as the electrodes were brought into contact during
repeated closing and opening of the electrode spacing. All
the Log I_{cv}-S data had three characteristic regions. Expressed
in terms of the tunneling current, the first of these regions
was the initial transition into the current range of the Log
amplifier. This region extended up to currents of approx-
imately 10^{-10} A and covered the non-linear part of the Log
amplifier's response. The direct tunneling region usually
extended from currents of 10^{-10} A up to 10^{-5} A for bias
voltages of 10 mV. The final region occurred as the spacing
of the electrodes was such that multiple portions of the
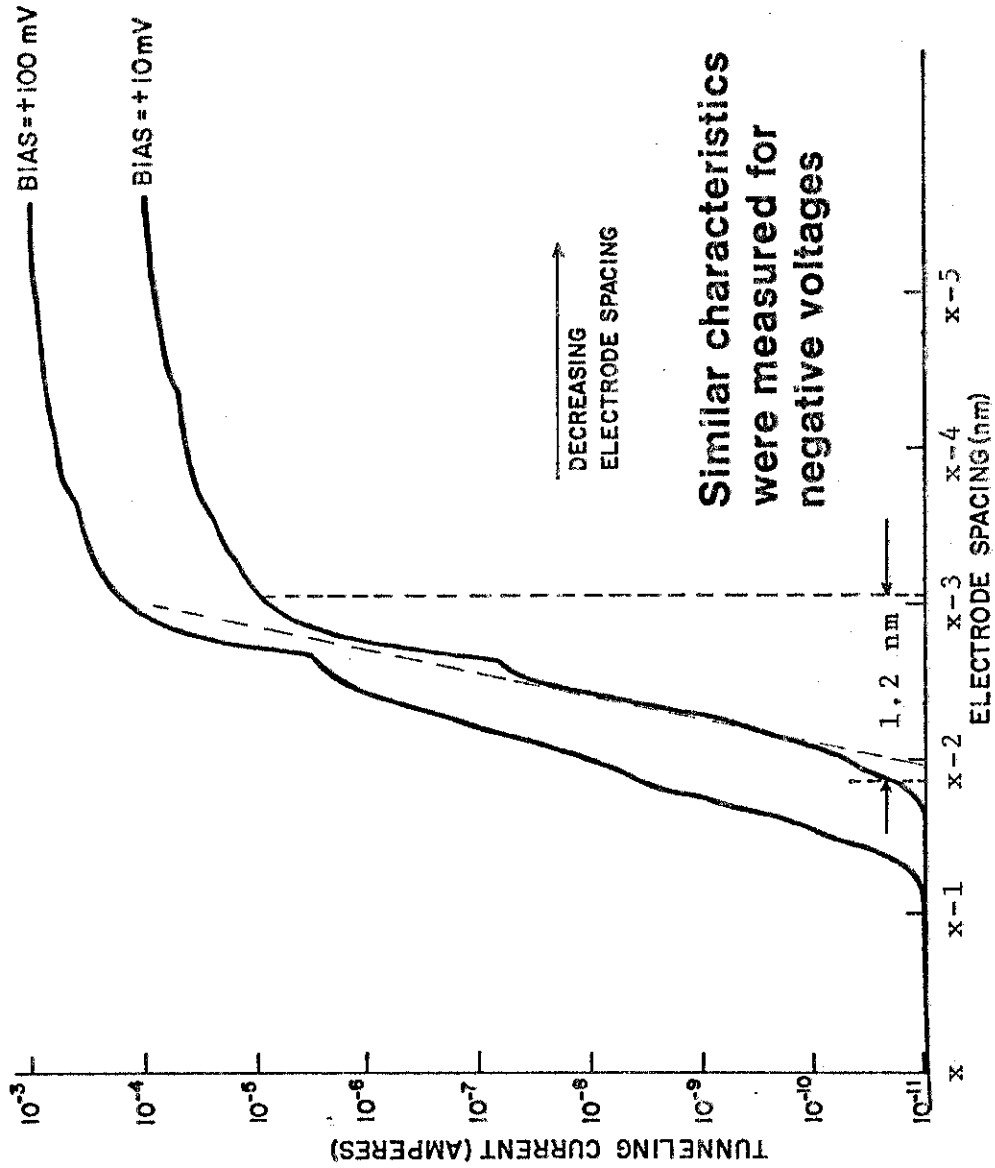
Fig. 32a. Measured Log Current-Spacing Characteristics. The sloping dashed line corresponds to a work function of approximately 3.0 eV. The 100 mV curve was measured immediately following the 10 mV curve. Horizontal placement of the two curves was determined by the zeros of the PZ element's ramp generator.
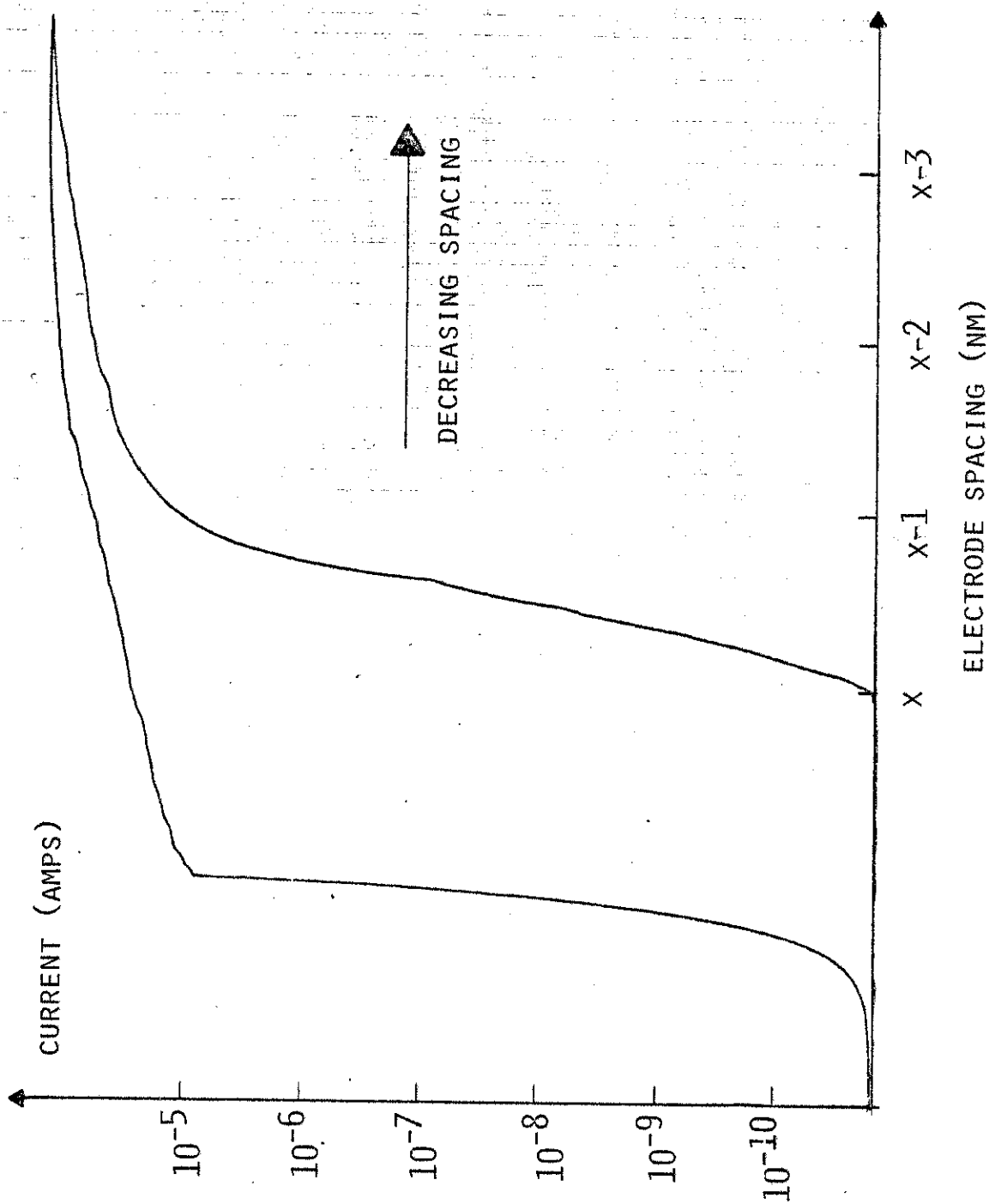
Fig. 32b. Measured Log Current-Spacing Characteristic, Condition A. Bias Vol-
tage = 10 mV. Curve A was measured as the PZ element expanded then curve B.

electrode surface, other than the previously dominant part, began to make significant contributions to the total current and as the initially dominant portions made contact.

A second attempt at obtaining constant-current measurements was made with a different power supply. In this attempt the transient discharge occurred again and was sufficient to microscopically weld the electrodes. Efforts to melt the bridge resulted in broken lead wires. The entire tunneling system was therefore disassembled, new lead wires installed, repositioned as described earlier, reassembled and all of the set-up operation repeated. Once the vacuum was at the 10^{-8} Torr level, the electrodes were cleaned with controlled capacitive discharges. A representative Log I_{cv}-S graph from this second experiment is given in Fig. 33. Five discharges of both polarities obtained from a 0.47 µfd capacitor charged to 14V were used for the cleaning and/or shaping of the electrode surfaces. The surface condition of the electrodes for the data of Fig. 33 is obviously different from that of Fig. 32, but the average slopes in the direct tunneling region of the two sets of data are approximately equal. The data in Fig. 33 were also reproduced a large number of times over several weeks.

The electrode surfaces were examined in detail after the completion of both experiments. No evidence of the discharges could be found. The changes in surface structure were therefore at a sub-microscopic level.
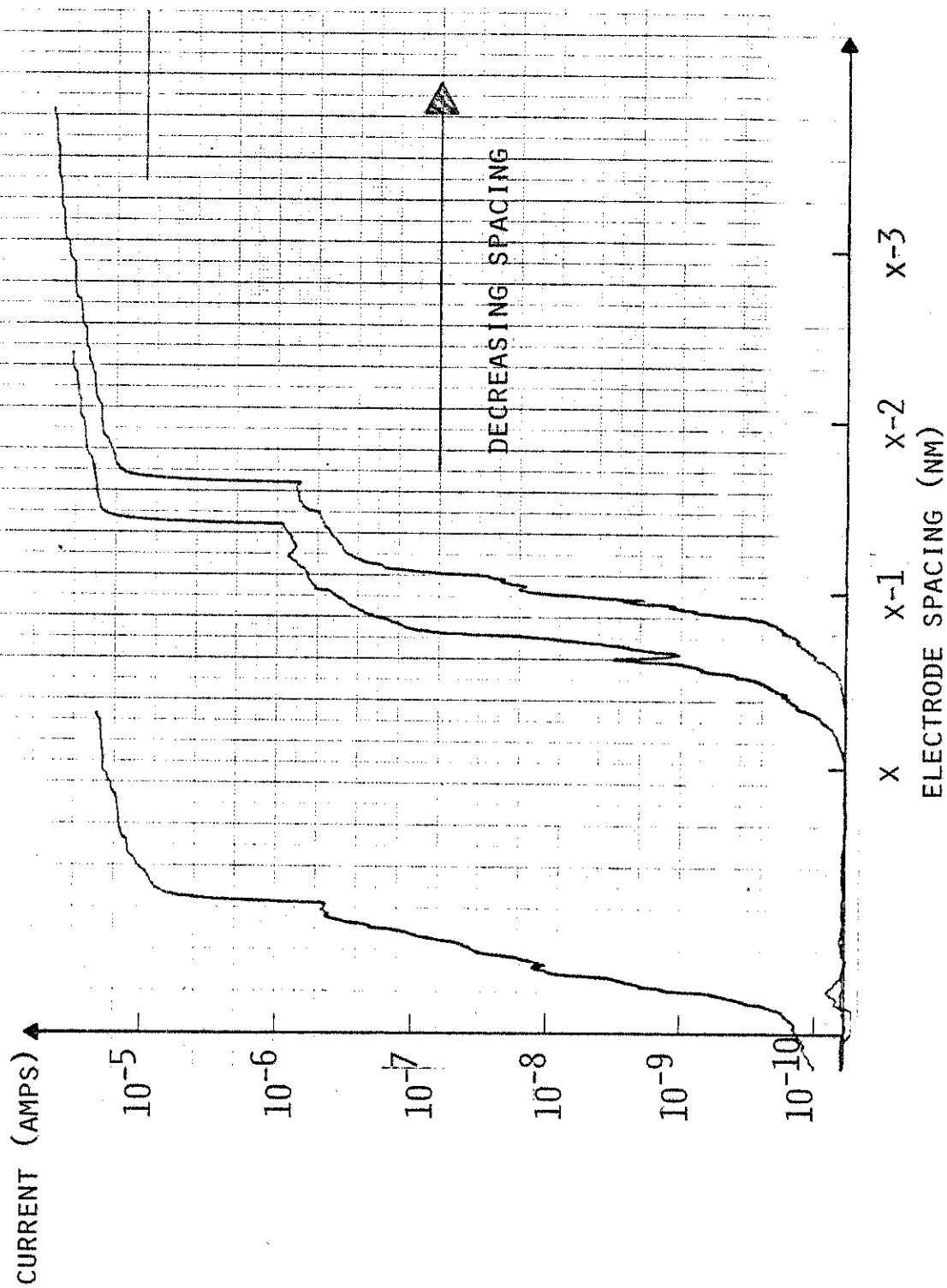
Fig. 33. Measured Log Current-Spacing Characteristic, Condition B.
Bias Voltage = 10 mV.

To confirm that the shape and magnitudes of the Log I_{cv}-S graphs were not being significantly affected by the time response of the Log amplifier, a very slow scan of the PZ element's voltage was performed. The data shown in Fig. 34 were obtained at a scan rate of 0.01 nm/s. One may conclude from a comparison of Figs. 33 and 34 that the shape of the Log curves was not affected.

A Log I_{cv} verses time measurement was also performed to check for temperature and any other instabilities in the experiment. Results are shown in Fig. 35. None of the changes in current appear to be the result of temperature variations since the transitions occur so rapidly. Changes such as the ones shown in Fig. 35 could be due to either sudden changes in surface conditions generated by the relatively large electic fields involved or to motion of the electrode surfaces resulting from lattice relaxation from the strains produced by the mechanical stress of Van der Waals forces and electrostatic forces. The magnitude of these mechanical stresses is discussed in the next section.

The work functions of the electrodes may be obtained directly from the Log I_{cv}-S data given in Figs. 32 and 33. The slope of these curves in the direct tunneling region may be related to the work function with the use of Eq. 2.70. By taking the ratio at two different spacings, one obtains

$$(\ln I_1 - \ln I_2)/(W_1 - W_2) \doteq - a \, B^{1/2} \qquad (4.1)$$
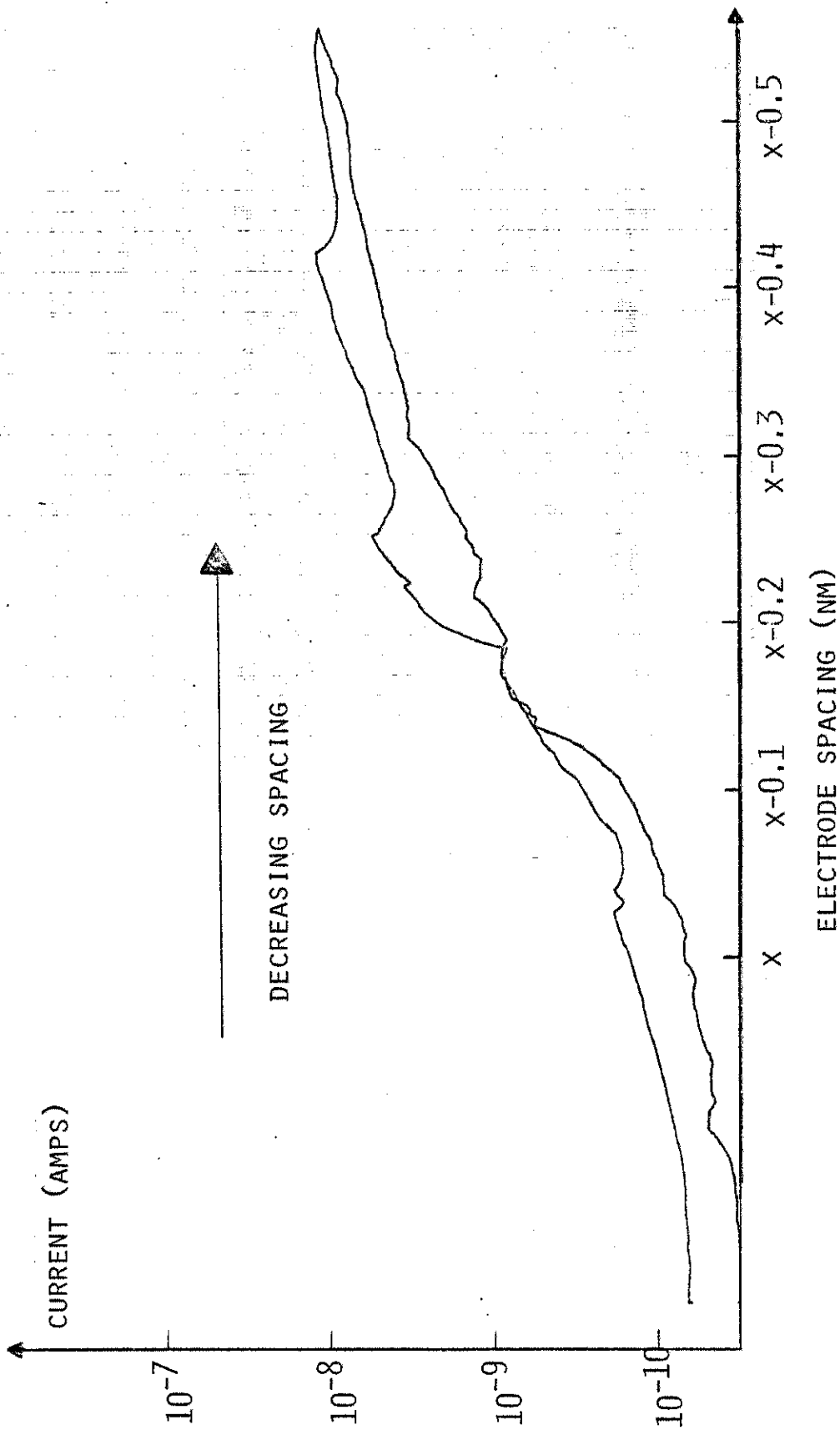
Fig. 34. Measured Log Current-Spacing Characteristic; Expanded Spacing Scale,
Bias Voltage = 10 mV.
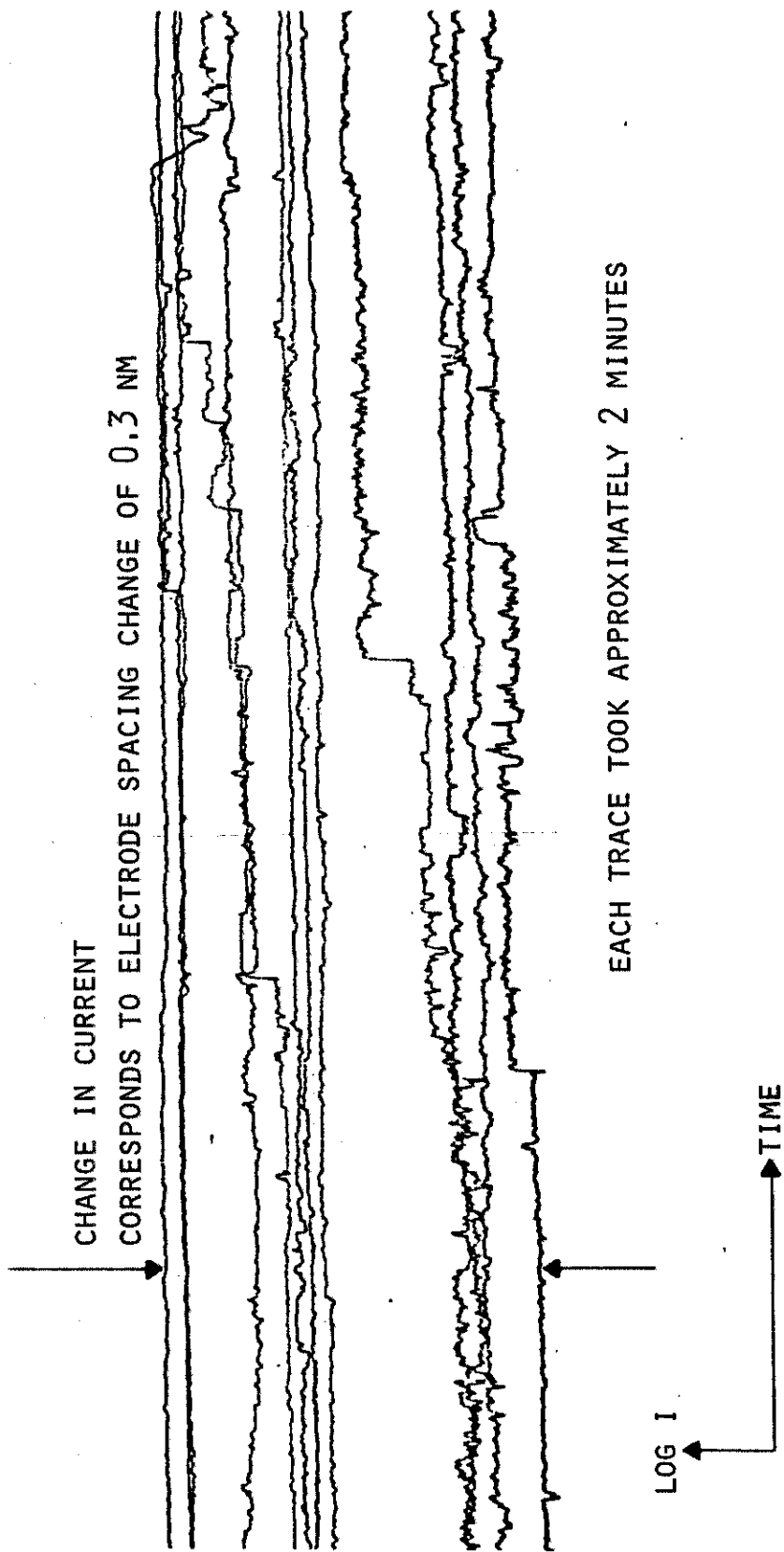
Fig. 35. Log Current Vs. Time for a Fixed Bias Voltage of 10 mV.

where a = 10.25 $(ev)^{-1/2}$ $(nm)^{-1}$. Eq. 4.1 only serves to qual-

itatively illustrate the method of relating the slope to the

WF since B is a function of WF. The exact relation between

the slope of Log I_{cv}-S data and the WF can be obtained from

the calculations of Chapter II. The sloping dashed line in

Fig. 32 was drawn with the use of Tables I and II and Fig. 13.

Based on the discussion of the changes in WF with adsorbed hy-

drocarbons the WF value of 3.0 eV is very reasonable. Note

that this WF value was obtained without the use of any assumed

property of the device or the electrode structure. The only

input information was the piezoelectric element expansion co-

efficient and measured currents. This is the first time that

such measurements have been performed. All previous measure-

ments employed separate tunneling devices with thicknesses

distributed over the values allowed by the fabrication process.

Determinations of the tunneling barrier thickness were also

made from capacitance measurements and therefore were not

independent of the device characteristics.

Current-Voltage measurements of the tunneling device were

made during the second experiment i.e. condition B. The re-

sults for an approximate electrode spacing of 1.2 nm are shown

in Fig. 36. The approximate spacing of the "S" curve was

obtained by determining the PZ element voltage at which touch-

ing occurred, assumed to be at the first major drop in slope

of the Log I_{cv}-S curve, then contracting the PZ element the

desired distance. The other curves were obtained by changing
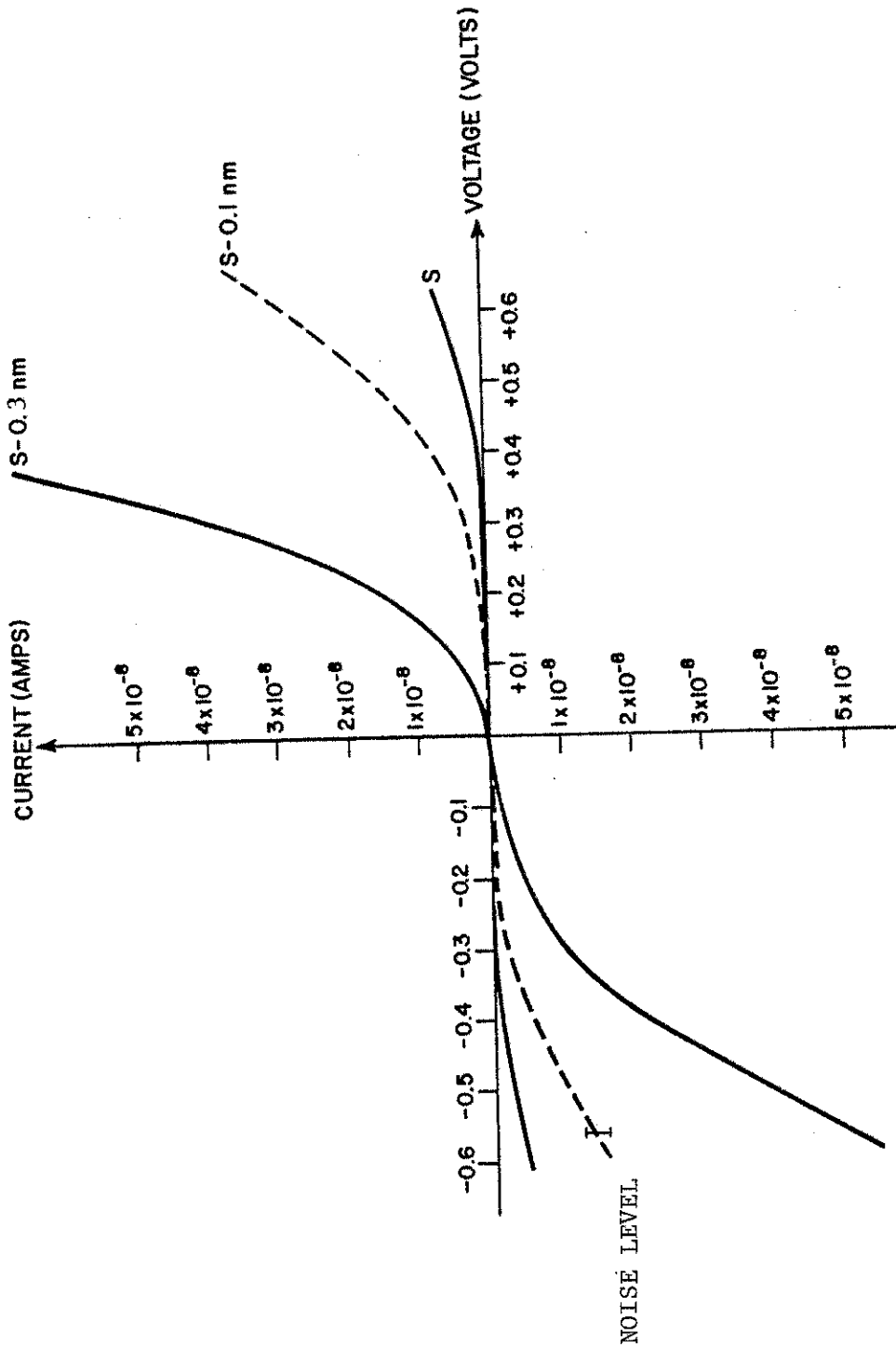
Fig. 36a. Measured Current-Voltage Characteristics For Three Electrode Spacings. S was approximately 1.2 nm. The S, S - 0.1, and S - 0.3 nm curves were drawn manually from the A, B, and C curves of the "raw data" of Fig. 36b, respectively. The uncertainty in S is much larger than that of the difference between the indicated spacings. The indicated noise level was a function of voltage; increasing with increasing voltage. The source of the noise was apparently changing surface condition.
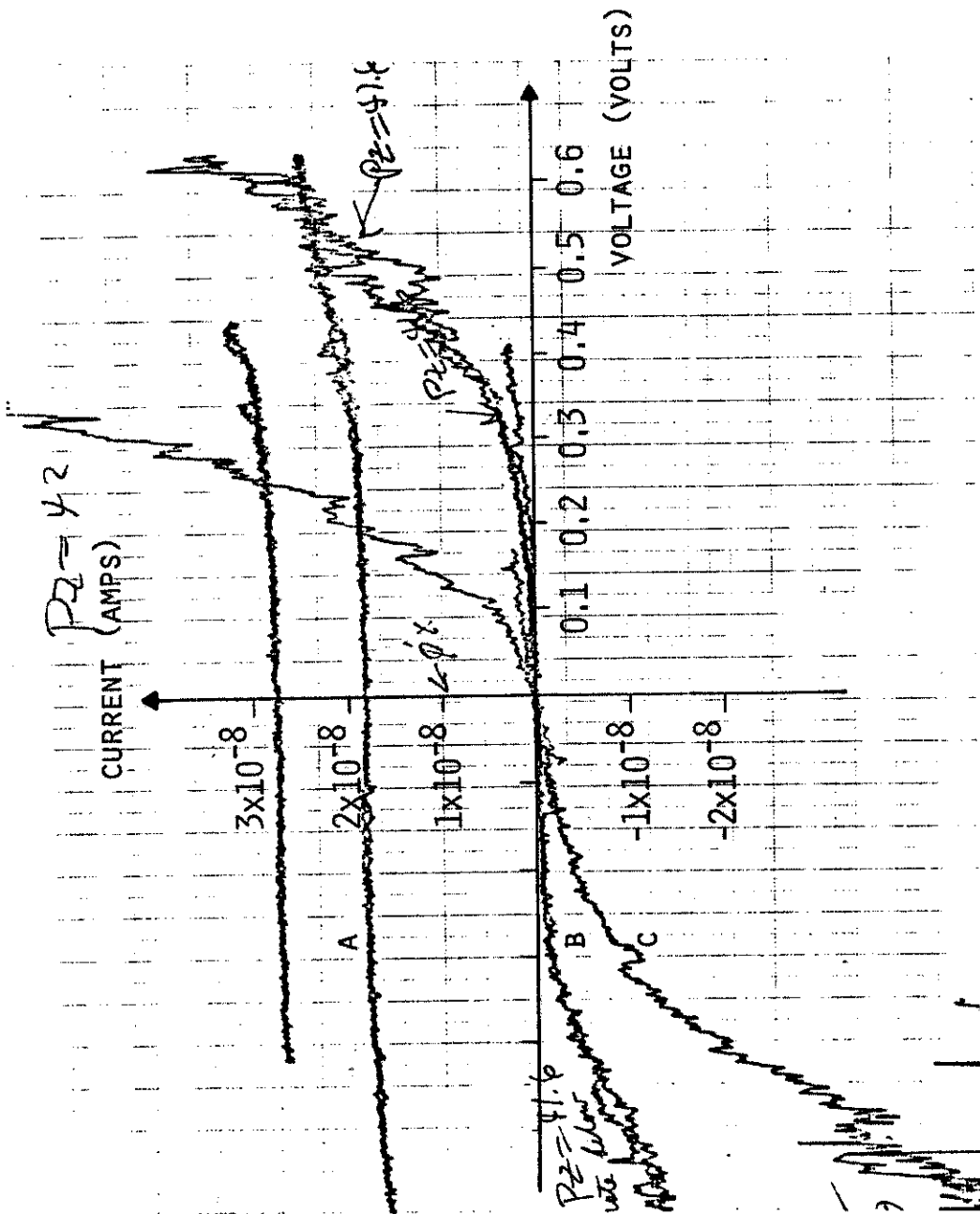
Fig. 36b. Measured Current-Voltage Characteristics for Three Electrode
Spacings. Curves A and B were measured with electrode spacings differing by
0.1 nm; curve C differs in spacing by 0.2 nm from curve B.

the applied PZ voltage by the amount to generate 0.1 nm

changes in electrode spacing ,i.e. 0.2 V.

Many attempts were made to obtain a continuous series

of I-V graphs with electrode spacings varying from 2 nm to

that when the electrodes made contact. In all attempts, the

state of the electrodes did not remain sufficiently stable

for the measurements to be performed. A series of measure-

ments at two to three electrode spacings such as shown in

Fig. 36 was obtained four times.

Relating the I-V data to the theoretical calculations of

Chapter II requires an estimate of the tunneling area and the

absolute electrode spacing. (The deduction of WFs from the

Log I_{cv}-S data only required knowledge of changes in electrode

spacing.) Ideally a consistent approach to obtaining both the

area and the absolute spacing would be first to deduce an

absolute spacing with the use of Eq. 2.73 which relates the

curvature of the I-V characteristics to the barrier height

and spacing. Since the barrier height can be obtained from

the slope of the Log I_{cv}-S data, the absolute spacing would

be the only undetermined parameter. Once it is obtained, the

current density calculations could then in combination with

the corresponding Log I_{cv}-S data and/or the I-V data be util-

ized to calculate an average tunneling conduction area.

Let G(v) = dI(V)/dV, then carrying out this procedure

for the S-0.1 nm curve of Fig. 36 gives G(+0.5)/G(0) = 21.42

and G(-0.5)/G(0) = 12.23. The corresponding S parameters

are S_+^2 = 25.13 B nm^2 and S_-^2 = 15.0 B nm^2. With the B values

calculated from the Log I_{cv}-S data in Fig. 32, both values

are greater than 6 nm. Based on the procedure outlined ear-

lier for obtaining this data S should have been less than

2 nm. A possible explanation of this discrepancy in terms of

mechanically generated strains is given in the next section.

Since this method for obtaining an absolute spacing was

not reliable, an alternative means to calculate the area and

spacing was tried. The second approach was to check for cor-

respondence between the area calculated from the ratio of

theoretical current and current density calculations of Chap-

ter II and the area estimated from the Log I_{cv}-S data with

use of Table I or Eq. 2.70. From the results given in Table I

a conduction area of approximately 2.4 X 10^{-13} m^2, with a

slight variation with work function and electrode spacing, is

obtained. If a spacing parameter S of 1.2 nm, a measured cur-

rent of 10^{-9} A, and a work function of 3.0 eV are assumed,

then one may estimate a tunneling conduction area of approx-

imately 5 X 10^{-16} m^2 by extrapolating the values given in

Table I. This area corresponds to a region of 20 nm radius

or about 1/20th that of the radius expected for perfect

spheres. Such an area is possible and could be produced by

by microscopic projections from the spherical surfaces.

However, a second possible hypothesis to explain this

difference between measured and predicted currents is that

the assumed point of contact occurred when S was not zero.

Several processes discussed in Chapter II would produce this effect. First, the transition from equal Fermi energies to equal bulk electrostatic potentials, even though a small effect for the almost identical electrodes of this experiment, could produce a change in slope of the Log I_{cv}-S curve that would be interpreted as contact. Second, adsorbed or chemisorbed molecules would produce a nonzero S at contact.

Third, a change in slope at some value of S will be produced by the onset of constriction resistance[1f] dominated current flow. For this conduction process the electrical resistance, R, between two large conductors connected by a small conduction area of radius, a, is given by: $R = p/(4a)$, where p is the conductors' resistivity. Gold's resistivity is 2.3 X 10^{-8} ohm-m. Thus with the area resulting from the first hypothisis, the expected conduction resistance would be approximately 0.3 ohm. The measured resistance at "contact" was, however, approximately 10^4 ohms. Constriction resistance for the conditions encountered in this experiment, therefore, does not appear to be a current limiting factor.

No consistent interpretation of the data given if Figs. 32, 33, and 36 has been found which gives an absolute electrode spacing and a tunneling conduction area. Future experiments will be required to resolve the unknown relationships between the barrier parameter S and the true physical spacing, and the difficulties of unknown conduction area.

Somewhat as a last resort the I-V characteristics of the tunneling device were explored at large electrode spacings. Fig. 37 shows the breakdown behavior which was typically observed for voltages greater than about 1.0 V, even with relatively large electrode spacings.
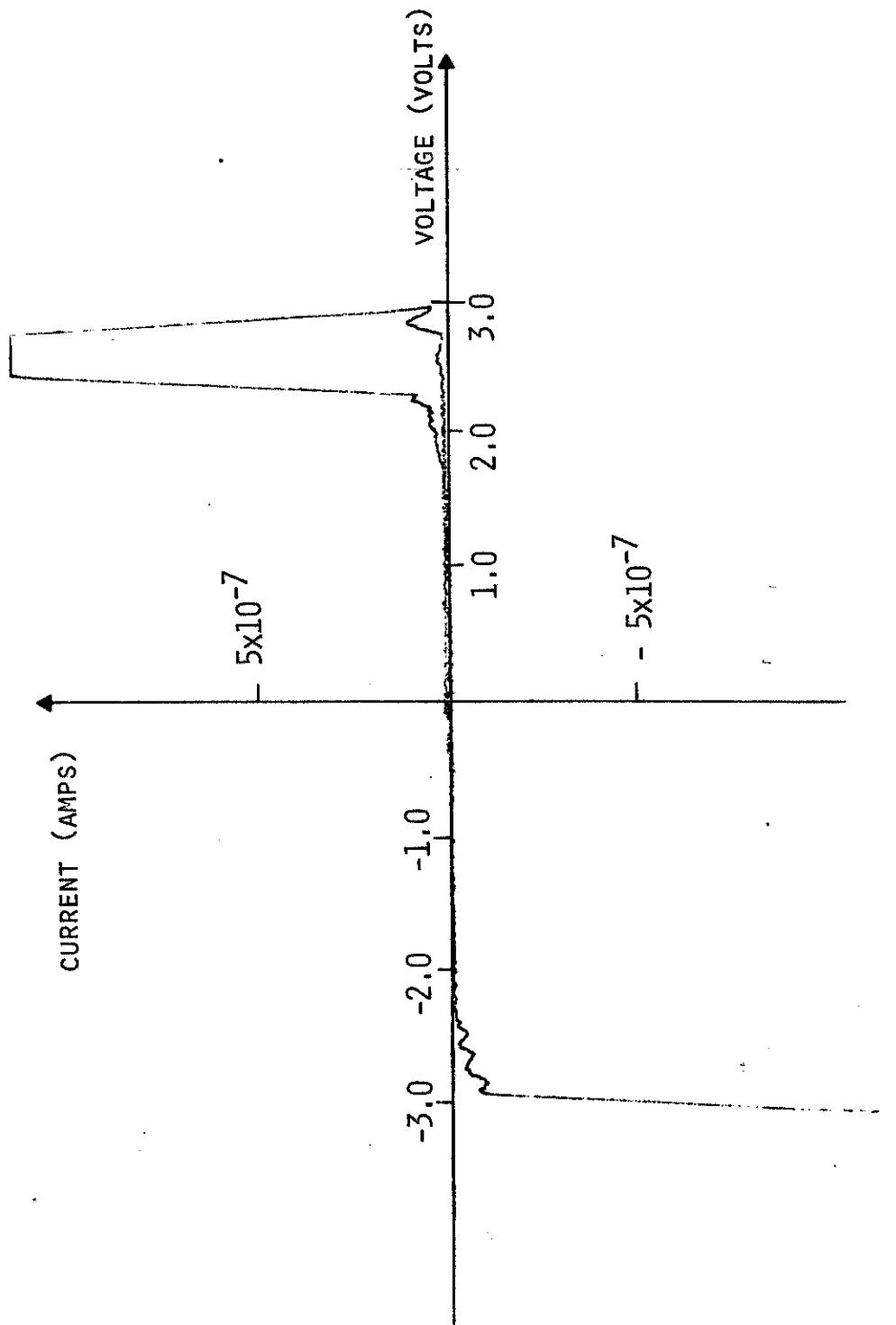
Fig. 37. Current-Voltage Characteristic for Electrode Spacing of Approximately 3.0 nm. The breakdown behavior was typical of all attempts to obtain I-V measurements for bias voltages greater than about 1.0 V.

The Effects of Mechanical Stress on the

Tunneling Characteristics

There are two likely sources of attractive forces
between the tunneling electrodes which could, by producing
surface deflections, affect both the Log I vs S and the
I vs V characteristics. These are the Van der Waals type
forces between two microscopic bodies and the force arising
from the electrostatic field produced by the applied bias
voltage.

The Van der Waals type forces between two microscopic
bodies spaced a distance D apart in a vacuum may be calcu-
lated from a general microscopic theory of dispersion forces
proposed by Lifshitz.[57,58] When D is less than the smallest
characteristic absorption wavelength of the material of the
bodies, the force per unit area, S_{VDW}, between two planar
bodies is given by

$$S_{VDW} = \hbar w / (8\ pi^2\ D^3) \qquad (4.1)$$

$\hbar w$ is known as the Lifshitz-Van der Waals interaction
constant. By using optical data to deduce the dielectric
functions for metals and the Lifshitz theory Krupp, Schnabel
and Walter[59] computed $\hbar w$ for the case when both bodies were
gold; $\hbar w$ was found to be approximately 1.9×10^{-18} joule.

With D expressed in nm, S_{VDW} between gold planes in vacuum is therefore given by

$$S_{VDW}{}^{Au} = 2 \times 10^7/D^3 \quad N\ nm^3/m^2 \qquad (4.2)$$

The stress, T, produced by an electric field, E, perpendicular to a metal surface is[4]

$$T = 1/2\epsilon_0 E^2, \qquad (4.3)$$

$\epsilon_0 = 8.85 \times 10^{-12}$ FD/m^2. For a voltage V and electrode spacing D (in nm), T is therefore given by

$$T = 4.42 \times 10^6\ (V/D)^2 \quad N\ nm^2/(volt^2\ m^2). \qquad (4.4)$$

Lifshitz's theory is based on the existence of a fluctuating electromagnetic field in the region between the two bodies and the resultant component of the Maxwell stress tensor. Thus, both types of these forces may be viewed as being the static and dynamic manifestation of the same force.

A complete treatment of the strains generated in the gold electrodes by these stresses would be an extremely difficult problem. One would need to account for the non-planarity of the two electrodes in terms of its effect on the Van der Waals forces and the effect of the electric field not being parallel to the axis of the electrodes. However, since the radii of the effective area is small compared to the sphere radius, a reasonable approximation

is that all the forces act parallel to the axis of the two
spherical electrodes. Further assume that the equation
derived by Timoshenko and Goodier[61] for the deflection,
$W(r,\theta)$, at a point (r,θ) on a boundary plane of a semi-
infinite solid, produced by a stress, $q(r',\theta')$, over the
area $r'dr'd\theta'$ holds for the surfaces of the spherical
electrodes. Timoshenko and Goodier's relation between W
and q is

$$W(r,\theta) = [(1 - p^2)/(piY)] \, q(r',\theta') \, dr'd\theta', \qquad (4.5)$$

p is Poisson's ratio for the solid and Y is the elastic
modulus. Eq. 4.5 is based on the assumption that the solid's
elastic properties are isotropic.

Let D_o be the minimum spacing between the electrodes
assuming no mechanical stresses were present. Then, for
the small deviations from the axis of the electrodes, the
spacing, D, at a distance r from the axis is given by
$D = D_o + r^2/R$; R is the radius of the electrodes. With
the assumption about the force directions made earlier,
the maximum deflection will occur on the axis. Here
Eq. 4.5 gives

$$W = [2 (1 - p^2)/Y] \int_0^{R_{max}} q(r') \, dr'. \qquad (4.6)$$

Substituting the sum of the stresses described by Eqs. 4.2 and 4.4 for q into Eq. 4.6 gives

$$W = a \int_0^{R_{max}} [b\, D(r')^{-3} + CV^2\, D(r')^{-2}]\, dr', \qquad (4.7)$$

$a = 2\,(1 - p^2)/Y$, $b = 2 \times 10^7$ N nm^3/m^2,

and $C = 4.42 \times 10^6$ N nm^2/(volt^2 m^2).

Let $y = D(r')/D_o$ then $dr = 1/2\,(D_o R)^{1/2}(y - 1)^{-1/2}$ dy and,

$$W(D_o) = a/2\,(R/D_o^3)^{1/2} \int_1^{y_{max}} (b/D_o)\, y^{-3}(y - 1)^{-1/2} \qquad (4.8)$$

$$+ CV^2\, y^{-2}\,(y - 1)^{-1/2})\, dy.$$

Both parts of the integrand are standard forms. The integral evaluates to:

$$W(D_o) = (a/2)\,(R/D_o^3)^{1/2}\, [b\,(y - 1)^{1/2}/(2D_o y^2) + (3b/4D_o + CV^2)$$

$$(y - 1)^{1/2}/y + \tan^{-1}(y - 1)^{1/2}]\,\Big|_1^{y_{max}} \qquad (4.9)$$

Let y_{max} go to infinity, then

$$W(D_o) = (a/2)\,(R/D_o^3)^{1/2}\, pi/2[(3b/4D_o) + CV^2]. \qquad (4.10)$$

Y for gold is 8.3×10^9 N/m^2, $p = 0.33$ and $R = 1.5 \times 10^6$ nm; with these values, Eq. 4.10 reduces to

$$W(D_o) = 2.1 \times 10^{-7}\, D_o^{-3/2}\,(3b/4D_o + CV^2)\ nm. \qquad (4.11)$$

For the voltages used to obtain the Log I_{cv} vs S data, 10 and 100 mv, the dominant term is that from the Van der Waals force. If D_O is 1 nm, W = 3.1 nm; if D_O = 2 nm, W = 0.56 nm. Taking into account the relatively gradual and controlled behavior of most of the Log I_{cv} vs S data, the "avalanche" magnitudes obtained from this calculation are very puzzling. The history of the electrodes offers a possible explanation. During the process to obtain the first sets of data for Log I_{cv} vs S, typified by Fig. 31, an abrupt transition such as one would expect from the predictions of Eq. 4.11 was observed. However, after the accidental and purposeful electrode cleaning by capacitive discharges, the abrupt or almost step function behavior was no longer observed, e.g., Figs. 32. If the capacitive discharges produced local-ized regions of smaller curvature, the magnitude of the deflections, from both type forces, would be greatly reduced, i.e., if R = 10^3 nm, then W would be reduced by a factor of approximately 35 from that calculated from Eq. 4.11.

The density of electromagnetic modes for the spherical surfaces would be slightly different from that of the flat planes used by Lifshitz. Other microscopic geometrical deviations such as plateaus raised above a relatively smooth background would also affect the mode density. However, the geometry in both cases so closely approximates that of two planes over the areas which would contribute, i.e., about

10 𝜇m in radius, that the changes in the mode densities should not affect the result given by Eq. 4.11.

The effects predicted by the voltage dependent part support the previous proposal that the anomalously large curvature in the I vs V data for a fixed spacing was due to mechanical stresses. The difference between the theoretical ly calculated value of I for a particular voltage and spacing, e.g., Figs. 11 and 12, and that measured, e.g., Fig. 36 would correspond approximately to a voltage produced deflection of 0.08 nm for voltages of 0.35 volts. These values were obtained from the s-0.3 nm curve of Fig. 36 as estimates of deviations from a linear I - V characteristic. The change in W between V = 0 and V = 0.35 volts with D_o = 1.5 nm as obtained from Eq. 4.11 is 0.06 nm.

Conclusions

Albeit crudely, an experiment has been performed which demonstrates quantum mechanical tunneling of electrons through a vacuum region of continuously variable thickness. Within experimental error the results indicate that an image potential reduced barrier with the modifications suggested by Lang and Kohn gives a close approximation to the true barrier for metal-vacuum-metal tunneling. For the first time, the work function of the electrodes in a tunneling experiment has been deduced from experimental parameters independent of the tunneling device.

The device which was developed for this experiment demonstrates that vacuum tunneling experiments are feasible and can reliably be performed. With this demonstration many new areas of research may be explored. A particularly direct application of the vacuum tunneling technique is that of locating the true position of a surface to a precision of 0.1 nm, 10 to 100 times greater than presently available techniques. Without the limitation to electrode materials which form oxides that are good barriers, vacuum tunneling experiments will be a very versatile tool for performing inelastic electron tunneling spectroscopy.

Some contributions toward accomplishing the objectives given in Chapter I have therefore been made, but much remains to be done. The problems which have been discovered,

e.g. strains generated by field generated stresses and the
unknown relationship between physical and theoretical
spacing parameters, will need resolution before further work
can be performed. However, the work here does give direction
for solving the problems and once they are solved the full
potential of vacuum tunneling experiments can be realized.

APPENDIX I

NUMERICAL CALCULATIONS OF TUNNELING CURRENT

The computer programs, all in FORTRAN, which were used to calculate the data for the graphs and tables given in Chapter II are contained in this appendix. The programs were executed on the National Bureau of Standards 1108A Computing Facility. The main programs of these computations are CURDEN, to calculate the tunneling current density; CURNT, to calculate the tunneling current between spherical electrodes and a program to calculate the tunneling current density according to Simmons' theory.

Aside from the problems of roundoff and overflow errors, the major difficulty which had to be overcome was long computational times. In an earlier version of these programs, the Newton-Raphson method was used to find the classical turning points for the required energy values and a standard iterative Simpson's 1/3 rule integration was used for all integrations. With these algorithms, the computational time for one current density value ranged from 20 to 30 seconds, with the longer times corresponding to larger electrode spacings. The process of determining the turning points is deeply nested within the chain of integrals to calculate the current and current density. Its computational time is therefore a major component of the overall computational time.

By changing to the indicated tanh rule for integrating over K(x) and using an explicit solution for the roots of a cubic equation, the computational times were cut by a factor of 10 to 15.[62] The iterative method of increasing the number of partitions until the difference between the result for n and 2n partitions was less than a specified error was also dropped. After determining what number was required for the needed accuracy, a fixed number of 64 or 128 was used in all integrations. The particular number is specified in the programs involved.

With the programs as indicated, the time to compute one current density value was two seconds; the time for one current value was 15 seconds. The resulting values, within the limitations of the physical model, should be accurate to five and four significant digits respectively since doubling the number of partitions did not change the least significant digit.

The fundamental data unit of the 1108A central processing unit is a 36-bit word. Average processing rate is about 900,000 instructions per second; 0.75 microseconds for integer addition to 17.25 microseconds for double precision floating-point division. Single precision floating-point numbers carried about 8 significant decimal digits (27 bits) in the range: 2×10^{-39} to $1 \times 10^{+38}$. Double precision floating-point numbers carried about 18 significant decimal digits (60 bits) in the range: 3×10^{-309} to $8 \times 10^{+307}$.

```
C    COMPUTE APPROXIMATE VALUES OF CURRENT DENSITY
C    ACCORDING TO SIMMONS THEORY.  SEE THE FOLLOWING REFERENCE:
C    BURSTEIN, ELIAS AND LUNDQVIST, STIG, "TUNNELING PHENOMENA
C    IN SOLIDS", CH. 10 BY J.G. SIMMONS.
C    EQUATION 11, P. 141 HAS BEEN CORRECTED TO READ AS FOLLOWS:
C
C    S2=S(1-(23/KS)/(3UF+(10/KS)-2U)+S1

      REAL J0,JT
      DIMENSION JT(11)
      U(S,U,UF)=S*(1-23/(3*UF*S+10-2*U*S))
      UBI(S,U,UF,S1,S2)=UF-(U/(2*S))*(S1+S2)
     &  -(2.86/(S2-S1))*ALOG((S2*(S-S1))/(S1*(S-S2)))
      DATA UF,A,C/5.0,-1.025,6.2E14/
      DO 10 I=3,30
      S=I
      JT(1)=S/10
      DO 20 J=2,11
      U=(J-1.)/20.
      S1=3/UF
      S2=U(S,U,UF)+S1
      U1=U(S,U,UF)
      U1=UBI(S,U,UF,S1,S2)
      U2=U1+U
      J0=C*(U1*EXP(A*U1*SQRT(U1)))/(U1**2)
      J0=J0-C*(U2*EXP(A*U1*SQRT(U2)))/(U1**2)
      JT(J)=J0*(1+(3E-9*((U1*300.)**2)/U1))
   20 CONTINUE
      WRITE(7,600) (JT(L),L=1,11)
  600 FORMAT(12X,F4.1,1X,10E9.3)
   10 CONTINUE
      STOP
      END
```

Listing of CURDEN

```
C    PROGRAM TUNNEL CURRENT DENSITY (CURDEN)
C
C    WRITTEN BY E. CLAYTON TEAGUE    MARCH 1978
C
C    SUBPROGRAMS CALLED: RSIM13, PROD
C
C    THIS IS A PROGRAM TO CALCULATE THE TUNNELING CURRENT AS A
C    FUNCTION OF ELECTRODE SPACING AND APPLIED VOLTAGE.  THE INSUL-
C    ATING BARRIER IS ASSUMED TO BE VACUUM AS MODIFIED BY THE IMAGE
C    POTENTIAL.  THE CALCULATIONS ARE BASED ON A FREE ELECTRON MODEL
C    FOR THE ELECTRODES WITH A FREE ELECTRON MASS IN BOTH ELECTRODES
C    AND IN VACUUM. A SYMMETRICAL STRUCTURE WITH IDENTICAL
C    ELECTRODES IS ASSUMED.
C
C    THE BASIC TUNNELING EQUATIONS ASSUMING A WKB SOLUTION
C    TO THE SCHRODINGER EQUATION ARE:
C    (C.B. DUKE, TUNNELING IN SOLIDS, ACADEMIC PRESS, NEW YORK, 1969,
C    PP. 49-53)
C    CURRENT DENSITY(V, D, T,)= INTEGRAL(O TO INF)[DEX* D(EX, V, D, )*
C                               N(EX, V, T)]
C
C    WHERE:
C
C    N(EX, V, T) = (4(PI)MEKT)/H**3 * LN(XPONT)
C
C    WHERE XPONT = 1 + EXP[(FE-EX)/KT]/[1 +EXP[(FE - EX - EV)/KT]]
C
C    4(PI)MEK/H**3 = 1.385E10 AMPS/(EV,K)
C
C    D(EX, V, D) = (1 + EXP[-J(EX, V, D)])**-1
C
C    WHERE J(EX, V, D) = INT [X1(EX, V) TO X2(EX, V)]
C                        OF[4(PI)(2M)**0.5]/H]*[U(X)- EX]**0.5
```

Listing of CURDEN

```
C
C      THE BOTTOM OF THE CONDUCTION BAND OF THE "LEFT"
C      ELECTRODE IS ASSUMED TO BE E = 0 .  A VOLTAGE V IS APPLIED TO
C      LOWER THE ELECTRON ENERGIES OF THE "RIGHT" ELECTRODE.
C      THUS THE TOTAL POTENTIAL ENERGY FUNCTION FOR THE BARRIER IS
C      GIVEN BY:
C
C      U(X) = 0,       X LESS THAN OR EQUAL TO 0
C      U(X) = BARRIER HEIGHT - ELECTRIC POTENTIAL -IMAGE POTENTIAL
C                      0 < X < D
C      U(X) = - EV    X GREATER THAN OR EQUAL TO D.
C
C      THE BARRIER IS THEREFORE GIVEN BY:
C
C      U(X) = FE + WF - (EV/D)X -
C             (E**2) D * LN 2 * 1.15 / ((8 PI * EPPO * X(D -X))** -1)
C
C      IF D IS IN NM AND V, FE, AND WF ARE IN VOLTS,
C
C      THIS REDUCES TO:
C
C      U(X) = FE + WF - (V/D) X - 0.2867 D/ (X[D-X]).
C
C      THUS FOR CALCULATION ONE MUST FIRST DETERMINE FOR EACH VOLTAGE
C      THE CLASSICAL TURNING POINTS X1(EX, V) AND X2(EX, V) FOR EACH
C      RELAVENT ENERGY BETWEEN 0 AND FE + WF.
C
C      THE TUNNELING PROBABILITY IS THEN CALCULATED AS A FUNCTION
C      OF ENERGY, VOLTAGE, AND BARRIER.THICKNESS.   AFTER
C      CALCULATING THE SUPPLY FUNCTION "N" AS A FUNCTION
C      OF ENERGY, VOLTAGE, AND TEMPERATURE, THE CURRENT DENSITY FLOW
C      IS FINALLY CALCULATED AS A FUNCTION OF THE VOLTAGE
C      BARRIER THICKNESS, AND TEMPERATURE.
```

Listing of CURDEN

```fortran
C
C     THE USER IS REQUESTED TO SUPPLY THE TEMPERATURE OF THE
C     TUNNELING DEVICE, AND THE WORK FUNCTION AND FERMI ENERGY
C     OF THE ELECTRODES.
C
      REAL NTGL1,NTGL2,NTGL3
      COMMON T,FE,WF,V,D,FK
      EXTERNAL PROD
      DATA NP /128/
C
      NP2=NP/2
C
C     GET TEMPERATURE
C
      WRITE (6,90)
      READ (5,80) T
C
C     GET FERMI ENERGY
C
      WRITE (6,100)
      READ (5,80) FE
C
C     GET WORK FUNCTION
C
      WRITE (6,110)
      READ (5,80) WF
C
C     GET MINIMUM ELECTRODE SPACING
C
      WRITE (6,120)
      READ (5,80) IMIN
C
C     GET MAXIMUM ELECTRODE SPACING
```

Listing of CURDEN

```
C
      WRITE (6,130)
      READ (5,80) IMAX
      IDIF=IMAX-IMIN
C
C     GET INCREMENTS OF ELECTRODE SPACING
C
      WRITE (6,60)
      READ (5,80) NIES
C
      IF (IDIF.LT.NIES) IINC=1
      IF (IDIF.LT.NIES) GO TO 10
      IINC=IDIF/NIES
C
C     GET MINIMUM VOLTAGE
C
10    WRITE (6,140)
      READ (5,80) JMIN
C
C     GET MAXIMUM VOLTAGE
C
      WRITE (6,150)
      READ (5,80) JMAX
      JDIF=JMAX-JMIN
C
C     GET INCREMENTS OF VOLTAGE
C
      WRITE (6,70)
      READ (5,80) NV
C
      IF (JDIF.LT.NV) JINC=1
      IF (JDIF.LT.NV) GO TO 20
      JINC=JDIF/NV
```

Listing of CURDEN

```
C
20      WRITE (6,170) T,WF,FE
        WRITE (6,180)
C
        DO 50 ID=IMIN,IMAX,IINC
            D=ID/1000.
C
            DO 40 JV=JMIN,JMAX,JINC
                V=JV/1000.
                BLZCTT=8.6E-5*T
                DLTA=40.*BLZCTT+V
C
C       IF (E-FE) IS LESS THAN 40KT THEN: LN(XPONT) = EV/KT
C
                ETOP=FE+WF-1.1468/D
C
C       ETOP = TOP OF IMAGE POTENTIAL WITH NO BIAS VOLTAGE.
C
C       SET MAXIMUM TUNNELING BARRIER HEIGHT AS WF + DLTA
C
C       1ST INTEGRAL COVERS ENERGY RANGE WHERE LN(XPONT) MAY BE
C       APPROXIMATED BY EV/KT
C
                A=ETOP-WF-DLTA
                IF (A.LT.0.) A=0
                B=FE-DLTA
                FK=1.
                NTGL1=RSIM13(PROD,A,B,NP2)
C
C       2ND INTEGRAL COVERS ENERGY RANGE WHERE FULL VARIATION OF
C       LN(XPONT) AND TUNNPB MUST BE TAKEN INTO ACCOUNT. NOTE THAT
C       SINCE TUNNPB INCREASES AS E INCREASES UPPER LIMIT IS EXTENDED
C       TO 80KT
```

Listing of CURDEN

```
C
          A=FE-DLTA
          DIFF=ETOP-(FE+80.*BLZCTT)
          B=ETOP
          IF (DIFF.GT.0.1) B=FE+80.*BLZCTT
          FK=2.
          NTGL2=RSIM13(PROD,A,B,NP)

C
C    3RD INTEGRAL COVERS ENERGY RANGE IN WHICH TUNNPB IS ASSUMED
C    TO VARY LINEARLY WITH ENERGY, AND WHEN ETOP-FE IS LESS THAN
C    80KT.
C
          IF (DIFF.GT.0.1) NTGL3=0.
          IF (DIFF.GT.0.1) GO TO 30
          A=ETOP
          B=FE+80.*BLZCTT
          FK=3.
          NTGL3=RSIM13(PROD,A,B,NP2)

C
30        RJ=NTGL1+NTGL2+NTGL3
          WRITE (6,160) D,V,RJ

C
C    AT THE NATIONAL BUREAU OF STANDARDS COMPUTER FACILITY THE FOLLOWING
C    STATEMENT WRITES INTO AN AUTOMATICALLY CREATED TEMPORARY FILE CALLED
C    7.  UPON TERMINATION OF THE RUN FILE 7 MAY BE COPIED INTO THE USERS
C    OWN FILE FOR PERMANENT STORAGE.
C
          WRITE (7,160) D,V,RJ

C
40        CONTINUE
50        CONTINUE
          STOP
C
```

```
Listing of CURDEN

C
60    FORMAT (1X,'HOW MANY INCREMENTS OF ELECTRODE SPACING?')
70    FORMAT (1X,'HOW MANY INCREMENTS OF VOLTAGE?')
80    FORMAT ()
90    FORMAT (' ENTER TEMPERATURE IN DEGREES KELVIN     (REAL#)')
100   FORMAT (' ENTER FERMI ENERGY IN ELECTRON VOLTS    (REAL#)')
110   FORMAT (' ENTER WORKFUNCTION IN ELECTRON VOLTS    (REAL#)')
120   FORMAT (' ENTER MINIMUM ELECTRODE SPACING IN PM.  (INTEGER #)')
130   FORMAT (' ENTER MAXIMUM ELECTRODE SPACING IN PM.  (INTEGER #)')
140   FORMAT (' ENTER MINIMUM VOLTAGE IN MILLIVOLTS.   (INTEGER #)')
150   FORMAT (' ENTER MAXIMUM VOLTAGE IN MILLIVOLTS    (INTEGER#)')
160   FORMAT (2F8.3,E12.5)
170   FORMAT (1H1,//,8X,' TEMPERATURE = ',1X,F5.1,' DEGREES KELVIN.',/,
     2 8X,' WORK FUNCTION = ',1X,F4.1,' ELECTRON VOLTS.',//,8X,
     3 ' FERMI ENERGY = ',1X,F4.1,' ELECTRON VOLTS.',////)
180   FORMAT (8X,' COLUMN 1 = ELECTRODE SPACING IN NM.',//,3X,
     2 ' COLUMN 2 = BIAS VOLTAGE IN VOLTS.',//,8X,
     3 ' COLUMN 3 = CURRENT DENSITY FLOW IN AMPERES PER SQ.M',////)

C
      END
```

Listing of CURNT

```
C     PROGRAM TUNNEL CURRENT (CURNT)
C
C     WRITTEN BY E. CLAYTON TEAGUE    MARCH 1978
C
C     SUBPROGRAMS CALLED: RSJM13, DNSITY
C
      COMMON T,FE,WF,V
      EXTERNAL DNSITY
      DATA NPART /16/
C
C     GET TEMPERATURE
C
      WRITE (6,80)
      READ (5,70) T
C
C     GET FERMI ENERGY
C
      WRITE (6,90)
      READ (5,70) FE
C
C     GET WORK FUNCTION
C
      WRITE (6,100)
      READ (5,70) WF
C
C     GET MINIMUM ELECTRODE SPACING
C
      WRITE (6,110)
      READ (5,70) IMIN
C
C     GET MAXIMUM ELECTRODE SPACING
C
      WRITE (6,120)
```

Listing of CURNT

```
      READ (5,70) IMAX
      IDIF=IMAX-IMIN
C
C     GET INCREMENTS OF ELECTRODE SPACING
C
      WRITE (6,50)
      READ (5,70) NIES
C
      IF (IDIF.LT.NIES) IINC=1
      IF (IDIF.LT.NIES) GO TO 10
      IINC=IDIF/NIES
C
C     GET MINIMUM VOLTAGE
C
10    WRITE (6,130)
      READ (5,70) JMIN
C
C     GET MAXIMUM VOLTAGE
C
      WRITE (6,140)
      READ (5,70) JMAX
      JDIF=JMAX-JMIN
C
C     GET INCREMENTS OF VOLTAGE
C
      WRITE (6,60)
      READ (5,70) NV
C
      IF (JDIF.LT.NV) JINC=1
      IF (JDIF.LT.NV) GO TO 20
      JINC=JDIF/NV
C
20    WRITE (6,160) T,WF,FE
```

Listing of CURNT

```fortran
      WRITE (6,170)
C
      DO 40 ID=IMIN,IMAX,IINC
      D=ID/1000.
C
      DO 30 JV=JMIN,JMAX,JINC
      V=JV/1000.
C
C     INTEGRATE THE CURRENT DENSITY OVER SPHERICAL
C     SURFACES TO OBTAIN THE NET CURRENT FLOW.
C
      A=D
      B=D+0.4
      CURNT=RSJM13(DNSITY,A,B,NPART)
C
      CURNT=CURNT*3.14159265*1.5E-12
C
      WRITE (6,150) D,V,CURNT
C
C     AT THE NATIONAL BUREAU OF STANDARDS COMPUTER FACILITY THE FOLLOWING
C     STATEMENT WRITES INTO AN AUTOMATICALLY CREATED TEMPORARY FILE CALLED
C     7.  UPON TERMINATION OF THE RUN FILE 7 MAY BE COPIED INTO THE USERS
C     OWN FILE FOR PERMANENT STORAGE.
C
      WRITE (7,150) D,V,CURNT
C
30    CONTINUE
40    CONTINUE
C
      STOP
C
C
50    FORMAT (1X,'HOW MANY INCREMENTS OF ELECTRODE SPACING?')
```

```
Listing of CURNT

60    FORMAT (1X,'HOW MANY INCREMENTS OF VOLTAGE?')
70    FORMAT ()
80    FORMAT (' ENTER TEMPERATURE IN DEGREES KELVIN        (REAL#)')
90    FORMAT (' ENTER FERMI ENERGY IN ELECTRON VOLTS       (REAL#)')
100   FORMAT (' ENTER WORKFUNCTION IN ELECTRON VOLTS       (REAL#)')
110   FORMAT (' ENTER MINIMUM ELECTRODE SPACING IN PM. (INTEGER #)')
120   FORMAT (' ENTER MAXIMUM ELECTRODE SPACING IN PM. (INTEGER#)')
130   FORMAT (' ENTER MINIMUM VOLTAGE IN MILLIVOLTS. (INTEGER#)')
140   FORMAT (' ENTER MAXIMUM VOLTAGE IN MILLIVOLTS  (INTEGER#)')
150   FORMAT (2F8.3,E12.5)
160   FORMAT (1H1,//,8X,' TEMPERATURE = ',1X,F5.1,' DEGREES KELVIN.'/,
     2 8X,' WORK FUNCTION = ',1X,F4.1,' ELECTRON VOLTS.',/,8X,
     3 ' FERMI ENERGY = ',1X,F4.1,' ELECTRON VOLTS.',///)
170   FORMAT (8X,' COLUMN 1 = ELECTRODE SPACING IN NM.',/,8X,
     2 ' COLUMN 2 = BIAS VOLTAGE IN VOLTS.',/,8X,
     3 ' COLUMN 3 = CURRENT FLOW IN AMPERES ',////)

C

      END
```

```
      FUNCTION DNSITY (Z)

C     WRITTEN BY E. CLAYTON TEAGUE    MARCH 1978
C     SEE ANNOTATIONS IN CURRENT DENSITY PROGRAM.
C
C     SUBPROGRAMS CALLED: RSIM13, PROD
C
C     REAL NTGL1,NTGL2,NTGL3
C
      COMMON T,FE,WF,V,Z1,FK
      EXTERNAL PROD
      DATA NP /64/
C
      NP2=NP/2
      Z1=Z
      BLZCTT=8.6E-5*T
      DLTA=40.*BLZCTT+V
      ETOP=FE+WF-1.1468/Z
C
C     SET MAXIMUM ENERGY BARRIER HEIGHT AS WF + DLTA
C
      A=ETOP-WF-DLTA
C
      IF (A.LT.0.) A=0
      B=FE-DLTA
      FK=1.
C
      NTGL1=RSIM13(PROD,A,B,NP2)
C
      A=FE-DLTA
      DIFF=ETOP-(FE+80.*BLZCTT)
      B=ETOP
```

Listing of DNSITY

```
      IF (DIFF.GT.0.1) B=FE+80.*BLZCTT
      FK=2.
C
      NTGL2=RSIM13(PROD,A,B,NP)
C
      IF (DIFF.GT.0.1) NTGL3=0.
      IF (DIFF.GT.0.1) GO TO 10
      A=ETOP
      B=FE+80.*BLZCTT
      FK=3.
C
      NTGL3=RSIM13(PROD,A,B,NP2)
C
   10 DNSITY=NTGL1+NTGL2+NTGL3
C
      RETURN
      END
```

Listing of PROD

```
      FUNCTION PROD (EM)

C     WRITTEN BY E. CLAYTON TEAGUE    APRIL 1978
C
C     SUBPROGRAMS CALLED: RNTOP, TUNNPB
C
C     COMMON T,FE,WF,V,D,FK
C
      K=FK
      GO TO (10,20,30), K
C
C     NOTE THAT T IN CONSTANT OF RNTOP WAS CANCELLED BY T IN EV/KT.
C
10    PROD=(1.385E10)*(V/8.6E-5)*TUNNPB(EM)
      RETURN
C
20    PROD=RNTOP(EM)*TUNNPB(EM)
      RETURN
C
30    PROD=RNTOP(EM)*(1+(D/2.2936)*(EM-FE-WF))
C
      RETURN
      END
```

Listing of RNTOP

```
      FUNCTION RNTOP (EM)

C     WRITTEN BY E. CLAYTON TEAGUE    APRIL 1978
C
C     DOUBLE PRECISION FERMIL,FERMIR,ALPHA,BETA,BLZCTT
      COMMON T,FE,WF,V
C
      BLZCTT=8.6D-5*DBLE(T)
      ALPHA=DEXP(DBLE(FE-EM)/BLZCTT)
      BETA=DEXP(DBLE(FE-EM-V)/BLZCTT)
C
C     AVOID ROUNDOFF ERROR IN DOUBLE PRECISION BY USING APPROXIMATION
C     THAT LN[(1+A)/(1+B)]  = A-B WHEN A AND B ARE MUCH LESS THAN 1.
C
C     IF (ALPHA.LT.1D-6) GO TO 10
C
C     AVOID OVERFLOW ERRORS BY USING APPROXIMATION THAT
C     LN[(1+EXP(A))/(1+EXP(A+B))] = -B WHEN
C     A IS MUCH GREATER THAN 1.
C
      IF (BETA.GT.1D6) GO TO 20
C
      FERMIL=1.0D0+ALPHA
      FERMIR=1.0D0+BETA
      RNTOP=1.385D10*DBLE(T)*(DLOG(FERMIL)-DLOG(FERMIR))
      RETURN
C
10    RNTOP=1.385D10*DBLE(T)*(ALPHA-BETA)
C
      RETURN
C
20    RNTOP=1.385D10*DBLE(T)*DBLE(V)/BLZCTT
C
      RETURN; END
```

Listing of TUNNPB

```
      FUNCTION TUNNPB (EM)

C     WRITTEN BY E. CLAYTON TEAGUE    APRIL 1978

C     SUBPROGRAMS CALLED: DCUBIC, RNIHF, RTPOT

C     DOUBLE PRECISION A3,A2,A1,A0,Z1R,Z1I,Z2R,Z2I,Z3R,Z3I
C     EXTERNAL RTPOT
C     COMMON T,FE,WF,V,D,FK

C     CALCULATE X1(EM,V,D) AND X2(EM,V,D) TURNING POINTS.
C     CUBIC COEFFICIENTS CALCULATED FROM POT (IN SUBPROGRAM RTPOT).

      A3=V/D
      A2=-FE-WF+EM-V
      A1=(FE+WF-EM)*D
      A0=-.2867*D
      CALL DCUBIC (A3,A2,A1,A0,Z1R,Z1I,Z2R,Z2I,Z3R,Z3I)
      X1EM=Z2R
      X2EM=Z3R

C     CALCULATE THE TUNNELING PROBABILITY AS A FUNCTION OF ENERGY

      IF (X1EM.LT.0.0.OR.X2EM.GT.D) GO TO 10

C     CALCULATE TUNNELING INTEGRAL

      Y=RNIHF(RTPOT,X1EM,X2EM,16)

C     USE MILLER AND GOOD'S FORM OF WKB APPROXIMATION

      TUNNPB=1/(1+EXP(Y))
```

Listing of TUNNPB

```
        RETURN
C
10      WRITE (6,20) X1EM,X2EM
        TUNNPB=0.5
        RETURN
C
C
20      FORMAT (1X,'TURNING POINTS',1X,F8.5,1X,'AND',1X,F8.5,1X,
       2 'ARE OUT OF BOUNDS --- TUNPB SET = 0.5')
C
        END
```

Listing of RTPOT

```
        FUNCTION RTPOT (XEM)
C
C       WRITTEN BY E. CLAYTON TEAGUE      APRIL 1978
C
        COMMON T,FE,WF,V,D,FK,EM
C
        POT=FE+WF-EM-(V/D)*XEM-0.2867*D/(XEM*(D-XEM))
        IF (POT.LT.0.) POT=0.
C
        RTPOT=10.25*SQRT(POT)
C
        RETURN
        END
```

Listing of RSIM13

```
      FUNCTION RSIM13(F,A,B,N)
C     -  -  -  -  -  -  -  -  -  -  -  -  -  -  -  -  -  -  -  -
C     RSIM13    WRITTEN BY CHARLES P. REEVE, STATISTICAL ENGINEERING
C               DIVISION, NATIONAL BUREAU OF STANDARDS
C     FOR: NUMERICAL INTEGRATION BY SIMPSON'S 1/3 RULE
C     SUBPROGRAMS CALLED: USER DEFINED FUNCTION F
C     CURRENT VERSION COMPLETED APRIL 28, 1978
C     -  -  -  -  -  -  -  -  -  -  -  -  -  -  -  -  -  -  -  -
      COMMON T,FE,WF,V,D,FK,X
      N2=N/2
      IF(2*N2.NE.N) GO TO 5
      IF(A.GT.B) GO TO 4
      N21=N2-1
      H=(B-A)/N
      H2=2.*H
      X=A
      RSIM13=F(X)
      X=B
      RSIM13=RSIM13+F(X)
      X=A-H
      DO 10 I=1,N2
      X=X+H2
      RSIM13=RSIM13+4.*F(X)
   10 CONTINUE
      X=A
      DO 12 I=1,N21
      X=X+H2
      RSIM13=RSIM13+2.*F(X)
   12 CONTINUE
      RSIM13=H*RSIM13/3.
      RETURN
    4 WRITE(6,601)
  601 FORMAT(1X,'***LOWER LIMIT OF INTEGRATION EXCEEDS UPPER LIMIT***'/
```

Listing of RSIM13

```
        &4X,'VALUE OF INTEGRAL SET = 0.')
        RSIM13=0.
        RETURN
     5 WRITE(6,602)
   602 FORMAT(1X,'***THE NUMBER OF PARTITIONS MUST BE EVEN***'/4X,
        &'VALUE OF INTEGRAL SET = 0.')
        RSIM13=0.
        RETURN
        END
```

RSJM13 WAS A DUPLICATE COPY OF RSIM13

Listing of RNIHF

```
      FUNCTION RNIHF(F,A,B,N)
C     -  -  -  -  -  -  -  -  -  -  -  -  -  -  -  -  -  -  -
C     RNIHF   WRITTEN BY CHARLES P. REEVE, STATISTICAL ENGINEERING
C             DIVISION, NATIONAL BUREAU OF STANDARDS
C     FOR: NUMERICAL INTEGRATION USING THE TANH RULE
C     REFERENCE: HABER, SEYMOUR, THE TANH RULE FOR NUMERICAL
C           INTEGRATION, SIAM J. NUMER. ANAL., VOL. 14, NO. 4,
C           SEPTEMBER 1977
C     SUBPROGRAMS CALLED: USER DEFINED FUNCTION F
C     CURRENT VERSION COMPLETED APRIL 27, 1978
C     -  -  -  -  -  -  -  -  -  -  -  -  -  -  -  -  -  -  -
      IF(A.GT.B) GO TO 4
      H=3.14159265/SQRT(2.*N)-1/(2.*N)
      X=(B+A)/2
      RNIHF=F(X)
      DO 10 I=1,N
      HI=I*H
      Y=((B-A)/2)*TANH(HI)
      D=COSH(HI)**2
      RNIHF=RNIHF+(F(X+Y)+F(X-Y))/D
   10 CONTINUE
      RNIHF=((B-A)/2)*H*RNIHF
      RETURN
    4 RNIHF=0
      WRITE(6,600)
  600 FORMAT(1X,'***LOWER LIMIT OF INTEGRATION EXCEEDS UPPER LIMIT***'/
     &4X,'VALUE OF INTEGRAL SET = 0. IN SUBPROGRAM RNIHF')
      RETURN
      END
```

Listing of DCUBIC

```
      SUBROUTINE DCUBIC(A3,A2,A1,A0,Z1R,Z1I,Z2R,Z2I,Z3R,Z3I)
C     -   -   -   -   -   -   -   -   -   -   -   -   -   -   -   -   -
C     DCUBIC    WRITTEN BY CHARLES P. REEVE, STATISTICAL ENGINEERING
C                    DIVISION, NATIONAL BUREAU OF STANDARDS
C     FOR: COMPUTING THE ROOTS OF THE CUBIC EQUATION
C              A3 * X**3 + A2 * X**2 + A1 * X + A0 = 0
C          WHERE THE COEFFICIENTS A3, A2, A1, A0 ARE
C          DOUBLE PRECISION.
C          THE METHOD OF SOLUTION IS TAKEN FROM PAGE 17 OF
C          "HANDBOOK OF MATHEMATICAL STATISTICS" BY
C          M. ABRAMOWITZ AND I.A. STEGUN, NBS-AMS-55.
C     SUBPROGRAMS CALLED: KJD
C     CURRENT VERSION COMPLETED MAY 3, 1978
C     -   -   -   -   -   -   -   -   -   -   -   -   -   -   -   -   -
      IMPLICIT DOUBLE PRECISION (A-Z)
      IF(DABS(A3).LE.1D-8) GO TO 4
      PI=3141592653589793D-15
      A2=A2/A3
      A1=A1/A3
      A0=A0/A3
      Q=A1/3-(A2/3)**2
      R=(A1*A2-3*A0)/6-(A2/3)**3
      T=Q**3+R*R
      IF(T.LT.0.) GO TO 2
      T=DSQRT(T)
      S1C=DCBRT(R+T)
      S2C=DCBRT(R-T)
      GO TO 3
    2 TCR=0D0
      TCI=DSQRT(-T)
      CR=R+TCR
      CI=TCI
      A=DATAN(CI/CR)+PI*KJD(CI,CR)
```

Listing of DCUBIC

```
      A=A/3
      RR=DSQRT(CR*CR+CI*CI)
      RR=DCBRT(RR)
      S1R=RR*DCOS(A)
      S1I=RR*DSIN(A)
      CR=R-TCR
      CI=-TCI
      A=DATAN(CI/CR)+PI*KJD(CI,CR)
      A=A/3
      RR=DSQRT(CR*CR+CI*CI)
      RR=DCBRT(RR)
      S2R=RR*DCOS(A)
      S2I=RR*DSIN(A)
    3 UCR=-(S1R+S2R)/2-A2/3
      UCI=-(S1I+S2I)/2
      VCR=-(DSQRT(3D0)/2)*(S1I-S2I)
      VCI=(DSQRT(3D0)/2)*(S1R-S2R)
      Z1R=S1R+S2R-A2/3
      Z1I=S1I+S2I
      Z2R=UCR+VCR
      Z2I=UCI+VCI
      Z3R=UCR-VCR
      Z3I=UCI-VCI
      RETURN
    4 WRITE(6,600)
  600 FORMAT(/1X,'NO SOLUTION -- COEFFICIENT OF X**3 IS LESS THAN 1E-8')
      RETURN
      END
```

Listing of KJD

```
      FUNCTION KJD(T,B)
C     |   |   |   |   |   |   |   |   |   |   |   |
C     KJD   WRITTEN BY CHARLES P. REEVE, STATISTICAL ENGINEERING
C           DIVISION, NATIONAL BUREAU OF STANDARDS
C     FOR:  DETERMINING THE QUADRANT FOR THE INVERSE TANGENT FUNCTION.
C           THE PROPER MULTIPLE OF PI IS ADDED TO THE PRINCIPLE VALUE
C           OF THE INVERSE TANGENT.  THE MODE IS DOUBLE PRECISION
C     SUBPROGRAMS CALLED: -NONE-
C     CURRENT VERSION COMPLETED JUNE 8, 1976
C     |   |   |   |   |   |   |   |   |   |   |   |
      DOUBLE PRECISION T,B
      IF(T.LT.0) GO TO 1
      IF(B.LT.0) GO TO 2
      KJD=0
      RETURN
    1 IF(B.GE.0) GO TO 3
    2 KJD=1
      RETURN
    3 KJD=2
      RETURN
      END
```

APPENDIX II

STATISTICAL FLUCTUATIONS IN THE LENGTH OF A BAR

The fluctuations to be calculated here are those
arising from the thermodynamic properties of matter and do
not account for any additional quantum fluctuations in the
length of the bar. At the temperatures used for this experi-
ment, the quantum fluctuations would be negligible. The
calculations are based on the development given by Landau
and Lifshitz.[63] Starting from the argument that the proba-
bility for a quantity x to have a value in the range x to
x + dx is proportional to $e^{S(x)/k}$, where S(x) is the entropy
of the system involved and k is Boltzmann's constant, they
derive the result:

$$\overline{(\Delta V)^2} = -kT \ (\partial V/\partial P)_T. \tag{II-1}$$

Here $\overline{(\Delta V)^2}$ is the mean square fluctuation of the system
volume at the temperature T.

This may be related to the properties of a solid by
the bulk modulus, B, which is defined by the relation:

$$B = -V \ (\partial P/\partial V)_T, \tag{II-2}$$

Where V is the volume of the solid. Combining Eqs. II-1 and II-2 gives the result:

$$\overline{(\Delta V)}^2 = kTV/B. \tag{II-3}$$

If one now assumes that a bar of length, l, and cross-sectional area, A, is constrained such that all fluctuations are manifest in length changes then the result:

$$\overline{(\Delta l)}^2 = (kT/B)(l/A), \tag{II-4}$$

is obtained, where $\overline{(\Delta l)}^2$ is the mean square fluctuation in the length of the bar.

Values for the parameters of Eq. II-4 which represent the gold electrode leads are:

$$T = 300 \text{ K}$$

$$B = 1.0 \times 10^{10} \text{ dynes/cm}^2$$

$$l = 1 \text{ cm}$$

$$A = 10^{-2} \text{ cm}^2$$

Thus, $\sqrt{\overline{(\Delta l)}^2} = 2 \times 10^{-15}$ m. Calculated values for the fluctuations of other parts of the electrode assembly, i.e., the aluminum housing and the copper holders, are also close to this value for the gold electrodes. Since the fluctuations in all the parts of the electrode assembly would be uncorrelated, the net result would be the square root of the sum of the squares of the individual components. The resultant mean square fluctuations in the electrode

spacing would then be approximately: 4×10^{-15} m. Note that these estimates include all frequency components.

APPENDIX III

VACUUM CONDITIONS TO ACHIEVE AND MAINTAIN

CLEAN SOLID SURFACE

Let T be defined as the time in which an initially clean surface becomes covered with a monolayer of adsorbate when the surface is exposed to a gas at a pressure P Torr, then the purpose of this appendix is to show that an approximate expression for T is

$$T = 2 \times 10^{-6}/P \text{ seconds.} \qquad (III-1)$$

The following derivation assumes that the surface contains 10^{19} adsorption sites/m^2 and that the sticking sufficients for adsorption is one, i.e., every adsorbate molecule which strikes the surface is adsorbed.

According to the kinetic theory of gases, the number of molecules striking unit area per unit time, Z, is given by

$$Z = N_A \, p(2\text{pi} \, M \, R_g \, T)^{-1/2}, \qquad (III-2)$$

where N_A is Avagadro's number, M is the gases molecular weight, R_g is the Universal gas constant, and T is the gas temperature. For Nitrogen, N_2, at $300^{\circ}K$,

$$Z = 2.873 \times 10^{22} \text{ P molecules}/(m^2 s). \qquad (III-3)$$

Converting from units of P from N/m^2 to Torr gives

$$Z = 3.83 \times 10^{24} \text{ P molecules}/(m^2 s). \qquad \text{(III-4)}$$

Time for one monolayer is density of adsorption sites/Z, so

$$T = (10^{19}/m^2)/Z = (2.6 \times 10^{-6})/P \text{ seconds.} \qquad \text{(III-5)}$$

The general form of Eq. A III-1 for N adsorption sites/ unit area is

$$T = CVN(2pi\ M\ R_g\ T)^{1/2}/(N_A\ P), \qquad \text{(III-5)}$$

where C is a proportionality constant determined by the adsorbate's sticking coefficient.

APPENDIX IV

AN ELECTRONIC DEVICE UTILIZING QUANTUM
MECHANICAL TUNNELING

The idea for this electronic device resulted from attempts to design a metal-vacuum-metal tunneling structure with the use of microfabrication techniques commonly employed by the microelectronics industry. Conceptually, the device would combine the properties of piezoelectric ceramics with the high sensitivity of tunneling to changes in electrode spacing to produce an electronic device with a very high transconductance.

Starting with a highly polished piezoelectric substrate which is polarized as a transverse expander, i.e., fields applied normal to substrate plane result in dimensional changes in the substrate plane, the device would be fabricated as shown in Fig. 38. After applying electrodes to both faces of the piezoelectric substrate, a thick layer of poly-crystalline metal or semiconductor, shown as the dotted layer, would be deposited over the anticipated device area. The next step would be to heavily oxidize the metal or semi-conductor layer or by other means form an integral insulating layer, shown as the lightly cross-hatched strips. Following this operation, the tunneling electrodes would be formed on
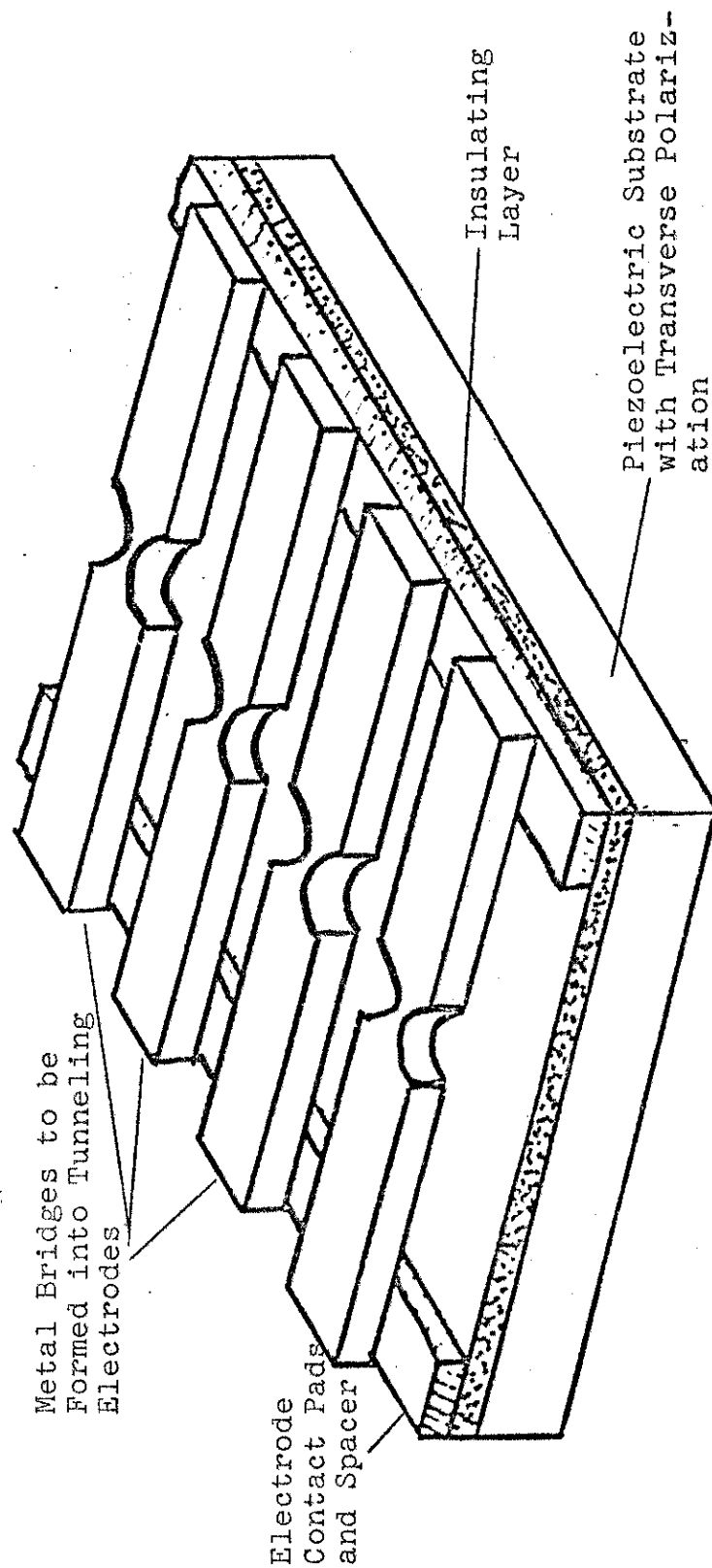
181

Fig. 38. Schematic of Method to Fabricate Tunneling Devices With the Use of Photolithographic Techniques.

top of the insulating layer using standard evaporation and photomasking technology. The final step in the fabrication process would be to remove the insulating layer using a preferential plasma or chemical etching process to leave a structure similar to that shown in Fig. 38. A gap within the range of the piezoelectric substrate would be formed by either highly precise photolithography or by melting a narrow bridge into two parts.

Assuming that one has produced a gap between the two electrodes which is shorter than the transverse dimensional capabilities of the piezoelectric material, the device characteristics should have the following qualitative properties. Let the piezoelectric electrodes be A and B and the tunneling electrodes be C and D. Then, if x_1 is the lateral distance between the bases of the tunneling electrodes and d_{31}, is the lateral expansion coefficient of the piezoelectric ceramic,

$$dx_1 = (d_{31}x_1t^{-1})dV_{AB}, \qquad (IV-1)$$

where t is the ceramic substrate's thickness, and dV_{AB} is the changes in voltage across the substrate. For a fabricated gap of 500 nm, the voltage V_{AB}^o to place the electrodes within tunneling distances for available piezoelectric ceramics would be approximately 50 volts for a 0.1 nm thickness.

Considering the device input to be the voltage applied to the piezoelectric ceramic and the output as the tunneling current I_{CD} for a fixed bias voltage, the transconductance is defined as

$$g = (dI_{CD}/dV_{AB})_{V_{CD} = const.} \qquad (IV-2)$$

Combining Eq. AIV-1 and AIV-2 with the rule-of-thumb tunneling equation

$$I_{CD} = C_1 \exp(C_2 S B^{1/2}) A\ V_{CD}, \qquad (IV-3)$$

where $C_1 = 3.16 \times 10^{13}$ A/m^2/V, $C_2 = 10.25$ (eV)$^{-1/2}$ nm^{-1}, S is the electrode spacing, B the mean barrier height and A is the tunneling area, gives:

$$g = C_1 C_2 B^{1/2}\ e^{C_2 S B^{1/2}}\ d_{31} x_1 t^{-1} A\ V_{CD}. \qquad (IV-4)$$

For tunneling areas of 10^{-12} m^2, $d_{31} = 0.25$ nm/V, $x_1 = 4$ mm, t = 0.1 mm, B = 1 eV, S = 1 nm, and $V_{CD} = 0.1$ Volt,

$$g = 10^{-2}\ A/V (= mho). \qquad (IV-5)$$

This value is about the maximum transconductance obtainable with conventional electronic devices[64],[65]. Increases in tunneling area to 10^{-10} m^2 would raise g to 1 mho.

A photograph of a device resulting from the explanation of this technique for fabricating tunneling structures is shown in Fig. 39. The approach was not pursued any
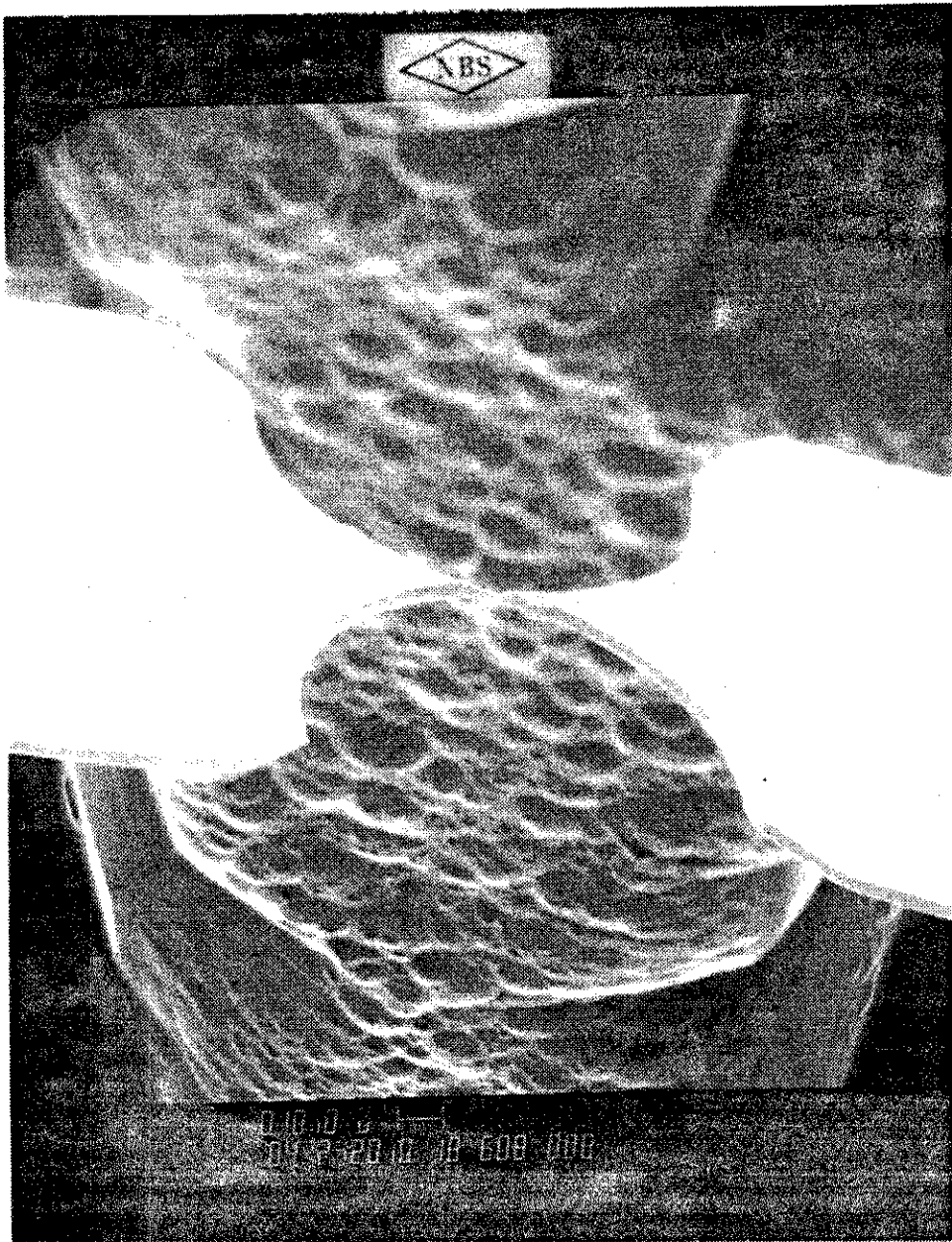
Fig. 39. Scanning-Electron-Microscope Photomicrograph of Prototype Tunneling Device Fabricated With the use of Photolithographic Techniques.

further, because at the time of the investigation, only limited time was available and the preferential etching process to produce the required electrode length of 2 mm was not sufficiently developed. Shorter lengths place demands on photomasking technology that could not be achieved, i.e., forming lines less than one micrometer in width. However, since the time of these attempted fabrication, April 1976, the capabilities of both technologies have significantly advanced.

APPENDIX V

ELECTRONICS FOR THE TEMPERATURE CONTROL SYSTEM

The purpose of this appendix is to give a description
of the two-stage temperature control system and its associated
electronics in terms of the transfer functions of each part
of the system, to derive from these transfer functions the
response of each stage's control system to setpoint changes
and environmental temperature changes, and finally to describe
the procedure employed to choose the lead and lag times of
the compensation network and to "tune" the network for an
acceptable response to setpoint changes. Descriptions of
both stage-controllers are given in terms of the block
diagram shown in Fig. 23. The intent here is not to give
a detailed analysis of the electronic circuity, but rather
to give a reasonably complete description of the basic
properties of the control system in terms of the properties
of its subunits. The transfer function of each subunit will
now be obtained.

The transfer function of the thermistor with respect to
ambient changes in temperature, T, can be obtained from the
equation for conservation of energy:

$$\dot{Q}_E = C\ dT_Z/dt + K(T_Z - T), \qquad (V-1)$$

T_Z = thermistor temperature, Q_E = electrical power input,

C = thermal capacity of the thermistor, and K = dissipation

constant. From this equation, the effects of input power

level may also be obtained. At a steady state temperature,

T_Z^{SS}, T_Z^{SS} - T_{REF} = $\dot{Q}_E$/K. With the input power levels and

dissipation constants described below. T_Z^{SS} - T_{outer} =

0.1 mK and T_Z^{SS} - T_{inner} = 1 ʍK. The Laplace transform

of Eq. V-1 gives the result:

$$T_Z(S) = [1/(1 + ZS)] \ T(S) + Z/[C(1 + ZS)] \ \dot{Q}_E(S), \quad (V-2)$$

Z = K/C is the time constant of the thermistor, and S is

the Laplace transform variable in the transform domain. The

thermistor transfer function with respect to ambient changes

in temperature is therefore:

$$M(S) = T_Z(S)/T(S) = 1/(1 + ZS). \quad (V-3)$$

The time constant, Z, and dissipation constnat, K, for both

controllers are strongly dependent on the manner in which

the thermistor is mounted. The estimates given below for

K were based on the manufacturer's recommendations and the

thermal conductivities of the mounting materials. Z must

account for the thermistor's response time and the coupling

of the thermistor to the heater and system mass. For the

thermistor's response, independent of this last factor, Z was

approximately one to ten seconds. Accounting for the imperfect

coupling of the thermistor and heater, rough estimates for Z

based on observations of system behavior are:

$$Z_{outer} \doteq 10\text{-}20 \text{ s},$$

and

$$Z_{inner} \doteq 100\text{-}150 \text{ s}.$$

The coupling of the thermistor and heating coils on the inner stage was across 6 mm of the inner aluminum enclosure.

Let Z_a, Z_b, Z_c, and Z_d represent the four impedances in a Wheatstone bridge. Then, if $Z = Z_a = Z_b = Z_d$ and $Z_c = Z + dZ$, with dZ much less than Z, the error signal, e, output by the bridge is[66]:

$$e = (E/4)(dZ/Z), \qquad (V\text{-}4)$$

E is the bridge excitation voltage. Thermistors have the property that $Z = Z(T_Z)$, where T_Z is the device temperature. Over a quite large working range $Z(T_Z)$ for the thermistors used in the controller bridges was given by $Z(T_Z) - Z(T_{REF}) = a(T_Z - T_{REF})$ with $a = -0.04 \ Z(T_{REF})/$ K. This along with the thermal transfer function of Eq. V-3 gives:

$$e = A(S)(T_{REF} - T_Z), \qquad (V\text{-}5)$$

where $A(S) = k/(1 + ZS)$, $k = 0.01E$ V/ K.

To minimize the temperature difference between the thermistor and its surroundings, the self-heating of the thermistors by the bridge excitation voltage must be kept to a minimum[67]. The manufacturers recommendation was that the self-heating be less than or equal to 0.1 of the desired control resolution.

The dissipation constants of the two thermistors as mounted

on the two thermal enclosures were 90 mW/$^\circ$C and 42 mW/$^\circ$C

for the outer and inner enclosures respectively. At bridge

balance, one-half of the exciting voltage will be across the

thermistor. Thus, the powers which may be dissipated in the

thermistors assuming one mK stability in the outer stage

and ten μK stability in the inner the stage are 9.0 μW and

and 42 nW, respectively. The recommended excitation volta-

ges are, in turn, 0.85 V and 0.13 V for the outer and inner

stages, respectively. Since any variations in these voltages

would result in an additional variation of the control signal,

stable sources are required. As a compromise between the

recommended excitation voltge and the need for stability,

a 1.35 volt mercury cell was used for the outer stage-bridge.

The inner stage-bridge was driven by a stabilized oscillator

with an output of 100 mV rms.

The circuit diagrams for both stages are shown in

Figs. 40 and 41. The lock-in amplifier employed for the

sensor amplifier was an instrument designed and built

in-house at the National Bureau of Standards[68]. It had gain

settings from 500 up to 10^6, time constants available from

0.5 s to 20 s and operated at a fixed frequency of one

kilohertz. To a first approximation, the transfer functions

of both sensor amplifiers may, for small deviations from

bridge balance, be represented by the equation:

$$H_1(S) = V_1(S)/e(S) = A/(1 + qS), \qquad (V-6)$$
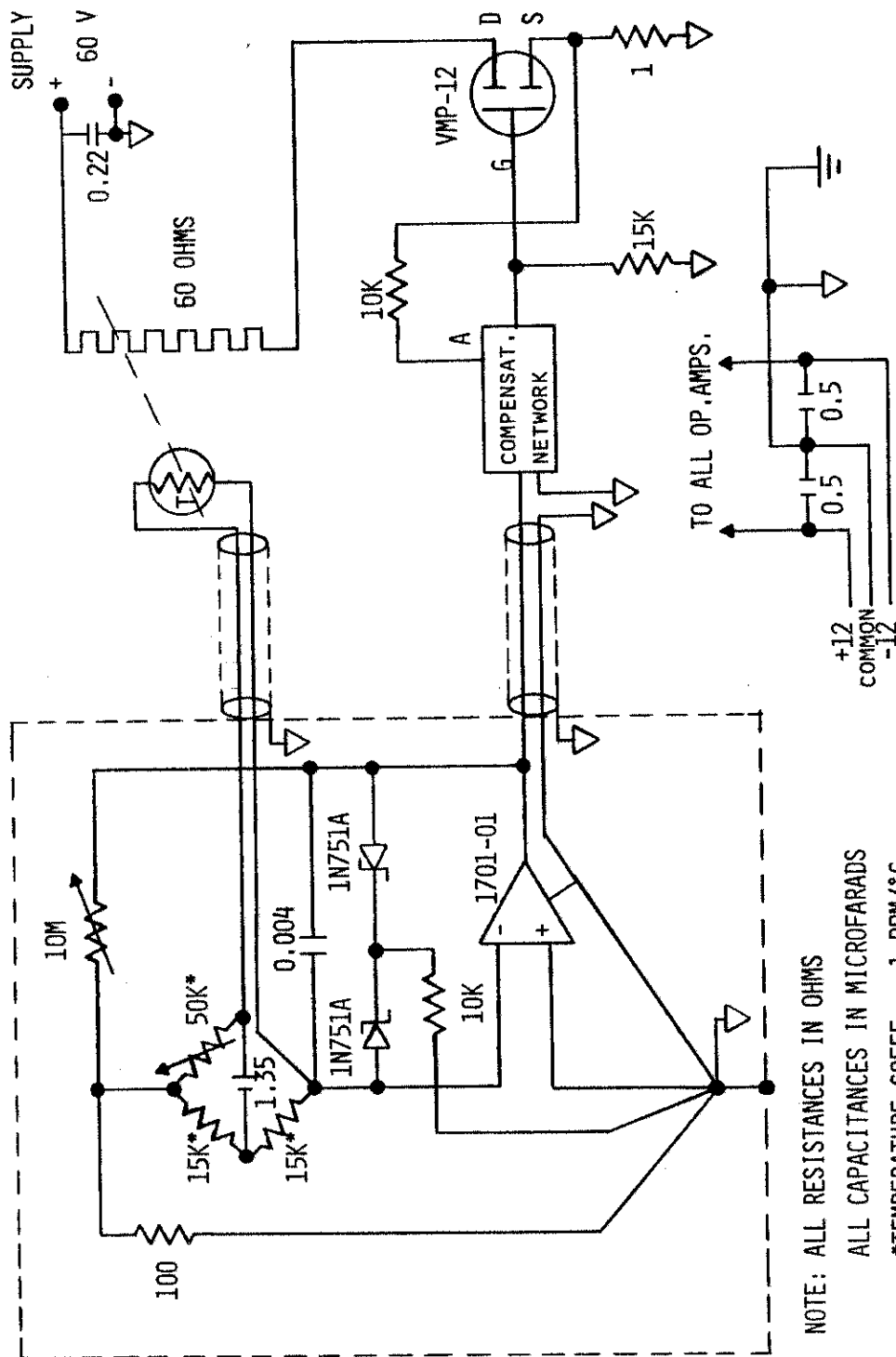
NOTE: ALL RESISTANCES IN OHMS
ALL CAPACITANCES IN MICROFARADS
*TEMPERATURE COEFF. = 1 PPM/°C
5 PPM/YR

Fig. 40. Schematic of Electronics for Outer Temperature Control Stage.

Fig. 41. Schematic of Electronics for Inner Temperature Control Stage.

A is the amplifier's dc gain or for the lock-in amplifier

its gain when the rms value of the input is not changing,

and q is the time constant of the respective amplifier.

This transfer function for the lock-in amplifier represents

the relationship between the dc output voltage and the rms

value of the input ac signal with the selected phase. For

the lock-in amplifier, q is simply the time constant setting

of the amplifier's low pass filter. Eq. V-6 assumes the

lock-in filter is equivalent to one RC stage. For the sensor

amplifier of the outer-stage-controller, q was set by the

0.004 μfd capacitor at 4×10^{-2} s since this was the approx-

imate value expected from the 12 dB/octave gain characteris-

tic and anticipated gain setting.

For both stages, the bridge-sensor amplifier combination

was configured to obtain the required negative feedback.

With the outer stage controller, this only amounted to

choosing the correct polarity of the bridge excitation

voltage. With the lock-in amplifier, this was accomplished

by choosing the appropriate phase to detect.

A brief note about the particular bridge circuit used

for the outer sensor amplifier. This circuit allows the

use of a single ended chopper stabilized amplifier and its

attendant low drift. Another advantage of the circuit is that

the gain is not dependent on the absolute value of the bridge

resistors and can be simply adjusted by changing the ratio

of the 10 Mohm and 100 ohm resistors.

The transfer function of the compensation network shown in Fig. 42 is given by [69]:

$$H_2(S) = V2/V1 = P + DS/(1 + aS)(1 + bS) + I/S, \quad (V-7)$$

where P is the proportional gain setting, I is the product of the integration channel's gain and the inverse of the integration time and D is the product of the differentiation time constant and this channel's gain. The time constant, a, was 0.2 s for the outer-stage controller and 2.0 s for the inner-stage controller; b was 0.5 D for the outer-stage and 0.05 D for the inner-stage. The open loop transfer function of the operational amplifiers used in the compensation network is to first order:

$$M(S) = 2 \times 10^{-5}/(1 + 6 \times 10^{-3} S). \quad (V-8)$$

Since this pole and the pole at S = 100 in the proportional channel are so much higher frequency poles than all the other poles of the controllers, their effects, which are minor, will not be included in the following discussion.

The response properties of the power amplifier for both control stages can be understood by noting that a fundamental property of an operational amplifier is to maintain the summing point, i.e., the inverting input, at a "virtual ground" condition.[69] The implication of this property for the power amplifier portion of the controllers is that all current flow to the inverting input of the operational
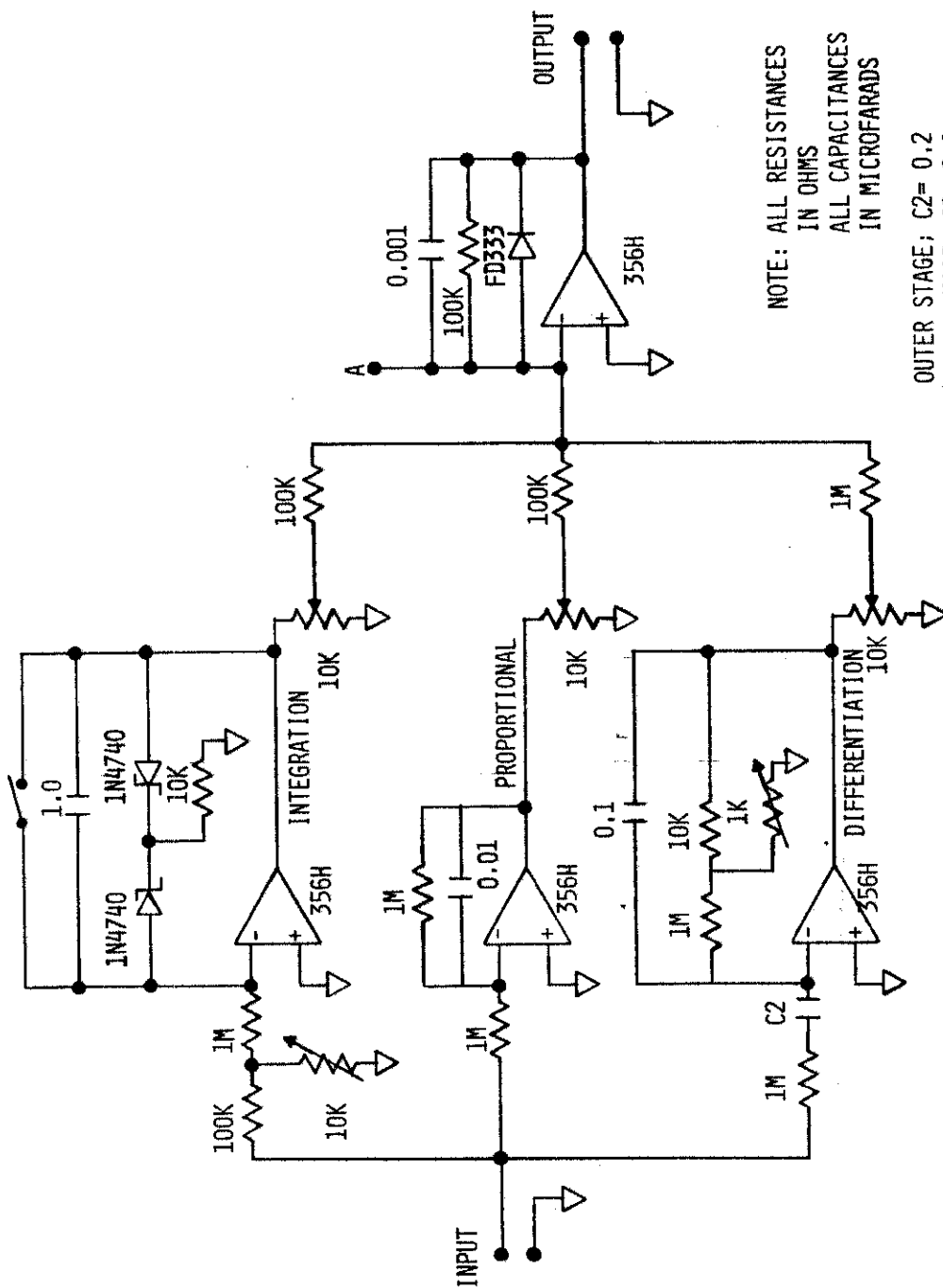
Fig. 42. Schematic of Compensation Network Used for Both Temperature Control Stages.

amplifier which drives the MOSFET power transistor, a VMP-12 or 22, must also flow thru the 10 Kohm feedback resistor, R_{FB}, connected to the device's source terminal. (This, of course, neglects the small amount flowing through the 100 Kohm resistor to the operational amplifier output.) This condition can be used to relate the voltage applied to the heater, V3, and the equivalent voltage output from the compensation network, V2. V2 is the voltage produced by the sum of the currents from the three channels of the compensation network with an equivalent input resistance, R_i, of 100 Kohms. Thus, with these definitions; $V2 = I \, R_i$, where "I" is the summed current. The voltage at the source terminal will then be maintained at; $V_{FB} = I \, R_{FB}$. But, $V_{FB} = (V3/R_H)R_B$, from a simple application of ohm's law. So:

$$V3 = (R_{FB}/R_i)(R_H/R_B) \, V2. \qquad (V-9)$$

Here R_H is the heater resistance and R_B is the bias resistance between common and the device source terminal.

The transfer function of the power amplifier is determined by the dc gain obtained from Eq. (V-9) and the response of the operational amplifier in the feedback loop. The corner frequency of the MOS device is greater than 100 MHz. Thus, the overall transfer function of the power amplifier would be:

$$H_3(S) = V3/V2 = A_p/(1 + pS), \qquad (V-10)$$

with $A_p = (R_{FB}/R_i)(R_H/R_B)$ and $p = 6 \times 10^{-3}$ s. As indicated for the compensation network, the effects of this high frequency pole are not accounted for in the following discussion.

To obtain a model of the thermal response of the heaters and their respective masses, a simple lumped parameter model of the heat conduction and radiation was utilized. Referring back to Fig. 22, let R represent the thermal resistance of all conduction paths between each stage's components and its environment. For the outer stage, these paths include the polyurethane foam, the stainless steel ports to the vacuum pumps, the electrical connecting leads, and the epoxy supports used to thermally isolate the outer stage from the granite vibration isolation table. For the inner stage, these paths include the electrical connecting leads and the ceramic supports. By analogy with electrical circuit terminology, R is given by: $R = (R_S - T_E)/\dot{Q}_C$, where T_S = temperature of stage, T_E = temperature of the stage's environment and $\dot{Q}_C$ = power loss due to conduction.

Radiation transfer of energy is a major factor which must be considered in the design of the inner control stage. Zemansky[70] shows that the rate of energy transfer $\dot{Q}_R$, between a body with emissivity, e, and temperature, T, and a surrounding system at temperature, T_E, is given by:

$$\dot{Q}_R = Aes \, (T^4 - T_E^4). \qquad\qquad (V-11)$$

Here A is the surface area of the enclosed body and s is

the Stefan-Boltzmann constant.

With the use of this lumped parameter model, the thermal

behavior of each stage can be described by the equation for

the conservation of energy:

$$\dot{Q} = \dot{Q}_{IN} - \dot{Q}_C - \dot{Q}_R \qquad (V-12)$$

or:

$$C \; dT/dt = V^2/r - (T - T_e)/R - Aes \; (T^4 - T_E^4), \qquad (V-13)$$

where C is the heat capacity of each stage, V is the voltage

applied to heater coils of resistance r, and the other

symbols are as defined previously. If Eq. V-13 is linearized

by expanding T and V about their operating point values,

T_{REF} and V_0, at which dT/dt = 0, the following equation

holds for small deviations about these values:

$$dT/dt + 1/R'C \; T = 2V_0/rC \; V + 1/R'C \; T_E, \qquad (V-14)$$

Where $1/R' = 1/R + 4AesT_{REF}^3$. Let $t_T = R'C$ and $t_E = rC$,

then the Laplace transform of Eq. V-14 gives the result:

$$T(S) = G_1(S)V(S) + G_2(S)T_E(S) \qquad (V-15)$$

where $G_1(S) = 2V_0 t_T/(t_e \; (1 + t_T S))$ or $G_2(S) = 1/(1 + t_e S)$.

The transfer function of the cascaded sensor amplifier

compensation network, and power amplifier is given by the

product of their individual transfer functions[71]. Therefore,

let:

$$H(s) = V3/e = H_1(S) \times H_2(S) \times H_3(S). \qquad (V-16)$$

The controllers feedback responses are then determined by the equations:

$$e = A(S)(T_{REF} - T)$$
$$V = V_3 = H(S) \; e \qquad (V-17)$$
$$T = G_1(S)V + G_2(S)T_E,$$

The transform variable is not indicated on the dependent variables. Solving this set of equations for T gives:

$$T = [G_2(S) \; T_E + A(S)G_1(S)H(S) \; T_{REF}] \; F(S), \qquad (V-18)$$

$$F(S) = [1 + A(S)G_1(S)H(S)]^{-1}.$$

The following discussion is presented in terms of changes in T_{REF}. While the transient response of the system is different for changes in T_{REF} and T_E, the stability conditions are the same for both system changes. Calculations were only made in terms of changes in T_{REF} since step changes in T_{REF} were anticipated.

Let $K(S) = T(S)/T_{REF}(S)$, then:

$$K(S) = G_1(S)H(S)A(S)F(S). \qquad (V-19)$$

$K(S)$ is the overall transfer function describing the response of the closed loop system to changes in the setpoint, T_{REF}. Substitution of the various parameter and function definitions yields the result:

$$G_1(S)H(S)A(S) = \frac{g(S+S_1)(S + S_2)(S + S_3)}{S(1+t_1S)(1+aS)(1+bS)(1+ZS)(1 +qA)}, \quad (V-20)$$

Where $g = 2kAA_pV_ot_T/t_e$.

The zeros S_1, S_2, and S_3 are the roots of the equation:

$$S^3 + [I/p + 1/b + 1/a + D/(abP)] S^2 \qquad (V-21)$$

$$+ [I/bP + I/aP + 1/ab] S + I/abP = 0.$$

This equation reduces to the following equations for the two stages;

outer stage:

$$S^3 + 15 S^2 + [5I + 10/D]_1 S + 10 I/D = 0, \qquad (V-22)$$

and inner stage:

$$S^3 + 11 S^2 + [20I + 10/D]_2 S + 10 I/D = 0. \qquad (V-23)$$

For Eqs. V-22 and V-23, the roots are approximately[72]:

outer stage:

$$S_1 \doteq -15, \quad S_2, \; S_3 \doteq -(2S_1)^{-1} [\;]_1 \pm S_1^{-1} [\;]_1^{1/2},$$

and inner stage:

$$S_1 \doteq -11, \quad S_2, \; S_3 \doteq -(2S_1)^{-1} [\;]_2 \pm S_2^{-1} [\;]_2^{1/2}.$$

Parameters of the outer-stage controller were:

heat capacity $= C = 1.42 \times 10^4$ joule/$^\circ$C

heater resistance $= r = 60$ ohm

thermal resistance $= R = 0.8$ $^\circ$C/W

steady state voltage $= V_o = 20$ V

bridge constant $= k = 0.1$ V/$^\circ$C

stage time constant $= RC = t_T = 1.1 \times 10^4$ s

power amplifier gain = A_p = 6 V/V

The poles, other than the high frequency ones not accounted for in Eq. V-20, were a = 0.25 s, b = 0.5 D s, Z = 10-20 s, and q = 4×10^{-2} s.

Parameters of the inner-stage controller were:

heat capacity = C = 2.9×10^3 joule/$^\circ$C

heater resistance = r = 1.05×10^3 ohm

thermal resistance = R = 8 $^\circ$C/W

steady state voltage = V_o = 10 V

bridge constant = k = 1×10^{-3} V/$^\circ$C

stage time constant = RC = 2.3×10^4 s

power amplifier gain = A_p = 3

The poles were located at a = 2.0 s, b = 0.05D s, Z $\doteq$ 100 - 150 s, and q $\doteq$ 0.5 - 2 s. The thermal resistance R of this stage represents the parallel resistance of conduction and radiation.

The poles and zeros of K(S) in the S-plane completely determine the stability of the temperature-control stages and their transient responses to changes in setpoint temperature and environmental temperature.[71] Some guidelines for the design of a feedback system which are usually scattered throughout most texts on control systems, are:

A. The system will be unstable if K(S) contains any poles in the right half-plane.

B. The system's transient response is increasingly

oscillatory as the poles of K(S) move toward the imaginary axis.

C. The system's speed of response is proportional to the distance of the dominant poles from the S-plane origin.

D. Introduction of negative real zeros in K(S) in general increases system stability.

E. The relative weighting, R_L, of the Lth mode of a system, i.e., a pole or a complex pair of poles, is determined by:

$$R_L = \frac{\displaystyle\prod_{i=1}^{m} P_i - n_i}{P_L \displaystyle\prod_{\substack{i=1 \\ j \neq L}}^{n} P_L - P_j} \qquad\qquad (V-24)$$

where n_i, i= 1, m, are the zeros of K(S) and P_j, j = 1, n, are the poles of K(S). Thus, placing zeros near troublesome or oscillatory poles minimizes their effect.

F. The response of a feedback system as in Fig. 23 to a constant reference input has a zero steady-state error if and only if the open loop transfer function $G_1(S)H(S)A(S)$ has at least one pole at S = 0. For zero steady-state error with reference inputs of the form, a t^n, the requirement is that $G_1(S)H(S)A(S)$ have a pole at S = 0 with multiplicity m greater than n.

G. For disturbance inputs, a similar property holds.
    Here the pole at S = 0 must be in the controller
    transfer function H(S). Therefore, a controller
    with a pole at S = 0 insures that a zero steady-
    state error may be achieved in both cases.

An attempt was made to use these guidelines in adjusting
the lead and lag times of the compensation networks. The
procedure for adjustment was to set I and D to zero and P = 1.
The overall gain of the feedback loop was then increased by
increasing A, the sensor amplifier gain, until the stage-
controller broke into oscillation. D and I were then increased
to the values calculated below; D to eliminate the instability
by introducing zeros near the origin and I to eliminate or
minimize any offset by introducing a pole at the origin. The
effects of these changes can be visualized in terms of a root-
locus diagram. This type diagram is a graph of the paths
traced by the poles of K(S) as g is varied from zero to
infinity. A root-locus diagram, constructed with the aid of
the root-locus properties described by Fortmann and Hitz[73]
and Kuo[74], for K(S) of the outer-stage controller is sketched
in Fig. 43. Only the dominant poles and zeroes are drawn
since the effects of the other ones are principally to change
the angles of the asymptotes of the root-loci.

An examination of the diagram in Fig. 43 will show that
before compensation, the two dominant poles are the ones due
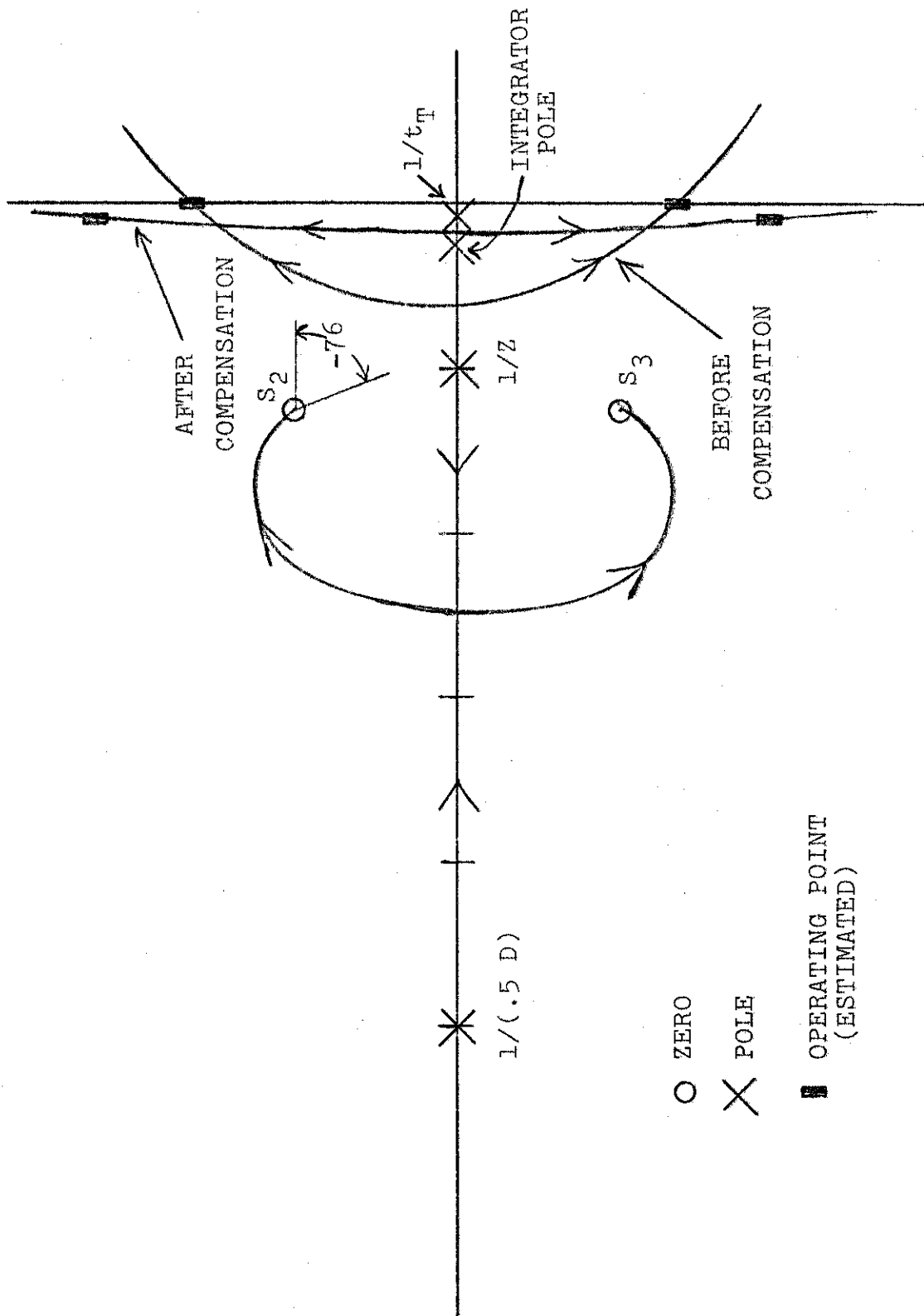to the thermal lag of the stage mass and to the time constant

Fig. 43. Sketch of Root-Locus Diagram For Temperature Control System.

of transferring energy from the heater to the thermistor.
These are labelled $1/t_T$ and $1/Z$ respectively in the diagram.
The compensation network introduces three zeros and three new
poles. The zeros tend to straighten the root-locus branch
that causes instability so that the same gain may be used
with no oscillations. An equal margin of stability without
compensation would have required significantly reduced
loop gain and, thus, less attenuation of environmental distur-
bances.

D and I were initially chosen to bring the zeros, S_2 and
S_3, to be adjacent to the pole at $1/Z$ to approximately cancel
its effect. From the roots given for Eqs. V-22 and V-23, this
condition requires that for the outer stage:

$$1/30 \; [5I + 10/D] = 0.1$$

and for the inner stage:

$$1/22 \; [20I + 10/D] = 0.01.$$

Initial setting for D and I were;

for outer stage:

$$I = 0.1 \; S^{-1}, \; D = 3 \; s$$

and for inner stage:

$$I = 0.01 \; S^{-1}, \; D = 50 \; s.$$

After some "tweaking" of I, D, and P to get maximum gain
without oscillations, the responses to setpoint changes shown
in Figs. 44 and 45 were obtained. These responses are certainly
not optimum, but are acceptable. The sensor amplifier gains
and compensation network settings to obtain these responses

were; outer stage: $A = 5000$ V/V, $I = 0.013$ S^{-1}, $D = 4$ S, $P = 1$, and inner stage: $A = 5 \times 10^5$ V/V, $I = 0.015$ S^{-1}, $D = 200$ S, $P = 0.75$.

With these sensor amplifier gains, the closed loop gain, including the bridge and thermistor response, were;

outer stage: $A_{CL} = A \, A_p \, k = 3,000$ V/$^\circ$C

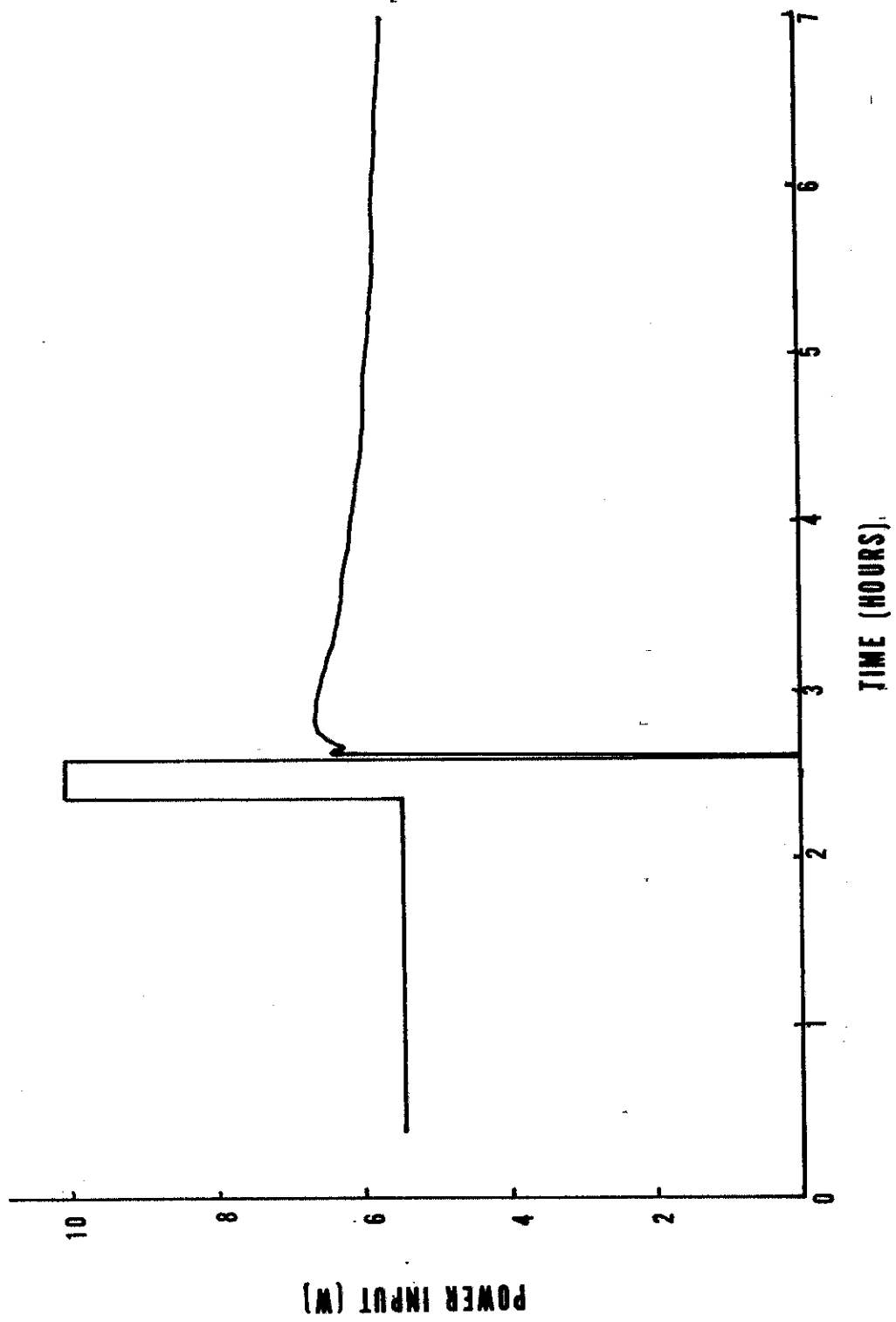inner stage: $A_{CL} = A \, A_p \, k = 15,000$ V/$^\circ$C

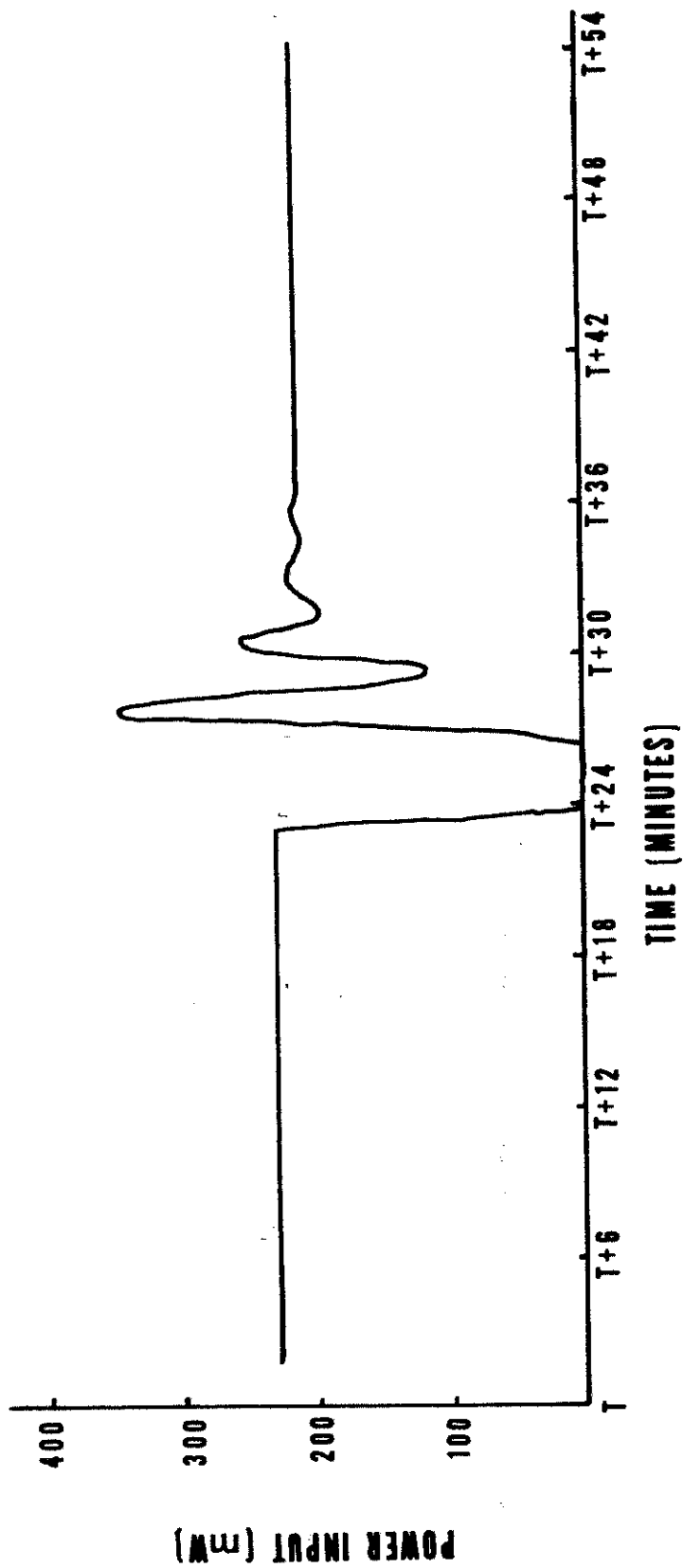Fig. 44.   Response of Outer Temperature Control Stage to Setpoint Change.

Fig. 45. Response of Inner Temperature Control Stage to Setpoint Change.

REFERENCES

1a. E. Schrödinger, "Quantization as a Problem of Proper Values, Part I," Annalen der Physik 79, 361 (1926); Part II, Ibid. 79, 489 (1926); Part III, Ibid. 80, 437 (1926), and Part IV, Ibid. 81, 109 (1926).

1b. J. R. Oppenheimer, "Three Notes on the Quantum Theory of Aperiodic Effects," Phys. Rev. 31, 66 (1928).

1c. R. H. Fowler and L. Nordheim, "Electron Emission in Intense Electric Fields," Proc. Roy. Soc. (London), 119, 173 (1928).

1d. G. Gamow, "Zur Quanten Theorie des Atomkernes," Z. Phys., 51, 204 (1928).

1e. J. Frenkel, "On the Electrical Resistance of Contacts Between Solid Conductors," Phys. Rev. 36, 1604 (1930).

1f. R. Holm, Electric Contacts, (Springer-Verlag, New York, 1967).

1g. I. Giaever, "Energy Gap in Superconductors Measured by Electron Tunneling," Phys. Rev. Lett. 5, 147, 464 (1960), and "Electron Tunneling and Superconductivity," Science 183, 1253 (1974), Nobel Prize Lecture.

1h. L. Esaki, "Long Journey into Tunneling," Science 183, 1149 (1974), Nobel Prize Lecture and Phys. Rev. 109, 603 (1958).

1i. B. D. Josephson, "Possible New Effects in Superconductive Tunneling," Phys. Lett. 1, 251 (1962), and "The Discovery of Tunneling Supercurrents," Science 184, 527 (1974), Nobel Prize Lecture.

1j. J. Lambe and R. C. Jaklevic, "Molecular Vibration Spectra by Inelastic Electron Tunneling," Phys. Rev. 165, 821 (1968).

2a. R. D. Young, J. Ward, and F. Scire, "Observation of Metal-Vacuum-Metal Tunneling, Field Emission, and The Transition Region," Phys. Rev. Lett. 27, 922 (1971).

2b. W. A. Thompson and S. F. Hanrahan, "Thermal Drive Apparatus for Direct Vacuum Tunneling Experiments", Rev. Sci. Instrum. 47, 1303 (1976).

3. E. Burstein and S. Lundquist, Tunneling Phenomena in Solids, (Plenum Press, New York, 1969).

4. C. B. Duke, Tunneling In Solids, (Academic Press, New York, 1969).

5. J. G. Simmons, "Generalized Formula for the Electric Tunnel Effect Between Similar Electrodes Separated By a Thin Insulating Film," J. Appl. Phys. 34, 1793 (1963).

6. W. A. Harrison, "Tunneling From an Independent-Particle Point of View," Phys. Rev. 123, 85 (1961).

7. R. Stratton, "Volt-Current Characteristics for Tunneling Through Insulating Films," J. Phys. Chem. Solids 23, 1177 (1962).

8. W. F. Brinkman, R. C. Dynes, and J. M. Rowell, "Tunneling Conductance of Asymmetrical Barriers," J. Appl. Phys. 41, 1915 (1970).

9. J. A. Appelbaum and W. F. Brinkman, "Theory of Many-Body Effects in Tunneling," Phys. Rev. 186, 464 (1969).

10. C. Caroli, R. Cambescot, D. Wederer-Rozenblatt, P. Nozieres, and D. Saint-James, "Comment on a Recent Theory of Tunneling Without the Transfer-Hamiltonian Formalism," Phys. Rev. B 12, 3977 (1975), and references contained therein.

11. T. E. Feuchtwang, "Theory of Tunneling without Transfer Hamiltonian," Phys. Rev. B 12, 3979 (1975), and references contained therein.

12. S. L. Kurtin, T. C. McGill, C. A. Mead, "Direct Interelectrode Tunneling in GaSe," Phys. Rev. B 3, 3368 (1971).

13. C. B. Duke; Reference 4, pp 60-65

14. N. D. Lang and W. Kohn, "Theory of Metal Surfaces: Charge Density and Surface Energy," Phys. Rev. B 1, 4555 (1970).

15. N. D. Lang and W. Kohn, "Theory of Metal Surfaces: Work Function," Phys. Rev. B 3, 1215 (1971).

16. N. D. Lang and W. Kohn, "Theory of Metal Surfaces: Induced Surface Charge and Image Potential," Phys. Rev. B 7, 3541 (1973).

17. W. Kohn and L. J. Sham, "Self-Consistent Equations Including Exchange and Correlation Effects," Phys. Rev. 140, A1133 (1965) and P. Hohenberg and W. Kohn, Phys. Rev. 136, B864 (1964).

18. L. Hedin and B. Lundquist, "Explicit Local Exchange-Correlation Potentials," J. Phys. C 4, 2064 (1971).

19. J. C. Slater, The Self-Consistent Field For Molecules and Solids, (McGraw-Hill Book Company, New York, 1974), Chapter 2.

20. V. L. Moruzzi, J. F. Janak, A. R. Williams, Calculated Electronic Properties of Metals, (Pergamon Press Inc., New York, 1978) p. 9.

21. D. E. Eastman, "Photoelectric Work Functions of Transition, Rare-Earth, and Noble Metals", Phys. Rev. B 2, 1 (1970), and G. A. Haas and R. E. Thomas, "Thermionic Emission and Work Function," in Measurement of Physical Properties, Ed. By E. Passaglia, Vol.VI of Techniques of Metal Research, Ed. by R. F. Bunshah, (Interscience Publishers, New York, 1972).

22. J. Bardeen, "Theory of the Work Function," Phys. Rev. 49, 653 (1936).

23. J. A. Applebaum, "Electronic Structure of Solid Surfaces," in Surface Physics of Materials, Edited by J. M. Blakely, (Academic Press, New York, 1975).

24. C. Kittel, Elementary Statistical Physics, (John Wiley, New York, 1858), pp. 25-31.

25. E. Spenke, Electronic Semiconductors, (McGraw-Hill Book Company, 1958), Chapter 10.

26. A. J. Bennett and C. B. Duke, "Self-Consistent Model of Bimetallic Interfaces," Phys. Rev. 160, 541 (1967).

27. J. G. Simmons, "Image Force in Metal-Oxide-Metal Tunnel Junctions," in Reference 3.

28. C. B. Duke, Reference 4, p. 6 and p. 207.

29. L. D. Landau and E. M. Lifshitz, Quantum Mechanics: Non-Relativistic Theory, 3rd Ed, (Pergamon Press, Oxford, England, 1977), pp. 55-60.

30. J. M. Blatt and V. F. Weisskopf, Theoretical Nuclear Physics, (John Wiley and Sons, New York, 1952), pp. 528-529.

31. E. Merzbacher, Quantum Mechanics, 2nd Ed, (John Wiley and Sons, New York, 1970), pp. 116-126.

32. D. Bohm, Quantum Theory, (Prentice-Hall, Inc., New York, 1951), pp. 271-277).

33. C. B. Duke, Reference 4, p. 59.

34. B. A. Politzer, "Comparison of a Numerical Method and the WKB Approximation in the Determination of Transmission Coefficients for Thin Insulating Films," J. Appl. Phys., 37, 279 (1966).

35. J. G. Simmons, "Generalized Formula for the Electric Tunnel Effect Between Similar Electrodes Separated by a Thin Insulating Film," J. Appl. Phys. 34, 1793 (1963), and J. Appl. Phys. 35, 2655 (1964), The forms of the image potential given here must be corrected according to the paper by Simmons in Reference 3.

36. J. G. Simmons, J. Appl. Phys. 34, 238 (1963).

37. H. P. Knauss and R. A. Breslow, "Current-Voltage Characteristic of Tunnel Junctions," Proc. IRE 50, 1834 (1962).

38. J. M. Rowell, "Tunneling Anomalies-Experiment," in Reference 3.

39. E. L. Murphy and R. H. Good, Jr., "Thermionic Emission, Field Emission, and The Transition Region," Phys. Rev. 102, 1464 (1956).

40. R. D. Young, "Theoretical Total-Energy Distribution of Field-Emitted Electrons," Phys. Rev. 113, 110 (1959).

41. S. C. Miller, Jr. and R. M. Good, Jr., "A WKB-Type Approximation to The Schrodinger Equation," Phys. Rev. 91, 174, (1953).

42. J. L. Hunter, Acoustics, (Prentice-Hall, Inc., Englewood Cliffs, NJ, 1962), Chapter 8.

43. T. N. Rhodin and D. L. Adams, "Adsorption of Gases on
    Solids," Chapter 5 in, <u>Treatise on Solid State
    Chemistry: Surfaces</u>, Edited by N. B. Hannay
    (Plenum Press, New York, 1976).

44. M. A. Chesters and G. A. Somorjai, "The Chemisorption
    of Oxygen, Water, and Selected Hydrocarbons on the
    (111) and Stepped Gold Surfaces," Surf. Sci. <u>52</u>,
    21 (1975).

45. B. M. W. Trapnell, "The Activities of Evaporated Metal
    Films in Gas Chemisorption," Proc. Roy. Soc. <u>A218</u>,
    566 (1953).

46. J. L. Gland and G. A. Somorjai, "Low-Energy-Electron-
    Diffraction and Work Function Studies of Adsorbed
    Organic Monolayers on the (100) and (111) Crystal
    Face of Platinum," Advances in Colloid and Interface
    Science <u>5</u>, 205 (1976).

47. R. Hocken, Physicist at National Bureau of Standards,
    private communication.

48. R. Cutkosky and B. F. Field, "Standard Cell Enclosure
    with 20 μK Stability," IEEE Trans. Instrum. Meas.,
    <u>IM-23</u>, 295 (1974).

49. Emerson and Cuming, Inc.; Canton, MA 02021; Stycast
    2850KT with catalyst 24LV for cylindrical walls,
    catalyst 9 for top and bottom surfaces.

50. The particular ceramic used was PZT-8, manufactured by
    the Vernitron Corporation; Piezoelectric Division;
    232 Forbes Road; Bedford, OH 44146. A general
    description of this class of ceramics is given in,
    Piezoelectric Ceramics, by B. Jaffe, W. R. Cook and
    H. Jaffe, (Academic Press, New York, 1971)

51. Emerson and Cuming, Inc.; Canton, MA 02021; Eccobond
    Solder V-91.

52. The insulating film used was "Kapton" manufactured by
    E. I. duPont de Nemours & Company, Inc.; Plastics
    Products and Resins Department; Industrial Films
    Division; Wilmington, DE 19898. Kapton is a
    mechanically strong, transparent, amber colored
    film which has a very low outgassing rate and a
    dielectric strength of 2.75×10^5 V/mm. The
    manufacturer specifies that no outgassing was
    revealed by weight loss at 200°C and 3×10^{-6}
    Torr pressures. This behavior was confirmed
    before use in this experiment by observing that
    a piece .25 m x .25 m x 25 micrometer thick could
    quickly be pumped down to a pressure of 10^{-9} Torr
    with a 50 1/s ion pump system.

53. Model 341A D.C. Voltage Calibrator manufactured by John
    Fluke Mfg. Co., Inc., P.O. Box 43210 Mountlake Terr.,
    WA 98043.

54. F. E. Scire and E. C. Teague, "A Piezo-Driven 50 Micro-
     meter Range Stage with Sub-Nanometer Resolution,"
     Accepted for publication in Rev. Sci. Instrum. Fall
     1978.

55. P. M. Morse and K. V. Ingard, Theoretical Acoustics,
     (McGraw Hill Book Co., New York, (1968), Chapter 5.

56. S. H. Crandall, "The Role of Damping in Vibration Theory,"
     J. of Sound Vibr. 11, 3 (1970).

57. Lifshitz, E. M., "The Theory of Molecular Attractive
     Forces Between Solids," Soviet Physics, Journal of
     Experimental and Theoretical Physics 2, 73 (1956).

58. J. N. Israelachvili and D. Tabor, "Van Der Waals Forces:
     Theory and Experiment," in Progress in Surface and
     Membrane Science Volume 7, Edited by J. F. Danielli,
     M. D. Rosenberg, and D. A. Cadenhead, (Academic
     Press, New York, 1973).

59. H. Krupp, W. Schnabel, and G. Walter, Journal of Colloid
     and Interface Science 39, 421 (1972).

60. W. K. H. Panofsky and M. Phillips, Classical Electricity
     and Magnetism, (Addison-Wesly Publishing Company,
     Reading, MA, 1962), pp. 103-107.

61. S. Timoshenko and J. N. Goodier, Theory of Elasticity,
     (McGraw-Hill Book Company, New York, 1951), pp.
     362-372.

62. The author is indebted to C. P. Reeve, National Bureau of
    Standards, for suggesting and assisting with these
    changes.

63. L. D. Landau and E. M. Lifshitz, Statistical Physics
    (Addison-Wesley Publishing Company, Reading, MA, 1969)
    pp. 348-352.

64. A. S. Grove, Physics and Technology of Semiconductor
    Devices, (John Wiley and Sons, Inc., New York,
    1967), p. 253.

65. R. Boylestad and L. Nashelsky, Electronic Devices and
    Circuit Theory, 2nd Ed., (Prentice Hall, Inc.,
    Englewood, Cliffs, NJ, 1978).

66. Terman and Pettit, Electronic Measurements (McGraw-
    Hill Book Company, Inc. New, York, 1952), pp. 74-83.

67. "Thermistor Manual," (Bulletin EMC-6, Fenwal Electronics,
    1974).

68. The amplifier was designed by Mark Horowitz, National
    Bureau of Standards.

69. J. V. Wait, L. P. Huelsman and G. A. Korn, Introduction
    to Operational Amplifier Theory and Applications,
    (McGraw-Hill Book Company, Inc. 1975), pp 1-55.

70. M. W. Zemansky, Heat and Thermodynamics, (McGraw-Hill Book
    Company, Inc., New York, 1957), p. 106.

71. T. E. Fortmann and K. L. Hitz, An Introduction to Linear
    Control Systems, (Marcel Dekker, Inc., New York, 1977),
    pp. 159-396.

72. J. V. Uspensky, <u>Theory of Equations</u>, (McGraw-Hill Book
    Company, Inc., 1948), pp. 82-94.

73. Reference 71 pp. 300-307.

74. B C. Kuo, <u>Automatic Control Systems</u>, (Prentice-Hall, Inc.,
    1962), pp. 1-170 and 246-300.